ABSTRACT

Title of Document:	THERMOELECTRIC TRANSPORT PHENOMENA IN SEMICONDUCTING NANOSTRUCTURES
	Jane Elizabeth Cornett, Doctor of Philosophy, 2013
Directed By:	Associate Professor Oded Rabin, Department of Materials Science and Engineering

The efficiencies of state-of-the-art thermoelectric devices made from bulk materials remain too low for widespread application. Early predictions by Hicks and Dresselhaus indicated that one potential route for improving the thermoelectric properties of materials was through nanostructuring. This predicted improvement was due to two effects: an increase in the thermoelectric power factor and a decrease in the lattice thermal conductivity.

In this thesis, new models are developed for calculation of the thermoelectric transport properties of nanostructures. The results of these models are in line with what has been seen experimentally in the field of nanostructured thermoelectrics: the power factor of nanostructures falls below the bulk value for sizes accessible by current experimental techniques. While this is demonstrated first for a particular system (cylindrical InSb nanowires), this result is shown to hold true regardless of the dimensionality of the system, the material of interest or the temperature. Using the

analytical forms of the transport properties of nanostructured systems, we derive universal scaling relations for the power factor which further point to the fundamental and general nature of this result.

Calculations done for nanostructured systems in which the scattering time is a function of carrier energy indicate that the introduction of nanoscale grain boundaries can lead to improvements in the power factor. We present experimental methods for the fabrication and characterization of porous bismuth-antimony-telluride ($Bi_{2-x}Sb_xTe_3$) thin films using a templated deposition technique. Preliminary results from this experimental work indicate that the nanostructured morphology of the templates used for the deposition of porous films limits diffusion during grain growth, and thus the crystal structure of these porous films differs from that of films deposited on dense substrates. For fundamental investigation of the effects of porosity on thermoelectric transport, future studies should therefore focus on $Bi_{2-x}Sb_xTe_3$ thin films made by top-down patterning techniques.

THERMOELECTRIC TRANSPORT PHENOMENA IN SEMICONDUCTING
NANOSTRUCTURES

By

Jane Cornett

Dissertation submitted to the Faculty of the Graduate School of the
University of Maryland, College Park, in partial fulfillment
of the requirements for the degree of
Doctor of Philosophy
2013

Advisory Committee:
Professor Oded Rabin, Chair
Professor John Cumings
Professor Ichiro Takeuchi
Professor Bao Yang
Dr. Patrick Taylor

Dedication

To my parents, for their love, guidance and Sunday night dinners.

Acknowledgements

First and foremost I would like to thank my advisor Prof. Oded Rabin for his endless patience and guidance. It is in large part due to his support that I have transformed from a youthful graduate student into a scientist. I would be proud to claim even $1/10^{th}$ of his work ethic. His drive allowed me to realize that I could work harder and accomplish more than I ever thought possible, and for that I am eternally grateful.

I would like to thank all of the Rabin group members and collaborators both past and present from whom I have learned so much. I would like to give a special thank you to Dr. SeungYong Lee, who sat at the desk next to me for 4 years. He was not just a colleague, but a great mentor and an amazing friend. His kind words got me through many a tough day in the lab (and still do). I will always remember the Friday afternoon Korean lessons as a high point in my graduate school career. I would also like to specifically thank Andrew Lawson, a current graduate student in the Rabin group, for his help with so many things from fabricating anodic alumina to editing this thesis. I am so grateful to Dr. Xin Zhang for his hard work, kind explanations and extreme patience in patterning with self-assembled block copolymers over the last 6 months.

I wish to thank the staff in IREAP and in the Fablab not just for their endless help, but also for their friendship. There is nothing quite like pictures of grandchildren or a litter of newborn kittens to brighten any rough day. I would also like to thank Dr. Wen-An Chiou (director the NISP Lab) and Dr. Peter Zavalij (head

of the UMD X-ray Crystallographic Center) for their training and help with SEM and XRD.

On a more personal note, I could not have made it through the last 5 years without my friends and family. Thank you to everyone who has kept me caffeinated, spent uncountable lunch hours laughing with me and supported me in many times of need. Last but certainly not least, I thank my parents. I owe all of this to them--my success is their success.

Table of Contents

List of Tables

List of Figures

Chapter 1 Introduction to Thermoelectricity

1.1 Thermoelectricity

As the global demand for energy continues to grow, alternative and renewable sources become increasingly important. Thermoelectric materials, which can efficiently convert heat into electricity and vice versa, present an exciting solution to this problem: What if we could turn some of the energy rejected as heat (almost 60% of ~10^{20} Joules per year [22]) into useable electrical energy?

Thermoelectric devices are currently used to generate power in several limited applications (for example, power generation for satellites too far from the sun to use solar energy).[23] Future applications include waste heat recovery in cars and industrial plants, which could mean a more substantial dent in demand for non-renewable energy. However, low device efficiencies have thus far made widespread application impractical. Much of the research currently being done in the field of thermoelectrics therefore focuses on improving device efficiency by optimizing the thermoelectric properties of materials. As fabrication and characterization techniques at the nano-scale have improved over the last 30 years, one approach to improving thermoelectric materials is through nanostructuring. This chapter presents a short history and introduction to the field of thermoelectrics, starting with a brief introduction to the thermoelectric effects and the definition of the thermoelectric figure of merit (the quantity used to evaluate the thermoelectric properties of a
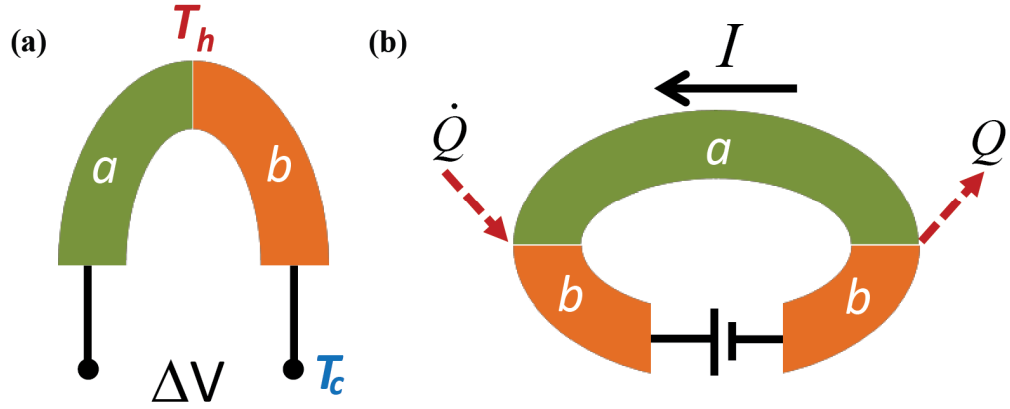
Figure 1.1: Schematics demonstrating the (a) Seebeck effect and (b) the Peltier effect.

material), and finishing with an overview of the relatively new field of nanostructured thermoelectrics.

1.2 *Thermoelectric Effects*

The Seebeck effect, the phenomenon through which materials convert a thermal gradient into useable electrical energy, was discovered in 1821 by Thomas Seebeck. When the top junction of a circuit formed by two dissimilar conductors is heated to some temperature T_h, and the bottom of the circuit is kept at a temperature T_c (see schematic in Figure 1.1(a)) carriers in the legs of the junction diffuse from the hot side to the cold side, forming an open-circuit voltage ΔV. When $\Delta T = T_h - T_c$ is small, this voltage is linear with the temperature difference:

$$\Delta V = -S_{ab}\Delta T. \tag{1.1}$$

2

Here we have defined the Seebeck coefficient of the junction, S_{ab}. The measured voltage ΔV is the difference between the Seebeck voltages created in leg a, $\Delta V_a = -S_a \Delta T$, and leg b, $\Delta V_b = -S_b \Delta T$. It is clear that a large voltage is achieved when the Seebeck coefficients of the two legs are of opposite signs; this occurs when one leg is an n-type thermoelectric material ($S < 0$) and one leg is a p-type thermoelectric material ($S > 0$). The Seebeck effect is harnessed for thermoelectric power generation and for temperature measurement.

If a current I is flowed through the loop formed by two dissimilar materials (Figure 1.1(b)), one junction of the circuit will become hot (emitting heat at a rate $\dot{Q}$) while the other junction will become cold (absorbing heat at the same rate). By reversing the direction of the electrical current, the hot and cold junctions will switch. This is the essence of the Peltier effect, discovered by Jean Peltier in 1834. The rate of heat emission (and absorption) at the junctions is proportional to the applied electrical current via the Peltier coefficient of the junction

$$\dot{Q} = \Pi_{ab} I. \tag{1.2}$$

The emitted (and absorbed) heat at the junctions is the result of the difference between the thermal currents flowing in (and the Peltier coefficients of) the two materials. The Peltier effect is harnessed in thermoelectric cooling and heating devices.[24]

1.3 Thermoelectric Figure of Merit

A schematic of a simple thermoelectric refrigerator is shown in Figure 1.2(a). The left and right legs are taken to be p- and n-type thermoelectric materials, respectively. The temperatures of the source and sink are T_C and T_H, respectively. By
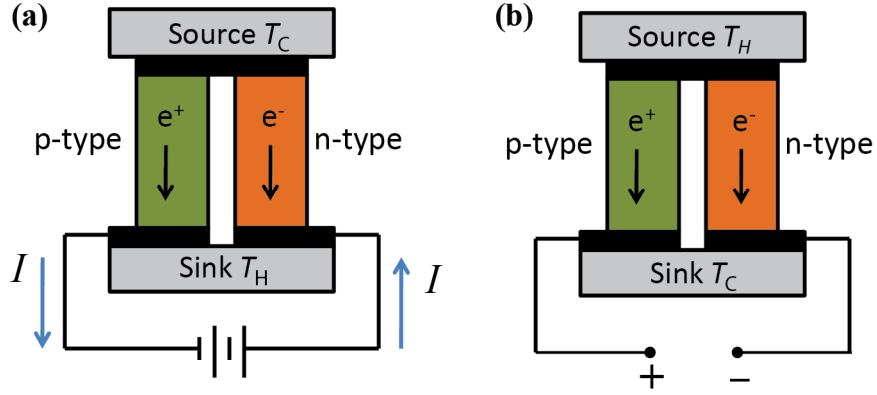
Figure 1.2: Schematic of (a) a thermoelectric refrigerator and (b) a thermoelectric power generator.

passing a current I through the device, heat flows from top to bottom (reversing the direction of current reverses the direction of heat flow). The efficiency of this device is defined as the ratio of the rate of cooling of the source to the total power consumption:

$$\phi = \frac{Q_{cooling}}{W_{consumed}}. \tag{1.3}$$

Taking into account the heat carried by the Peltier current, as well as the opposing Joule heating ($I^2 R$) and heat flow as the result of the temperature gradient created ($\kappa \Delta T$), we find that

$$Q_{cooling} = S_{pn} I T_C - \kappa \Delta T - \frac{1}{2} I^2 R \tag{1.4}$$

where κ is the total thermal conductance and R the total electrical resistance of the device. The total power consumed is a sum of the Joule power and the additional power required to overcome the Seebeck voltage created:

$$W_{consumed} = I^2 R + S_{pn} I \Delta T. \tag{1.5}$$

At the optimal current value, the device efficiency is then

$$\phi_{opt} = \left[\frac{T_{avg}}{\Delta T} \left(\frac{\sqrt{1+ZT_{avg}}+1}{\sqrt{1+ZT_{avg}}-1} \right) + \frac{1}{2} \right]^{-1} \qquad (1.6)$$

where $T_{avg} = (T_C + T_H)/2$ and the quantity

$$Z = \frac{S_{pn}^2}{R\kappa}, \qquad (1.7)$$

which has units of 1/K, depends on the shape, size and material properties of the legs. The full derivation for Eq. (1.6) can be found in [24]. With the appropriate choice of leg geometries to maximize the device efficiency, the quantity Z reduces to

$$Z_{max} = \frac{S_{pn}^2}{\left(\left(\frac{\kappa_p}{\sigma_p} \right)^{1/2} + \left(\frac{\kappa_n}{\sigma_n} \right)^{1/2} \right)^2}. \qquad (1.8)$$

We note that Z_{max} depends only on the properties of leg materials: the thermal (κ_i) and electrical (σ_i) conductivities of the two materials and the Seebeck coefficient of the junction.

A schematic of a thermoelectric power generator is shown in Figure 1.2(b). In this case, a voltage is created by placing the device across a temperature gradient (between the heat source at T_H and heat sink at T_C). An analogous argument for the optimal device efficiency of a power generator yields

$$\eta_{opt} = \frac{T_{avg}}{\Delta T} \left(\frac{\sqrt{1+ZT_{avg}}-1}{\sqrt{1+ZT_{avg}}+1} \right) - \frac{1}{2} \qquad (1.9)$$

The maximized efficiencies (as well as the efficiencies of the refrigerator at maximum heat pumping and of the power generator at maximum power output) are increasing functions of Z_{max}, which depends on the pair of materials chosen. As such, Z_{max} is referred to as the thermoelectric figure-of-merit. Though Z_{max} in Eq. (1.8) is

given for the device, in practice we evaluate thermoelectric transport in individual materials via

$$Z = \frac{S^2 \sigma}{\kappa} \tag{1.10}$$

where the thermal conductivity is a sum of the electronic (κ_e) and lattice (κ_l) contributions. We note that the dimensionless quantity *ZT* is also frequently reported.[24]

Eq. (1.10) indicates that a good thermoelectric material has a high Seebeck coefficient *S*, a high electrical conductivity σ and a low thermal conductivity κ. In general, however, these 3 parameters are related, and cannot be optimized individually. An increase in electrical conductivity generally corresponds to an increase in the electronic contribution to thermal conductivity (via the Wiedemann-Franz law), as well as a decrease in the Seebeck coefficient. Because of this unfavorable coupling between transport properties, the best room temperature *ZT*
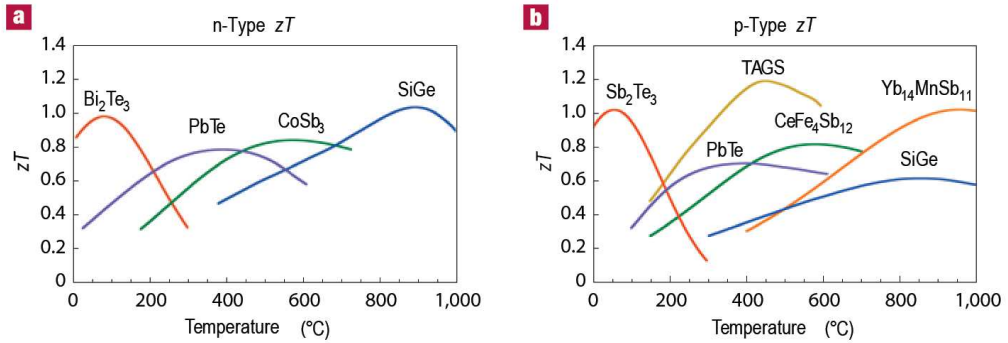
Figure 1.3: State-of-the-art *ZT* values of (a) n-type and (b) p-type materials as of 2008.[2]
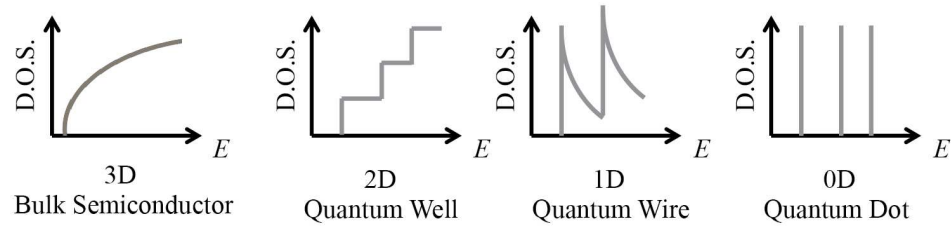
Figure 1.4: Schematics of electron density-of-states functions for various system dimensions, adapted from [3].

values of bulk materials are around 1 (see Figure 1.3), with not much improvement over the last 50 years of research.[24]

1.4 *Nanostructured Thermoelectrics*

In 1993, pioneering theoretical work by Hicks and Dresselhaus[18, 19] indicated that confining a material to a one-dimensional nanowire or a two-dimensional thin film could mean significant increases in *ZT* values relative to bulk. The predicted improvement is the result of two important effects when moving from bulk to the nanoscale: (1) the resulting quantization of the electronic density-of-states function (Figure 1.4) was expected to lead to an increase in the thermoelectric power factor (σS^2, the numerator of *Z*), and (2) an increase in phonon scattering by nanoscale features should mean a decrease in the lattice contribution to the thermal conductivity, κ_l.

1.4.1 Models of Hicks and Dresselhaus

The original models of Hicks and Dresselhaus were derived for highly confined (very small) systems, in which the separation between quantized energy levels (which are proportional to w^{-2}, where w is the size of the nanostructure) is large enough that only a single subband energy contributes to transport.[18, 19] We will refer to this model as the "single-subband model", described in additional detail below. Using the single subband model, Hicks and Dresselhaus calculated the room temperature ZT values of Bi_2Te_3 thin films and square nanowires as a function of film thickness and nanowire width, respectively. These results are shown in Figure 1.5.

Huge ZT values (~7 for 2D, ~14 for 1D) are seen for the smallest structures (<1nm in size): a significant improvement over the bulk value of ~0.5. For both 2D and 1D systems (regardless of film or nanowire orientation), ZT increases monotonically with decreasing size—leading to the initial conclusion that smaller
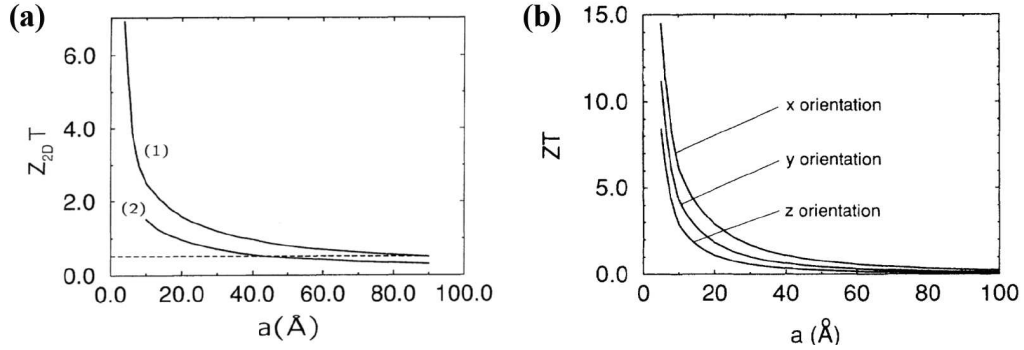
Figure 1.5: ZT values calculated using the single-subband model as a function of film thickness and nanowire radius for (a) Bi_2Te_3 quantum wells and (b) Bi_2Te_3 quantum wires of various crystallographic orientations. Taken from [18, 19].

structures are always better. However, two things should be noted from these results: (1) The sizes investigated in this work are very small, for the most part falling below the experimentally accessible size range and (2) *ZT* does not approach the bulk value as the structure size increases; rather, *ZT* goes asymptotically to zero as the size goes to infinity. This indicates a need for further theoretical investigation into thermoelectric transport in the intermediate size range between ~10nm and bulk.

1.4.2 Experimental Demonstration of High *ZT* Nanostructured

Thermoelectrics

Since the ground-breaking theoretical work done by Hicks and Dresselhaus, improvements in fabrication, characterization and measurement techniques at the nanoscale have led to significant progress in the field of nanostructured thermoelectrics. These improvements include advances in techniques for wet chemical synthesis of nanoparticles, nanowire growth, thin film deposition, and improved resolution in electron microscopies (making it possible both to image and to pattern smaller and smaller features). With these enhanced experimental methods, many groups have demonstrated increased *ZT* values in nanostructures relative to bulk. Several of the systems showing the most substantial improvements in *ZT* are highlighted below.

In 2001, Venkatasubramanian *et al*. reported a cross-plane *ZT* value of 2.4 in a p-type Bi_2Te_3/Sb_2Te_3 superlattice structure at room temperature[25]—a significant improvement over commercially available $Bi_{2-x}Sb_xTe_3$ alloys (*ZT*~0.8). They found that the lattice thermal conductivity is minimized for a superlattice period of 6nm, regardless of the thickness of the individual layers, with little impact on electron
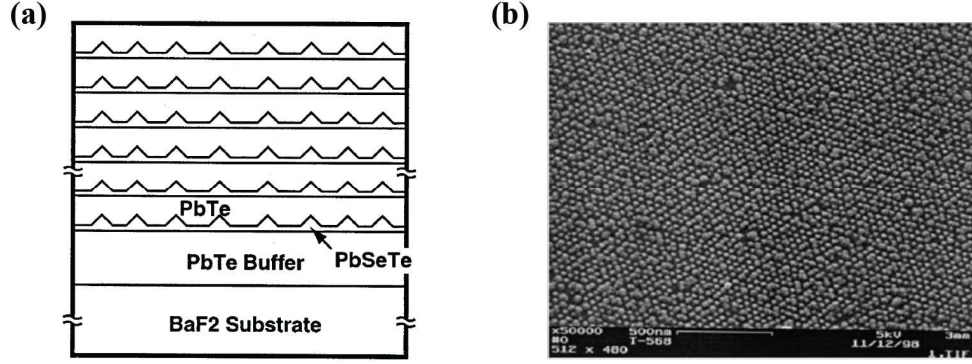
Figure 1.6: (a) Cross-sectional schematic and (b) top surface SEM image of the PbSe$_{1-x}$Te$_x$/PbTe quantum dot superlattice (QDSL) structure.[6]
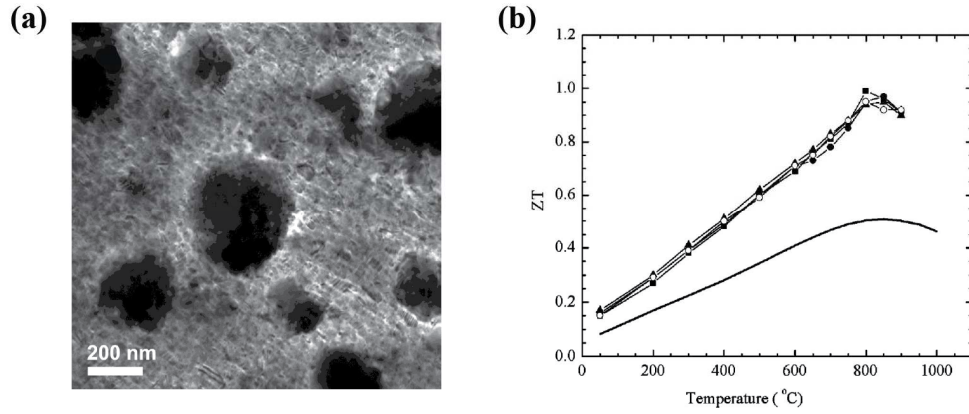
Figure 1.7: (a) TEM image of a hot-pressed nanostructured bulk Si-Ge alloy, (b) *ZT* values of hot-pressed samples (shown with various markers) compared with state-of-the-art bulk (solid line) as a function of temperature.[17]

transport. Shortly thereafter, Harman *et al*. demonstrated room temperature in-plane *ZT* values between 1.3 and 1.6 for devices based on PbSe$_{1-x}$Te$_x$/PbTe quantum dot superlattice structures (Figure 1.6).[6, 26]

More recently, improvements in *ZT* have also been shown in nanostructured bulk alloys. Joshi *et al*. demonstrated a 50% increase in the high temperature (800-
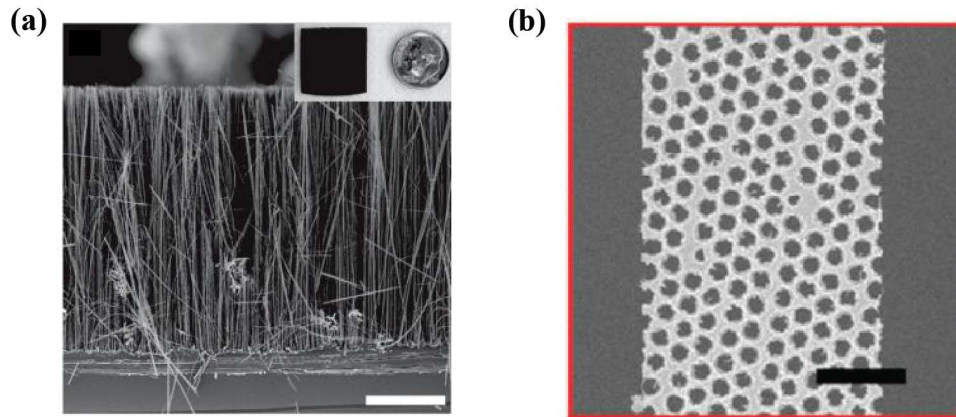
Figure 1.8: (a) Cross-sectional SEM image of rough Si nanowires (scale bar:10um)[8] and (b) SEM image of a holey Si nanoribbons (scale bar:1um).[13]

900 C) *ZT* value of the Si-Ge alloy system. Si and Ge powders are mechanically alloyed using a ball milling technique, and the resulting nanopowder is hot pressed to form a bulk pellet (Figure 1.7).[17] The high density of nanoscale interfaces created through the ball milling, hot pressing process leads to a reduction of almost 50% in the thermal conductivity relative to bulk, and a slight increase in the power factor. A similar process was used by Poudel *et al.* to synthesize a nanostructured bulk $Bi_{2-x}Sb_xTe_3$ alloy with a low temperature (100 C) *ZT* value of 1.4—a 40% increase over a comparable bulk alloy. The increase in *ZT* is in large part due to a 50% decrease in the lattice thermal conductivity, as well as a slight increase in electrical conductivity attributed to charge build-up at the grain boundaries and a resulting increase in hole density within the grains.[27]

One of the materials perhaps best suited for nanostructuring is Si, which exhibits such a large thermal conductivity in bulk (~110W/m-K) that thermoelectric application is impractical. Techniques including bulk nanostructuring[28], synthesis

of nanowires[8, 29] and fabrication of holey ribbons[13] (see Figure 1.8) have led to significant reductions in the thermal conductivity of Si (as low as 1.6W/m-K at room temperature), giving rise to a factor of 60 improvement in *ZT*.

The measured room temperature transport properties of several of the nanostructured systems mentioned in this section are listed in Table I and compared with their bulk counterparts.

Table I. Measured transport properties of various nanostructure and bulk thermoelectric systems at room temperature.

Material	Structure	Power Factor (10^{-3} W/m-K^2)	Total Thermal Conductivity (W/m-K)	*ZT*
Si	Nanowire (1)	3.3[8]	1.6	0.6
	Nanowire (2)	2.9[29]	2.5	0.25
	Bulk	4.0[30]	110	0.01
$PbSe_{1-x}Te_x$	Quantum dot superlattice	3.1[26]	0.58	1.6
	Bulk PbTe	4.6[31]	2.3	0.52
$Bi_{2-x}Sb_xTe_3$	Nanostructured bulk	4.3[27]	1.1	1.2
	Bulk	4.5[27]	1.4	0.9

These results indicate that while substantial increases in *ZT* have been realized, these improvements are almost always due to a significant decrease in the thermal conductivity. In fact, in the majority of investigated materials systems the power factor of nanostructures actually falls below the bulk value. In systems for which modest improvements in power factor are reported, this is usually attributed to secondary effects, rather than modification of the electron density-of-states as the

result of confinement. These results are in stark contrast to the original predictions of Hicks and Dresselhaus, indicating the need to further improve our understanding of electron transport in nanostructured systems.

1.5 *Objectives of Thesis*

The objectives of this thesis are as follows.

1. *To resolve the discrepancy between experimental and theoretical work:*

The theory that the thermoelectric power factor of nanostructures should be larger than that of bulk has dominated the field for the last 20 years. Experimental results from a wide variety of materials systems disagree with this conclusion, which was based on the preliminary modeling work of Hicks and Dresselhaus. The first goal of this work is to resolve this discrepancy between experimental and theoretical work. We develop new models for calculation of the thermoelectric transport properties of nanostructures, and apply these models to a wide range of materials systems. We then derive universal scaling relations for the thermoelectric power factor that allow us to calculate the power factor value of any simple nanostructure (nanowire and thin film) in any configuration (material, size, temperature) *without any additional computational effort*.

2. *To explore new techniques for demonstrating high values of the thermoelectric power factor in nanostructures:*

The modeling work described above suggests that demonstrating high power factor values in "simple" nanostructures (nanowires and thin films) may prove difficult. Calculations done for thermoelectric nanostructures in which the scattering time is a function of the carrier energy indicate that the introduction of a scattering

mechanism with a preferable energy-dependence could be a potential means for improving the power factor in these simple nanostructures. In experimental systems, this can be realized by the introduction of additional nanoscale grain boundaries, either through the introduction of nanoparticles or nanopores.

We then set out to experimentally verify these theoretical predictions by fabricating porous thin films. The model thermoelectric materials system $Bi_{2-x}Sb_xTe_3$ was utilized for this study. Porous thin films were deposited onto anodic alumina templates using pulsed laser deposition, and the room temperature transport properties were measured using set-ups in our lab.

1.6 Organization of Thesis

This thesis consists of 8 chapters in addition to the introduction. The content of these chapters is summarized below.

Chapter 2: A model for calculation of the thermoelectric transport properties of cylindrical nanowires is presented, and calculations done for n-type InSb are reported. We compare results calculated using our model to those calculated using the model of Hicks and Dresselhaus, and discuss the validity of the Hicks and Dresselhaus model in the range of sizes of interest here.

Chapter 3: In this chapter, models for calculation of the transport properties of square nanowires and thin films are presented and applied to n-type InSb. These models are then applied to a range of systems with varying material parameters and temperatures, and we discuss the general behavior of the size-dependent power factor of nanostructures within this framework.

Chapter 4: We use the analytical forms of the transport properties of nanowires and thin films to derive universal scaling relations for the power factor. These equations allow us to determine the power factor of any simple nanostructured system without any additional computational effort. The universal scaling relations analytically illustrate the dependence of the power factor on size; the effects of choice of material and temperature on the power factor follow naturally from these derivations.

Chapter 5: The effect of an energy-dependent scattering time on the transport properties of nanostructures is investigated. The potential for improving the power factor through the intentional introduction of carrier scattering centers is discussed.

Chapter 6: This chapter focuses on the experimental techniques developed to both fabricate and characterize thermoelectric thin films. This includes a description of the dual pulsed laser deposition, thermal evaporation system in our lab as well as the set-ups built for measurement of the thermoelectric transport properties.

Chapter 7: In this chapter, we investigate pulsed laser deposition of $Bi_{2-x}Sb_xTe_3$ thin films. The effects of various deposition and annealing conditions on the properties of the films are explored, and an optimized set of process conditions is identified.

 Chapter 8: We present a study of templated deposition of porous $Bi_{2-x}Sb_xTe_3$ thin films. These films were produced by a method described herein. The properties of porous and dense films deposited using this method are compared.

Chapter 9: The final chapter includes general conclusions on the research presented in this thesis, and offers a vision for future work.

Chapter 2 Thermoelectric Transport in Cylindrical InSb Nanowires

2.1 *Introduction*

The thermoelectric transport properties of a material are a complex function of many material and system parameters, including the types, characteristics and concentration of carriers, crystallographic orientation, and temperature. In lieu of huge amounts of costly experimental work, theoretical modeling of the transport properties is crucial for sifting through this wide parameter space in order to find materials of interest, and predict ideal configurations (e.g. carrier concentration or range of ideal operation temperatures) in which the thermoelectric properties of these materials are optimized.[32-35] This is especially true when investigating nanostructured materials, which are often more challenging to fabricate and characterize.[36-38] Predictive models for the transport properties of nanostructured materials are therefore vital as we explore potential applications of nanotechnology to thermoelectric systems.

In this chapter, a model for calculation of the transport properties of cylindrical InSb nanowires is presented. The theoretical approach presented here is based on the model developed by Hicks and Dresselhaus for calculation of the transport properties of nanowires. The initial computational work of Hicks and Dresselhaus predicted huge improvements in *ZT* when moving from bulk to nano-scale systems, due to an increase in the thermoelectric power factor ($PF = \sigma S^2$) and a

decrease in the lattice thermal conductivity κ_l. Experimental work over the last 20 years, jumpstarted by the initial conclusion that "Smaller is always better", has shown that while κ_l for nanostructures can be far lower than the bulk value, the power factor shows no improvement with nanostructuring. The computation model presented in this chapter was therefore motivated by the need to resolve the discrepancy between modeling and experimental results in the field of thermoelectrics.

The assumptions made in the original model of Hicks and Dresselhaus, which was derived for *highly confined (very small) systems,* are not suitable for the range of sizes of interest here (nanowire radii between 10 and 100nm). The model derived here is therefore designed to take into account the changing physics when moving between highly confined nanowire systems (radii smaller than ~12nm) to nanowire systems exhibiting bulk-like transport properties (radii larger than ~100nm).

The model presented in this chapter involves calculating the electronic subband structure of the nanowire systems and solving the Boltzmann transport equation in order to derive the 1D thermoelectric transport properties with this subband structure as an input. Following the model description, radius-dependent power factor and *ZT* values calculated for n-type InSb nanowires are reported. The results of the model derived here offer a new outlook for the field of nanostructured thermoelectric materials: In general, the nanowire power factor actually falls below the bulk value (smaller is not always better).

2.2 General Expressions for the Thermoelectric Transport Properties

The thermoelectric transport properties (electrical conductivity σ, Seebeck coefficient S and electronic thermal conductivity κ_e) of cylindrical InSb nanowires

are calculated by solving the semi-classical equations of motion in the presence of an electric field and a temperature gradient. We start by deriving general expressions for the thermoelectric transport properties of materials within this formalism, and then derive equations specific to 1D systems (Sect. 2.3) and 3D systems (Sect. 2.4). The derivations given here are brief; a much more thorough treatment can be found in [39].

The semi-classical equations of motion of an electron at position $\mathbf{r}$ in a spatially uniform and static electric field $\mathbf{E}$ are given by

$$\dot{\mathbf{r}} = v(\mathbf{k}) = \frac{1}{\hbar}\frac{\partial E(\mathbf{k})}{\partial \mathbf{k}} \tag{2.1}$$

$$\hbar\dot{\mathbf{k}} = -e\mathbf{E}$$

where $\mathbf{k}$ is the electron wavevector, $v(\mathbf{k})$ is the electron group velocity, $\hbar$ is the reduced Planck's constant $h/2\pi$, $E(\mathbf{k})$ is the dispersion relation and e is the charge of an electron. The electric current density $\mathbf{j}$ and the thermal current density $\mathbf{j_q}$ can be written as

$$\mathbf{j} = -e \int \frac{d\mathbf{k}}{4\pi^3} v(\mathbf{k})g(\mathbf{k}) \tag{2.2}$$

$$\mathbf{j_q} = \int \frac{d\mathbf{k}}{4\pi^3}\left[E(\mathbf{k}) - E_f\right]v(\mathbf{k})g(\mathbf{k})$$

where $g(\mathbf{k})$ is the non-equilibrium distribution function and E_f is the Fermi energy. In the presence of the electric field $\mathbf{E}$ and a constant temperature gradient ∇T, $g(\mathbf{k})$ differs from the equilibrium distribution function $g_0(\mathbf{k})$ via

$$g(\mathbf{k}) = g_0(\mathbf{k}) + \tau(E(\mathbf{k}))\left(-\frac{\partial f}{\partial E}\right)v(\mathbf{k})\left[-e\mathbf{E} + \frac{E(\mathbf{k})-E_f}{T}(-\nabla T)\right]. \tag{2.3}$$

In Eq. (2.3), $\tau(E(\mathbf{k}))$ is the relaxation time, f is the Fermi-Dirac distribution and T is the temperature. The non-equilibrium distribution function in Eq. (2.3) is derived

18

within the framework of the relaxation time approximation. Physically, this approximation means that it is only through various scattering processes that the system returns to equilibrium in time $\tau(E(\mathbf{k}))$. This is generally appropriate for thermoelectric materials (which tend to be doped semiconductors) at room temperature, for which the dominant carrier scattering mechanisms are elastic processes.[24] Detailed models for calculation of the non-equilibrium distribution function in the presence of inelastic scattering processes are described in [35, 40, 41]. Plugging Eq. (2.3) into Eq. (2.2) and noting that by definition the equilibrium distribution function does not contribute to currents gives the following expressions for the electrical and thermal current densities:

$$\mathbf{j} = \mathbf{L}^{(0)}\mathbf{E} - \frac{1}{eT}\mathbf{L}^{(1)}(-\nabla T) \tag{2.4}$$

$$\mathbf{j_q} = -\frac{1}{eT}\mathbf{L}^{(1)}\mathbf{E} + \frac{1}{e^2 T}\mathbf{L}^{(2)}(-\nabla T)$$

where the "L-integrals" are defined as

$$\mathbf{L}^{(\alpha)} = e^2 \int \frac{d\mathbf{k}}{4\pi^3}\left(-\frac{\partial f}{\partial E}\right)\tau(E(\mathbf{k}))\,v(\mathbf{k})v(\mathbf{k})\big(E(\mathbf{k}) - E_f\big)^\alpha. \tag{2.5}$$

The electrical conductivity, Seebeck coefficient and electronic thermal conductivity can then be solved for as

$$\sigma = \mathbf{j}\cdot\mathbf{E}^{-1}\big|_{\nabla T=0} = \mathbf{L}^{(0)}$$

$$S = \mathbf{E}\cdot(\nabla T)^{-1}\big|_{\mathbf{j}=0} = -\mathbf{L}^{(1)}/\big(eT\cdot\mathbf{L}^{(0)}\big) \tag{2.6}$$

$$\kappa_e = \mathbf{j_q}\cdot(\nabla T)^{-1}\big|_{\mathbf{j}=0} = \left(\frac{1}{e^2 T}\right)\left(\mathbf{L}^{(2)} - \frac{(\mathbf{L}^{(1)})^2}{\mathbf{L}^{(0)}}\right).$$

We note that the derivation given above assumed a single band in the electronic structure of the material. If multiple bands are relevant when calculating the transport properties, the quantity $\mathbf{L}^{(\alpha)}$ becomes a sum over the contributions of each band:

19

$$\mathbf{L}^{(\alpha)} = \sum_{\text{band}} \mathbf{L}_{\text{band}}^{(\alpha)}. \tag{2.7}$$

Calculation of the thermoelectric transport properties requires knowledge of the band structure $E(\mathbf{k})$ of the material. For the model derived here, we take the effective mass approximation (considering only carriers near the extrema of the conduction and valence bands).[39] In the interest of simplicity and ease of extension to a wide range of materials, we will assume a single conduction band characterized by an ellipsoidal Fermi surface. The effective mass along the x-direction, the direction of transport, is denoted $m_{\parallel}^*$ and effective masses along the y- and z-directions, which are taken to be equal, are denoted $m_{\perp}^*$. The dispersion relation for this band, assumed to have a parabolic form, is then given by $E(\mathbf{k}) = \frac{\hbar^2}{2}\left(\frac{k_x^2}{m_{\parallel}^*} + \frac{k_y^2 + k_z^2}{m_{\perp}^*}\right)$, where k_i is the wavevector in the i direction. These approximations are appropriate for n-type InSb, the materials system investigated in this chapter. The band structure for InSb is shown in Figure 2.1. The 3 conduction band minima of InSb closest to the Fermi energy are located at the Γ, L and X points of the Brillouin zone. The L and X valleys lie at high enough energies (~0.5 and 0.8eV) relative to the Γ valley that we can consider n-type InSb a single-carrier material at room temperature, with electrons occupying only the Γ valley. The bandgap of InSb, 0.17eV at room temperature, is large enough that to a first approximation we assume that there is no electron transport due to holes in the valence bands.

This model can easily be extended to more complex band structures. For example, for systems in which multiple bands (including both electrons and holes) must be considered, the contributions of these bands are summed in Eq. (2.7). For systems in which interactions between the conduction and valence bands lead to a
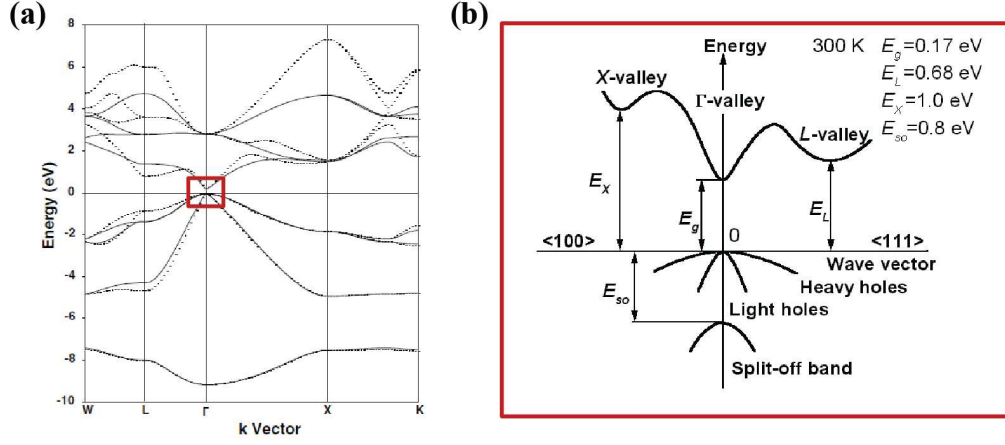
Figure 2.1: (a) Band structure calculations for InSb, taken from [14]. The Fermi energy is marked by a horizontal line at Energy=0. (b) Schematic of the key features of the InSb band structure [20]. Note that the wavevector axes for these two plots are reversed.

deviation from the parabolic dispersion relation[42], a more accurate form of $E(\mathbf{k})$ may be plugged into Eq. (2.5).

In order to emphasize the effects of the electronic structure on transport, the "L-integrals" from this point forward will be given as a function of electron energy, as opposed to wavevector. This change of variables, done assuming that the k_i wavevectors are independent of one another, is detailed in [43].

2.3 Transport in 1D

In this section, the model used for calculation of the subband structure of InSb nanowires as well as the one-dimensional form of Eq. (2.3) are presented. The derivations given here are brief; detailed derivations for these equations can be found in [43].

2.3.1 Modeling the Subband Structure of Cylindrical Nanowires

For nanowire systems, we take the x-direction to be the direction of transport, aligned with the axis of the nanowire. As a result of confinement by the nanowire boundary, the wavevectors in the y- and z-directions are quantized. In order to calculate the dispersion relations for nanowire systems (given by $E(\mathbf{k}) = \frac{\hbar^2}{2}\left(\frac{k_x^2}{m_\parallel^*} + \frac{k_y^2+k_z^2}{m_\perp^*}\right)$ in bulk), we must first determine the allowed values of k_y and k_z by solving the Schrodinger equation for electrons in a confining potential.

From the effective mass theorem, the Schrodinger equation for electrons in a solid has the general form:

$$-\frac{\hbar^2}{2}\nabla \cdot \boldsymbol{\alpha} \cdot \nabla \boldsymbol{\psi}(\mathbf{r}) + V(\mathbf{r})\boldsymbol{\psi}(\mathbf{r}) = E\boldsymbol{\psi}(\mathbf{r}) \tag{2.8}$$

where $\boldsymbol{\alpha}$ is the inverse effective mass tensor, $\mathbf{r}$ is the position, $V(\mathbf{r})$ is the confining potential created by the nanowire boundary, $\boldsymbol{\psi}(\mathbf{r})$ is the electron wave function and E is the electron eigen-energy. With the simple band structure described above, $\boldsymbol{\alpha}$ is given by

$$\boldsymbol{\alpha} = \begin{bmatrix} \left(m_\parallel^*\right)^{-1} & 0 & 0 \\ 0 & (m_\perp^*)^{-1} & 0 \\ 0 & 0 & (m_\perp^*)^{-1} \end{bmatrix}. \tag{2.9}$$

For a cylindrical nanowire of radius r, we assume the following piece-wise form of the confining potential:

$$V(\rho,\theta,z) = \begin{cases} 0 & \text{for } \rho < r \\ \infty & \text{for } \rho > r \end{cases} \tag{2.10}$$

where ρ, θ, x is the position in cylindrical coordinates defined in Figure 2.2.
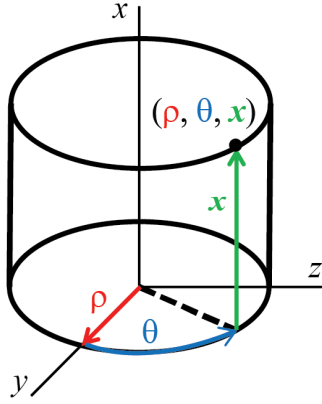
Figure 2.2: Cylindrical coordinate system.

The imposed boundary conditions are that $\psi(\mathbf{r})$ vanishes at the nanowire boundary ($\rho = r$) and remains finite at the center of the nanowire ($\rho = 0$).

With the effective mass tensor in Eq. (2.9), the general solution to Eq. (2.8) for a wave traveling in the x-direction and bounded in the y and z directions has the form

$$\psi(\mathbf{r}) = U(\rho, \theta) \cdot \exp(ik_x x). \tag{2.11}$$

Plugging (2.11) and (2.9) into (2.8), the Schrodinger equation simplifies to a two-dimensional differential equation for the function $U(\rho, \theta)$:

$$-\frac{\hbar^2}{2m_\perp^*}\left(\frac{\partial^2}{\partial \rho^2} + \frac{1}{\rho}\frac{\partial}{\partial \rho} + \frac{1}{\rho^2}\frac{\partial^2}{\partial \theta^2}\right) U = \left[E - \frac{\hbar^2 k_x^2}{2m_\parallel^*}\right] \cdot U \tag{2.12}$$

The eigen-energy solutions of Eq. (2.12), referred to as the "subband energies", are the quantized energy levels resulting from confinement in the y and z directions and are given by

$$E_{nm} = E - \frac{\hbar^2 k_x^2}{2m_\parallel^*} = \frac{j_{mn}^2 \hbar^2}{2m_\perp^* r^2}, \tag{2.13}$$
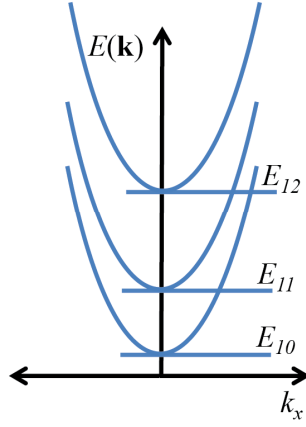
Figure 2.3: Nanowire subband structure with first 3 subband energies labeled.

where j_{nm} is the nth root of the mth-order Bessel function of the first kind.[44] The subband dispersion relations can then be written

$$E(\mathbf{k}) = E_{nm}(k_x) = \frac{\hbar^2 k_x^2}{2m_\parallel^*} + E_{nm}. \qquad (2.14)$$

The subband energy E_{nm}, therefore marks the bottom edge (k_x=0) of the subband dispersion relation (see Figure 2.3). We note that this analytical solution for the subband energies exists due to the rotational symmetry of the single carrier pocket assumed here (see Eq. (2.9)); numerical methods for calculating nanowire subband structures for Fermi surfaces of lower symmetry have been described elsewhere.[45]

2.3.2 Thermoelectric Transport Properties in 1D

Thermoelectric transport properties can then be calculated from the following one-dimensional form of Eq. (2.5):

$$\mathbf{L}^{(\alpha)} = \sum_{nm} 2 \frac{e^2}{\pi^2 r^2 \hbar} \sqrt{\frac{2}{m_\parallel^*}} \int_{E_{nm}}^{\infty} dE \cdot \tau(E) \sqrt{E - E_{nm}} \cdot \left(-\frac{\partial f}{\partial E}\right) \cdot \left(E - E_f\right)^{\alpha}. \qquad (2.15)$$

where all energies are taken relative to the band edge of bulk and the summation in

Eq. (2.15) is taken over the contributions of all subbands.

2.4 *Transport in 3D*

In order to determine the effect of nanowire confinement on the thermoelectric transport relative to bulk InSb, transport properties were also calculated for bulk. For a 3D material, Eq. (2.5) can be written as[43]

$$\mathbf{L}^{(\alpha)} = \frac{e^2 m_\perp^*}{3\pi^2 \hbar^3} \sqrt{\frac{8}{m_\parallel^*}} \int_0^\infty dE \cdot \tau(E) \sqrt{E^3} \cdot \left(-\frac{\partial f}{\partial E}\right) \cdot \left(E - E_f\right)^\alpha \tag{2.16}$$

where again all energies are taken relative to the band edge. As with the model presented for 1D, Eq. (2.16) was derived assuming a single conduction band, characterized by effective masses $m_\parallel^*$ (along the direction of transport) and $m_\perp^*$ (perpendicular to transport).

In order to keep the derivations presented in this chapter general, Eq. (2.15) and (2.16) are written without specifying the energy-dependence of the scattering time. For all results presented below, we will assume a carrier relaxation time constant with respect to energy ($\tau(E) = \tau = \mu m_\parallel^*/e$, where μ is the carrier mobility along the transport direction). We have taken this simple approach to scattering time in order to investigate the underlying physics of thermoelectric transport in nanowires without extensive material-specific adjustments to the model. Clearly this approach would not be appropriate for all systems; it is evident from Eq. (2.15) and (2.16), however, that this model can easily be extended to systems with an energy-dependent scattering time (this is discussed in detail in Chapter 3).

2.5 Procedure for Calculation of the Thermoelectric Transport Properties of InSb

Nanowires

We investigate n-type InSb, a promising thermoelectric material in bulk.[46] The material parameters used (electron effective mass m^*=0.013m_0, electron mobility μ=70,000cm^2/(V-s)) were obtained from the literature.[47, 48] The nanowire radius was varied in the range of 10-100nm.

For each nanowire radius r investigated, calculations of the thermoelectric transport properties at room temperature were done using the following procedure:

1. The lowest 300 subband energies are determined via Eq. (2.13). The calculations are limited to 300 subbands (despite the fact that the real electronic structure includes an infinite number) because, as is shown in more detail below, 300 subbands are enough to accurately model transport in the nanowire systems studied here.

2. For each of the 300 subband energies calculated in Step 1, we evaluate the **L**$^{(\alpha)}$-integrals in Eq. (2.15) as a function of Fermi energy. The total **L**$^{(\alpha)}$-integral for a given Fermi energy is then a sum over the contributions of each individual subband.

3. The **L**$^{(\alpha)}$-integrals are then plugged into the expressions in Eq. (2.6), giving the 3 transport properties $\sigma(E_f)$, $S(E_f)$, $\kappa_e(E_f)$ as a function of Fermi energy.

4. The power factor is calculated as a function of Fermi energy ($PF = \sigma S^2$), and the Fermi energy that maximizes the power factor $E_{f,opt}$ is identified.

An example of the thermoelectric power factor ($PF = \sigma S^2$) of a nanowire calculated as a function of Fermi energy is given in Figure 2.4 for r=10nm. The first
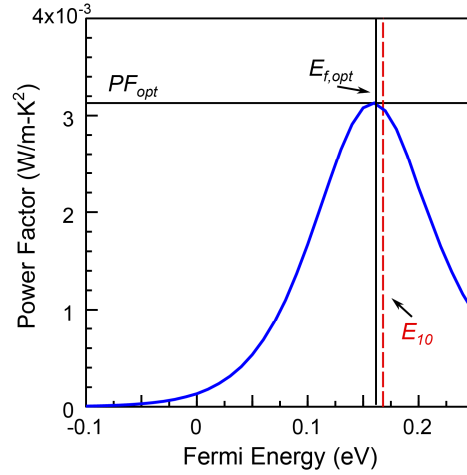
Figure 2.4: Calculated power factor as a function of Fermi energy for an InSb nanowire with r=10nm. Vertical lines mark the 1st subband energy (E_{10}) and the optimal Fermi energy ($E_{f,opt}$). The conduction band edge of bulk is set at E=0.

subband energy (E_{10}), the Fermi energy for which the power factor is maximized ($E_{f,opt}$) and the maximum power factor value (PF_{opt}) are labeled in this plot. Note that the power factor exhibits a maximum with respect to Fermi energy—this is because the power factor is the product of the electrical conductivity, which increases monotonically with Fermi energy, and the square of the Seebeck coefficient, which generally decreases with Fermi energy.

The room temperature transport properties of bulk InSb were also calculated as a function of Fermi energy, using Eq. (2.16) and (2.6) (Figure 2.5). With the optimization condition E_f=$E_{f,opt}$, the bulk power factor value for InSb is calculated to be 2.54x10^{-3} W/m-K^2, in good agreement with the experimental value of 2.0 x10^{-3} W/m-K^2.[46]
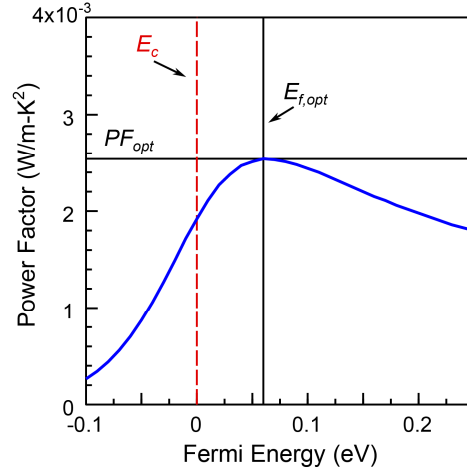
Figure 2.5: Calculated power factor as a function of Fermi energy for bulk InSb. Vertical lines mark the conduction band edge (E_c) and the optimal Fermi energy ($E_{f,opt}$).

2.6 Single-Subband Model of Hicks and Dresselhaus

We first present results calculated using the "single-subband model" developed by Hicks and Dresselhaus. With this model, we ignore the sum over the contribution of multiple subbands in Eq. (2.15). Without this summation, only the contribution of the lowest subband at E_{10} is considered. Power factor values calculated using the single-subband model are given as a function of nanowire radius in Figure 2.6. This curve displays a r^{-2} dependence, similar to what was calculated by Hicks and Dresselhaus for Bi_2Te_3 and shown in Figure 1.5. We note that, as with the data shown in Figure 1.5, the results calculated with the single-subband model do not approach the bulk value (marked by a dashed line in Figure 2.6) for large nanowire radii.

28
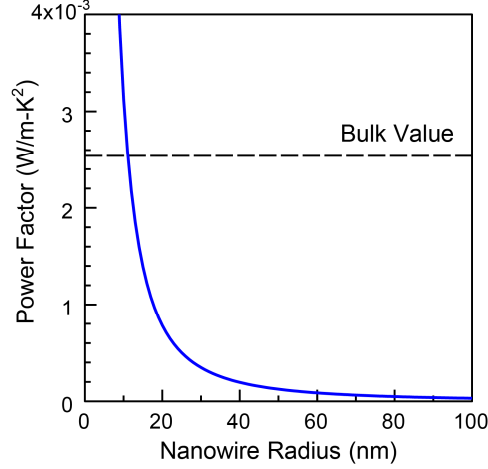
Figure 2.6: Calculated power factor values as a function of nanowire radius using the single-subband model. The bulk calculated value is marked by a dashed horizontal line. n-type InSb band parameters were used.

The r^{-2} dependence of the power factor calculated using the single-subband model is explained as follows. From Eq. (2.6), the power factor can be written in terms of the "L-integrals" as

$$PF = \sigma S^2 = \left(\frac{1}{eT}\right)^2 \frac{\left(\mathbf{L}^{(1)}\right)^2}{\mathbf{L}^{(0)}}. \tag{2.17}$$

The nanowire power factor can therefore be determined by plugging (2.15) into (2.17) to get

$$PF\left(r, E_f\right) = \left\{2\frac{\mu}{\pi^2 r^2 \hbar} \cdot \frac{\sqrt{2m_\parallel^*}}{eT^2}\right\} \left[\frac{\left[\sum_{nm}\int_{E_{nm}}^{\infty} dE \cdot \sqrt{E - E_{nm}} \cdot \left(-\frac{\partial f}{\partial E}\right) \cdot \left(E - E_f\right)\right]^2}{\sum_{nm}\int_{E_{nm}}^{\infty} dE \cdot \sqrt{E - E_{nm}} \cdot \left(-\frac{\partial f}{\partial E}\right)}\right]. \tag{2.18}$$

The power factor depends on nanowire radius (1) directly through the r^{-2} factor in the energy-independent coefficient (surrounded by {}), and (2) indirectly through the ratio of integrals (surrounded by []), which depend on the set of subband energies $E_{nm}(r)$. Assuming that the conduction band consists of a single subband E_{10}, the ratio of integrals $A(r, E_f)$ can be written as

$$A(r, E_f) = \frac{\left[\int_{E_{10}}^{\infty} dE \cdot \sqrt{E - E_{10}} \cdot \left(-\frac{\partial f}{\partial E}\right) \cdot (E - E_f)\right]^2}{\int_{E_{10}}^{\infty} dE \cdot \sqrt{E - E_{10}} \cdot \left(-\frac{\partial f}{\partial E}\right)} \tag{2.19}$$

such that $PF(r, E_f) = \left\{ 2\frac{\mu}{\pi^2 r^2 \hbar} \cdot \frac{\sqrt{2m_{\parallel}^*}}{eT^2} \right\} A(r, E_f)$. We note that because the Fermi

energy-dependence of the power factor comes exclusively from the function $A(r, E_f)$,

the Fermi energy that maximizes A is necessarily the same as the Fermi energy that

maximizes the power factor $E_{f,opt}$.

It will be shown below that except for a global energy shift the integrals and

therefore the function A do not depend on nanowire radius. This can be proven

analytically with a simple change of variables.

Take two nanowire radii r_a and r_b, where $\Delta E = E_{10,a} - E_{10,b}$ (the difference

between the single subband energies for nanowire a and nanowire b). The density-of-

states functions are shown as a function of energy in Figure 2.7(a) where we have

chosen r_a=10nm and r_b=15nm for demonstration purposes. In the proof given below,

we will prove the relation $A(r_a, E_f) = A(r_b, E_f + \Delta E)$: the A functions for nanowires a

and b are identical except for a shift of ΔE (see Figure 2.7(b)).

For nanowire a,

$$A(r_a, E_f) = \frac{\left[\int_{E_{10,a}}^{\infty} dE \cdot \sqrt{E - E_{10,a}} \cdot \left(\frac{e^{(E-E_f)/k_B T}}{\left(1 + e^{(E-E_f)/k_B T}\right)^2}\right) (E - E_f)\right]^2}{\int_{E_{10,a}}^{\infty} dE \cdot \sqrt{E - E_{10,a}} \cdot \left(\frac{e^{(E-E_f)/k_B T}}{\left(1 + e^{(E-E_f)/k_B T}\right)^2}\right)}. \tag{2.20}$$
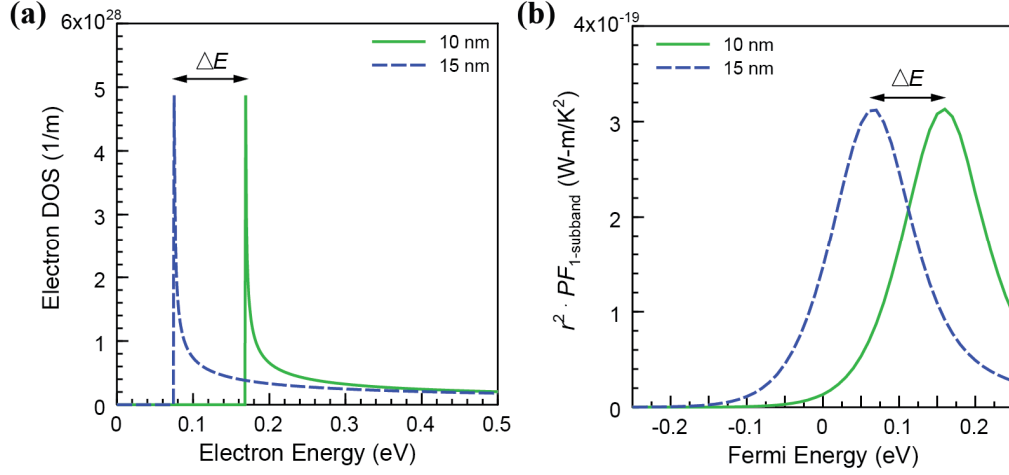
Figure 2.7: (a) Electron density-of-states as a function of carrier energy, (b) normalized $PF \cdot r^2$ calculations as a function of Fermi energy for nanowire radii of 10, 15nm.

We define a new energy variable $E' = E - \Delta E$. Then $E - E_{10,a} = E' + \Delta E - E_{10,a} = E' - E_{10,b}$ and we can write (2.20) as

$$A(r_a, E_f) = \frac{\left[\int_{E_{10,b}}^{\infty} dE' \cdot \sqrt{E' - E_{10,b}} \cdot \left(\frac{e^{(E'+\Delta E - E_f)/k_B T}}{\left(1 + e^{(E'+\Delta E - E_f)/k_B T}\right)^2} \right) (E' + \Delta E - E_f) \right]^2}{\int_{E_{10,b}}^{\infty} dE' \cdot \sqrt{E' - E_{10,b}} \cdot \left(\frac{e^{(E'+\Delta E - E_f)/k_B T}}{\left(1 + e^{(E'+\Delta E - E_f)/k_B T}\right)^2} \right)}. \tag{2.21}$$

If we similarly define a new Fermi energy $E'_f = E_f - \Delta E$, Eq. (2.21) can be written

$$A(r_a, E_f) = A(r_a, E'_f + \Delta E) = \frac{\left[\int_{E_{10,b}}^{\infty} dE' \cdot \sqrt{E' - E_{10,b}} \cdot \left(\frac{e^{(E'-E'_f)/k_B T}}{\left(1 + e^{(E'-E'_f)/k_B T}\right)^2} \right) (E' - E'_f) \right]^2}{\int_{E_{10,b}}^{\infty} dE' \cdot \sqrt{E' - E_{10,b}} \cdot \left(\frac{e^{(E'-E'_f)/k_B T}}{\left(1 + e^{(E'-E'_f)/k_B T}\right)^2} \right)},$$

$$\tag{2.22}$$

31

which is just $A\left(r_b, E'_f\right)$. We can then write

$$A\left(r_a, E_f\right) = A\left(r_b, E_f - \Delta E\right). \tag{2.23}$$

Therefore, the only difference between $A\left(r_a, E_f\right)$ and $A\left(r_b, E_f\right)$ is the global energy shift of ΔE. The significance of this result is best understood by noting that the energy shift ΔE is both the energy difference between the subband energies (see Figure 2.7(a)) *and* the energy difference between the Fermi energies that maximize A (see Figure 2.7(b)). Together, this means that the energy difference $E_{f,opt} - E_{10}$ and $A\left(E_{f,opt}\right)$ *do not depend on* r.

We have just shown that, evaluated at the optimal Fermi energy for each r, $A\left(r, E_f\right)$ does not depend on r. The single-subband power factor can then be written as:

$$PF\left(r, E_{f,opt}\right) = \left\{ 2\frac{\mu}{\pi^2 r^2 \hbar} \cdot \frac{\sqrt{2m^*_\parallel}}{eT^2} \right\} A\left(E_{f,opt}\right) \tag{2.24}$$

The r^{-2} dependence of the *PF* in the Hicks and Dresselhaus model therefore emerges solely from the energy-independent coefficient (in { }). Physically, the r^{-2} dependence of the power factor corresponds to the cross-sectional scaling of the conductivity of a quantum wire as the radius is varied, in the regime of a single operative conduction channel.

To determine the validity of the single-subband assumption, the electron density-of-states (DOS) function was calculated, per m^{-3}, for radii between 10 and 100nm using the parabolic band approximation
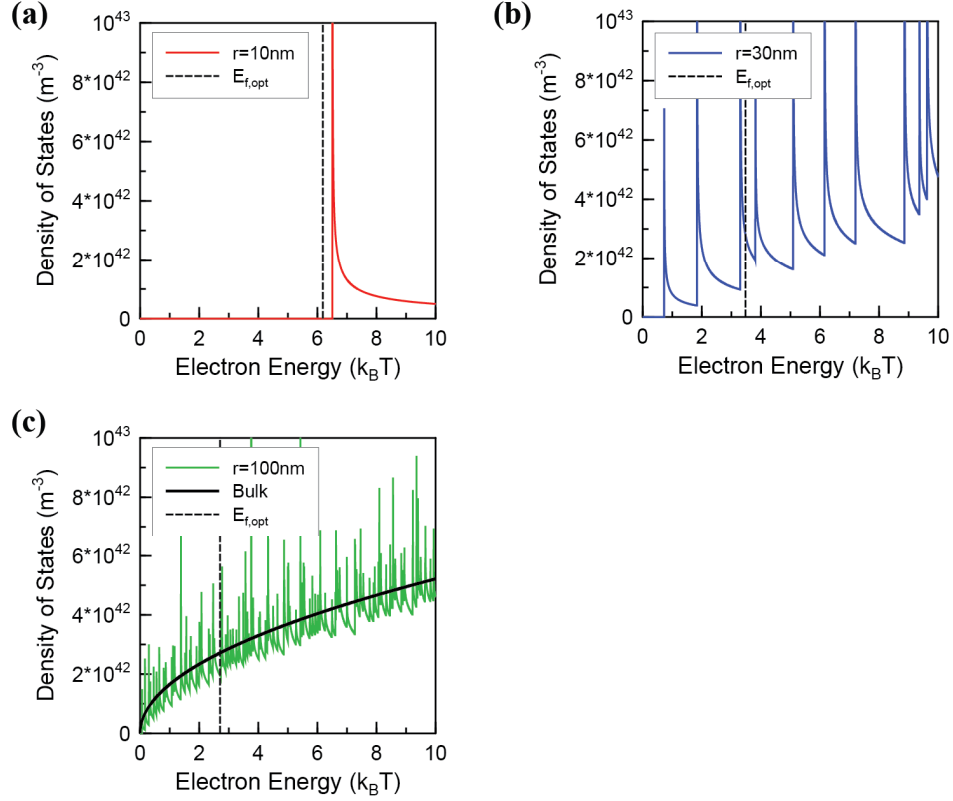
Figure 2.8: Calculated electron density-of-states as a function of electron energy for the conduction band of n-type InSb nanowires: (a) r=10nm, (b) r=30nm and (c) r=100nm (green) and bulk (black). Dashed vertical lines mark the Fermi energy that optimizes the power factor, $E_{f,opt}$, for each radius.

$$DOS_{1D}(E,r)dE = \frac{1}{\pi^2\hbar r^2}\sqrt{\frac{m_\perp^*}{2}}\sum_{nm}(E - E_{nm}(r))^{-1/2}dE \qquad (2.25)$$

where for each choice of r, the sum is taken over the E_{nm} subbands. Examples of DOS functions for radii of 10, 30 and 100nm are plotted in Figure 2.8 as a function of energy. The spikes in the DOS functions correspond to subband energies E_{nm}, and mark the bottom edges of the subband dispersion relations. The bulk density-of-states function, given by

$$DOS_{3D}(E)dE = \frac{\sqrt{2(m_\perp^*)^3}}{\pi^2\hbar^3}\sqrt{E}\,dE \qquad (2.26)$$

33

is also shown in Figure 2.8(c). For each DOS plot, the dashed vertical line marks the calculated optimal Fermi energy, $E_{f,opt}$ for the corresponding nanowire radius. The electrons that contribute to transport fall within several $k_B T$ of this Fermi energy. The relative positions of $E_{f,opt}$ and the spikes in DOS_{1D} in these plots illustrate that the single subband assumption is appropriate for r=10nm, but for radii as small as 30nm several subband energies fall within a few $k_B T$ window around $E_{f,opt}$. For r=100nm, the baseline of the density-of-states function resembles bulk and it is clear that many subbands contribute to transport. This indicates that the calculated power factor value for large nanowire radii should be close to that of bulk. The single-subband model ignores the contributions of these subbands that are crucial for accurately modeling transport in the intermediate size range (r>10nm). Therefore, the power factor values shown in Figure 2.6 are inaccurate for r>10nm and do not approach the bulk value.

2.7 *Many-Subband Model*

The "many-subband model" presented here retains the sum in Eq. (2.15) and assumes that the conduction band consists of 300 subbands. Power factor values calculated with the many-subband model are compared with the results of the single-subband model in Figure 2.9.[49] While the results of the many-subband model match those of the single-subband model in the small-radius limit, the curves diverge as r increases. The curve calculated using the many-subband model exhibits a minimum, located at r=19nm, at which the nanowire power factor falls 26% below the bulk value. Below 19nm, the assumption of a single subband is appropriate (confinement of electrons in the InSb nanowire is significant) and the power factor increases with decreasing radius.
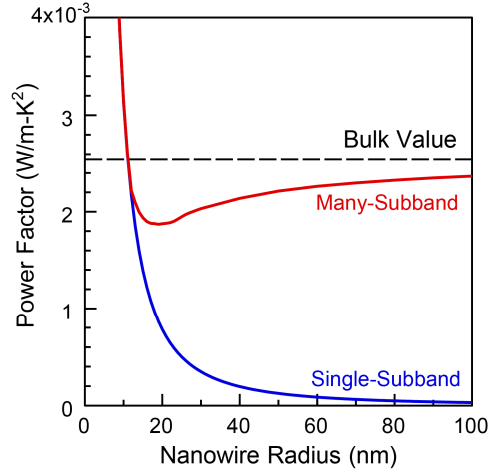
Figure 2.9: Power factor values calculated for InSb using the many-subband model (red) and the single-subband model (blue) as a function of nanowire radius.

Above 19nm, the power factor increases with *increasing* radius up to the bulk value, marked by a dashed horizontal line. The latter trend is clearly in contrast with what is seen using the single-subband model, which predicts that the nanowire power factor goes asymptotically to zero with increasing radius and vastly underestimates the power factor for large nanowire radii.

The evolution between the single-subband model and the many-subband model is shown in Figure 2.10(a), in which the calculated power factor is given as a function of radius and the number of subbands considered in calculations. The "number of subbands considered", or the number at which the sum in Eq. (2.15) is cut off, is a non-physical restraint on the model. As mentioned above, the electronic band structure of a nanowire includes an *infinite* number of subbands. For each choice of *r*, the smooth increase in the power factor with the number of subbands is shown in order to demonstrate model improvement and convergence of the power factor values.

35
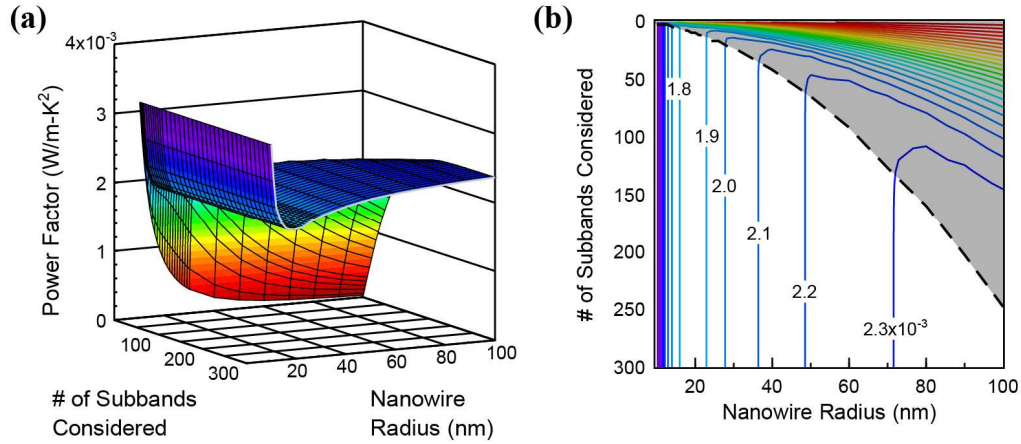
Figure 2.10: (a) Calculated power factor as a function of InSb nanowire radius and number of subbands included. (b) Contour plot of the data shown in (a). Calculations for which too few subbands are included (power factor values have not converged) have been grayed out.

The same data is given in the form of a contour plot in Figure 2.10(b). The number of subbands required for accurate calculation of the transport properties is marked by a dashed line in Figure 2.10(b). For each choice of r, this quantity is defined as the number of subbands N such that $(PF_N - PF_{N-1})/PF_N$ is less than the error tolerance of the calculation ($\sim 10^{-5}$). N ranges between 1 and 250 for the selected range of nanowire radii (10-100nm). Assuming that the conduction band consists of just 300 subbands is therefore appropriate for this range of radii. Data in the gray region, for which too few subbands have been included for convergence, is therefore not accurate or physical.

The non-monotonic dependence of the power factor on nanowire radius is attributed to the presence of two opposing effects: (1) *confinement*, which gives rise to the r^{-2} dependence for small nanowires, and (2) *the increasing magnitude of the density-of-states* with increasing nanowire radius (Figure 2.8). The minimum in *PF*

vs. *r* therefore represents the transition between regions of strong and weak quantum confinement.

2.8 Calculation of ZT

As discussed in Chapter 1, experimental work in the field of nanostructured thermoelectrics has demonstrated improvements in the thermoelectric figure of merit, *ZT*, when moving from bulk to nanostructures. In nearly all cases, the power factor of nanostructures is at or below the bulk value, and the increase in *ZT* is the result of a decrease in the lattice thermal conductivity. In this section, we investigate whether or not improvements in the *ZT* value of n-type InSb can be realized, in spite of the predicted decrease in the power factor values discussed in Sect. 2.7. In the absence of experimental data on the lattice thermal conductivity for InSb nanowires, *ZT(r)* values are calculated using two different approaches to modeling $\kappa_l(r)$. With the first approach, the lattice thermal conductivity does not change with confinement; with the second approach, the $\kappa_l(r)$ values are significantly lower (between 5 and 22x) than the bulk value.

The first approach, used by Hicks and Dresselhaus for calculations shown in Figure 1.5, is based on the kinetic theory of gases.[18, 19] The lattice thermal conductivity can be written as[39]

$$\kappa_l = {}^1\!/_3\, C_v v l_p \qquad\qquad (2.27)$$

where C_v is the specific heat per unit volume, *v* is the velocity of sound and l_p is the phonon mean free path. When the nanowire width (or film thickness) is smaller than the bulk phonon mean free path, we estimate that the phonon mean free path of the nanostructured system is given by $l_p{=}w$, where *w* is either the nanowire width or the

film thickness. The lattice thermal conductivity is then a piece-wise function of size, given by:

$$\kappa_l = \begin{cases} \frac{1}{3} C_v v w & \text{for } w < l_p \\ \frac{1}{3} C_v v l_p & \text{for } w > l_p \end{cases} \qquad (2.28)$$

For InSb, the room temperature bulk values for $\kappa_l=18$W/m-K, $C_v=1.15\text{x}10^6$ J/K-m^3 and $v=3410$m/s were obtained from the literature[50-52]. Using Eq. (2.27), the bulk phonon mean free path is calculated to be ~14nm and the piece-wise form of κ_l is given in Figure 2.11. Since l_p for bulk InSb is shorter than the smallest of the nanowire diameters investigated here (the minimum is w~$2r$=20nm), l_p is not modified in the nanostructures. All $ZT(r)$ calculations (shown in Figure 2.12) done in the range of r=10-100nm assume the bulk value of κ_l. Note that for each nanowire radius, the Fermi energy is now chosen such that ZT is maximized. As will be
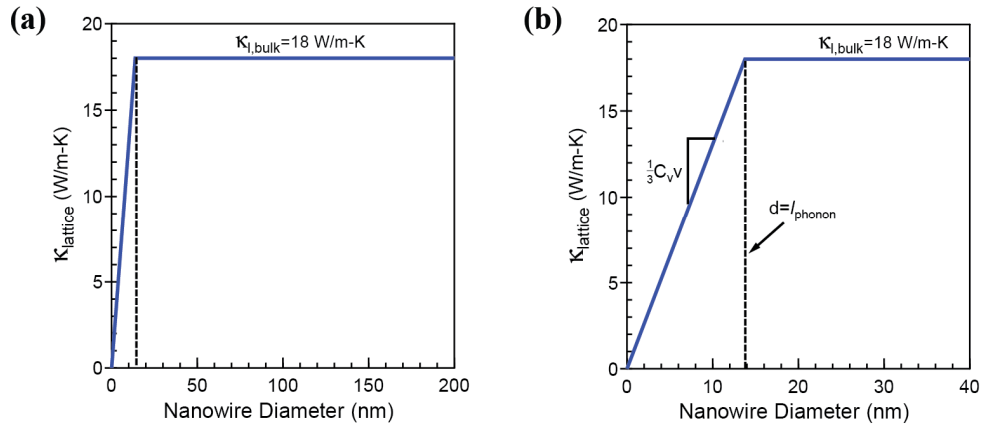
Figure 2.11: Calculated lattice thermal conductivity of InSb as a function of nanowire *diameter* using the kinetic theory of gases. Dashed vertical line marks the phonon mean free path in bulk. Plot in (b) focuses on the small-diameter region.
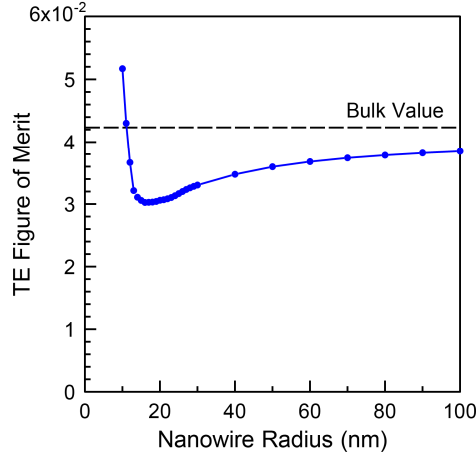
Figure 2.12: $ZT(r)$ calculations for InSb nanowires done assuming a bulk κ_l. The bulk ZT value is marked by a horizontal line.

explained in greater detail in Sect. 2.9, the Fermi energy for which ZT is maximized is not necessarily the same as the Fermi energy that maximizes the power factor ($E_{f,opt}$). With the assumption of a bulk κ_l, $ZT(r)$ exhibits a minimum at a radius of 16nm—slightly shifted relative to the radius corresponding to the minimum power factor at 19nm. The $ZT(r)$ and $PF(r)$ curves show similar qualitative behavior because with the assumption of the bulk lattice thermal conductivity, the total thermal conductivity (the denominator of ZT) is dominated by the radius-independent κ_l. For large nanowire radii, the ZT value approaches that of bulk (calculated to be ~0.042, marked by a horizontal line in Figure 2.12).

The second approach to modeling the lattice thermal conductivity of InSb nanowires follows the work of Broido and Mingo, described in detail in Ref. [53, 54]. The authors first derive the full phonon subband dispersion relations for cylindrical InSb nanowires assuming a Stillinger-Weber potential. The phonon mean free path is calculated for each subband i as a function of frequency ($l_i(\omega)$) including the effects

39

of impurity, Umklapp and diffuse boundary scattering. For each nanowire radius, the lattice thermal conductivity is then calculated as a function of temperature using

$$\kappa_l(T) = \frac{\hbar}{2\pi^2 r^2} \int_0^\infty [\sum_i l_i(\omega)] \cdot \omega \cdot \frac{df_B}{dT} d\omega \qquad (2.29)$$

where f_B is the Bose distribution and $l_i(\omega)$ is taken to have the piecewise form

$$l_i(\omega) = \begin{cases} l_i(\omega) & \text{for } \omega_{i,1} < \omega < \omega_{i,2} \\ 0 & \text{otherwise} \end{cases}. \qquad (2.30)$$

In Eq. (2.30), $\omega_{i,1}$ and $\omega_{i,2}$ are the lower and upper frequency limits for subband i. Like the expressions given in Sect. 2.2 for the electron transport properties, Eq. (2.28) was derived by solving the Boltzmann transport equation for phonons in an applied temperature gradient. Though this method for calculating $\kappa_l(r)$ has been verified experimentally for silicon nanowires, no experimental evidence for InSb has yet confirmed the validity of this assumed radius-dependence. $\kappa_l(r)$ was calculated for InSb by Mingo [4], and is shown in Figure 2.13(a). Over the range of radii investigated here, the room temperature κ_l values monotonically increase from 0.8 W/m-K to 3.9 W/m-K. This model clearly differs from the first approach taken above (Figure 2.11 and Figure 2.12) not only in the radius-dependence of the lattice thermal conductivity, but also in its magnitude. The κ_l values here, which fall significantly below the bulk value of 18W/m-K for all radii, are now within an order of magnitude of the electronic contribution to thermal conductivity (which ranges between ~0.1-0.3W/m-K for this range of radii). Using this model for κ_l, calculations of $ZT(r)$ result in a monotonic decreasing function of radius (Figure 2.13(b)). In the limit of large r, the calculated ZT value decreases down towards the bulk value, marked by a dashed horizontal line.
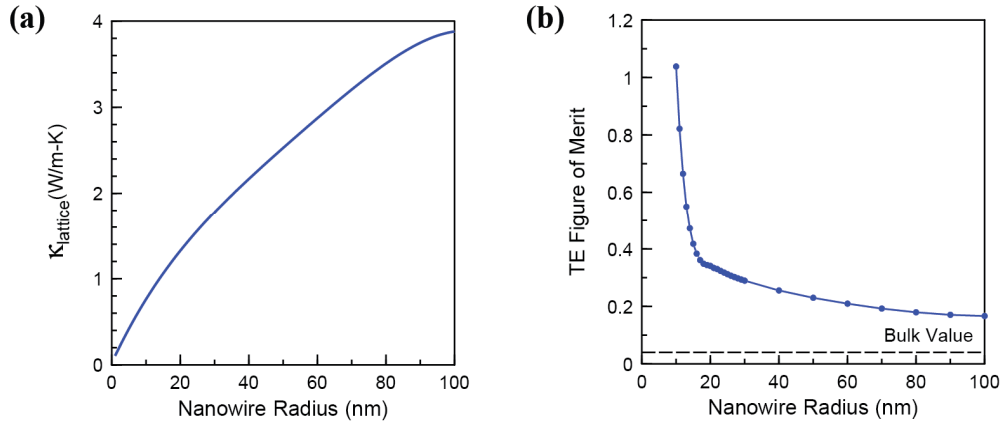
Figure 2.13: (a) Calculated lattice thermal conductivity values of InSb as a function of nanowire radius, from [4]. (b) $ZT(r)$ calculations for InSb nanowires assuming the $\kappa_l(r)$ values in (a).

2.9 Defining the Optimal Fermi Energy

As mentioned in previous sections, for each nanowire radius the Fermi energy is chosen such that either the power factor is maximized (see Sect. 2.5- 2.7) or *ZT* is maximized (see Sect. 2.8). These Fermi energies are not necessarily equal, and when maximizing *ZT*, the optimal Fermi energy will depend on the value of the lattice thermal conductivity. In this section, these optimal Fermi energies will be reported as a function of nanowire radius. For clarity, the Fermi energies which maximize the power factor and *ZT* will be denoted $E_{f,opt}^{PF}$ and $E_{f,opt}^{ZT}$, respectively.
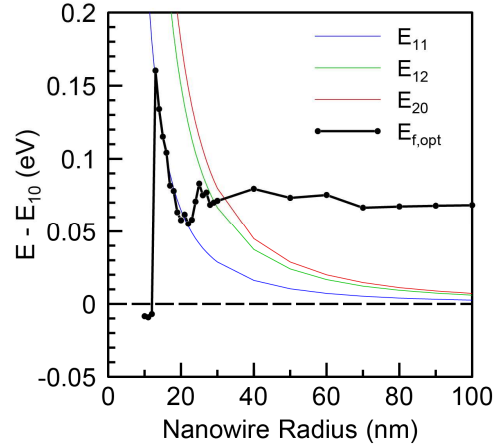
Figure 2.14: Fermi energy which maximizes the power factor ($E_{f,opt}^{PF}$) and the first 4 non-degenerate subband energies, relative to the first subband energy E_{10}, as a function of radius for InSb nanowires.

$E_{f,opt}^{PF}$ values are given relative to the first subband energy ($E_{f,opt}^{PF} - E_{10}$) as a function of radius in Figure 2.14. The first 4 non-degenerate subband energies are also shown (the first subband energy is given as a horizontal dashed line at 0). We can see from this plot that, while the power factor is a smooth function of nanowire radius, the optimal Fermi energy is not. For $r<12$nm, $E_{f,opt}^{PF} - E_{10}$ is approximately constant, at ~7meV below the band edge. As described in earlier sections, this is expected for highly confined systems in which a single subband contributes. For radii larger than 12nm, the jumps in $E_{f,opt}^{PF} - E_{10}$ mark the radii at which additional subbands begin to contribute to transport: At 13nm the second subband E_{11} starts to contribute, and at 25nm the third subband E_{12} starts to contribute. For larger radii, the jumps in $E_{f,opt}^{PF} - E_{10}$ are less significant (indicating decreasing quantum confinement), and the $E_{f,opt}^{PF} - E_{10}$ value eventually settles close to the value calculated for a bulk system, where $E_{f,opt}^{PF} - E_c = 70$meV.
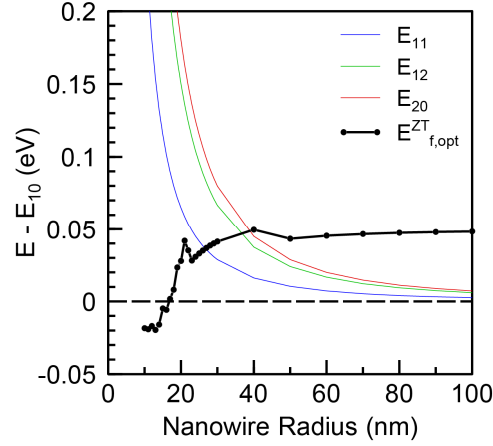
Figure 2.15: Fermi energy which maximizes ZT ($E_{f,opt}^{ZT}$) and the first 4 non-degenerate subband energies, relative to the first subband energy E_{10}, as a function of radius for InSb nanowires. Calculation of ZT was done using the $\kappa_l(r)$ data in Figure 2.13(a).

Analogous $E_{f,opt}^{ZT} - E_{10}$ values are given as a function of radius in Figure 2.15. As mentioned above, for a given radius the Fermi energy which maximizes ZT is dependent on the lattice thermal conductivity. The $E_{f,opt}^{ZT} - E_{10}$ values shown here were calculated using the radius-dependent lattice thermal conductivity given in Figure 2.13(a). The $E_{f,opt}^{ZT}$ values assuming a bulk lattice thermal conductivity (not shown) are nearly identical to the $E_{f,opt}^{PF}$ values.

The $E_{f,opt}^{ZT} - E_{10}$ values in Figure 2.15 and the $E_{f,opt}^{PF} - E_{10}$ values in Figure 2.14 show very different trends with nanowire radius. The $E_{f,opt}^{ZT} - E_{10}$ curve moves smoothly from a constant single-subband value (~20meV below the band edge) towards the bulk value of 70meV. In addition, the $E_{f,opt}^{ZT} - E_{10}$ values are consistently lower than the $E_{f,opt}^{PF} - E_{10}$ values. The $E_{f,opt}^{ZT} - E_{10}$ values move more smoothly with radius and fall below the $E_{f,opt}^{PF} - E_{10}$ values.

43

Figure 2.16 provides additional data to help explain the relationship between $E^{PF}_{f,opt}$ and $E^{ZT}_{f,opt}$. Calculated power factor (a), total thermal conductivity (b) and ZT values (c), normalized with respect to the maximum value for each quantity, are given in blue as a function of Fermi energy for an n-type InSb nanowire with radius 13nm. This radius is chosen because, as described above, at r=13nm the second subband starts to contribute to transport and $E^{PF}_{f,opt} - E_{10}$ "jumps" into the band (Figure 2.14).

The optimal Fermi energies $E^{PF}_{f,opt} - E_{10}$ and $E^{ZT}_{f,opt} - E_{10}$ are marked in (a)
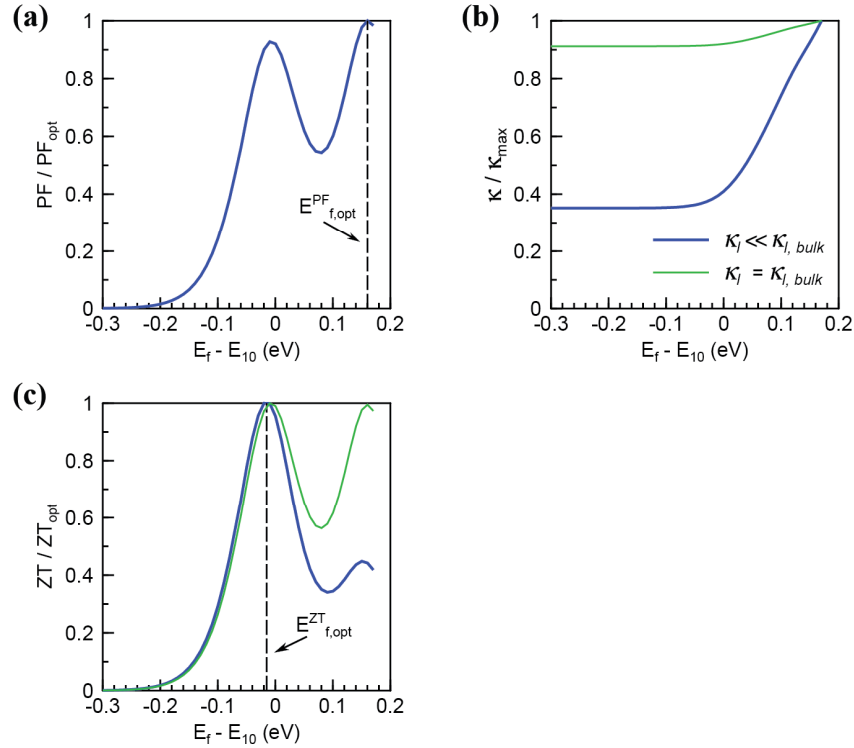
Figure 2.16: (a) Power factor values, (b) total thermal conductivity values and (c) ZT values, normalized with respect to the optimal value, as a function of $E_f - E_{10}$ for an InSb nanowire with radius 13nm. The optimal Fermi energies $E^{PF}_{f,opt} - E_{10}$ and $E^{ZT}_{f,opt} - E_{10}$ are marked as vertical dashed lines in (a) and (c), respectively.

and (c), respectively. As can be seen in Figure 2.16(a), the second peak in the power factor is higher than the first peak. However, after dividing by the monotonically increasing thermal conductivity (Figure 2.16(b)), the second peak in *ZT* is *lower* than the first peak (Figure 2.16 (c)). The $E_{f,opt}^{ZT}$ values therefore tend to fall closer to the band edge: for a given radius $E_{f,opt}^{ZT}$ is lower than $E_{f,opt}^{PF}$. In addition, this means that the $E_{f,opt}^{ZT}$ values do not "jump" with radius as additional subbands contribute to transport. Note that by fixing the lattice thermal conductivity to the bulk value, the total thermal conductivity becomes a much weaker function of Fermi energy (green data in Figure 2.16(b)). As such, *ZT* (green data in Figure 2.16(c)) shows a Fermi energy dependence similar to the power factor.

2.10 Summary

In this chapter, two models for calculation of the thermoelectric transport properties of cylindrical nanowires of a one-band conductor were presented: (1) The original "single-subband model" developed by Hicks and Dresselhaus and (2) the "many-subband model" derived here, which takes into account the additive contribution of multiple subbands to the transport properties. Both models were applied to n-type InSb, a promising thermoelectric material with a simple electronic band structure.

Power factor values calculated using the single-subband model decrease monotonically with nanowire radius as r^{-2}. These results lead us to the conclusion that has prevailed in the field of nanostructured thermoelectrics for the past 20 years: Smaller is always better!

Using the many-subband developed here, we reach a new conclusion which is in line with what has been seen experimentally. We find that the thermoelectric power factor of nanowires actually falls below the bulk value for all nanowires larger than 12nm in radius. The $PF(r)$ curve exhibits a minimum at 19nm (falling 26% below the bulk value), which separates regions of weak and strong quantum confinement. The simplicity of the n-type InSb band structure and the approximations made to keep the model as general as possible mean that the qualitative trends found here are expected to apply to a wide range of materials.

$ZT(r)$ calculations were also presented with two different approaches to modeling the lattice thermal conductivity. With the assumption of a radius-dependent $\kappa_l(r)$, we recover a monotonically decreasing function $ZT(r)$, and report a significant enhancement in the nanowire ZT values over bulk despite the predicted decreases in power factor values. As has been indicated by most experimental work in the field, the potential for high ZT values in nanostructured materials may therefore lie in decreasing the lattice contribution to thermal conductivity.

Chapter 3 Parametric Investigation of the Thermoelectric Transport Properties of Nanowires and Thin Films

3.1 Introduction

In Chapter 2, a model was presented for calculation of the thermoelectric transport properties of cylindrical nanowires of a one-band conductor. Applied to n-type InSb, the results calculated using this model indicate that in contrast to original predictions[18, 19], the nanowire power factor falls below the bulk value for a wide range of nanowire radii (r=12-100nm). This phenomenon is not expected to be specific to n-type InSb; indeed, the vast majority of experimental work on nanostructured thermoelectric materials thus far indicates that the power factor of nanostructures falls at or below the bulk value for a wide variety of materials and fabrication techniques.

In order to make general conclusions about the size-dependence of the power factor of nanostructures beyond n-type InSb cylindrical nanowire systems, a quantitative analysis of the effects of various material and system parameters on the power factor is necessary. In this chapter, we investigate how the size-dependence of the power factor is affected by the following parameters: nanowire shape, system dimension, material parameters and temperature.

1. Nanowire shape: A model is presented for calculating the subband structure and transport properties of nanowires with a square cross-section. Power

factor values calculated using this model, assuming the band parameters of n-type InSb, are compared with those calculated for cylindrical nanowires as a function of cross-sectional area.

2. System dimension: We report a model for calculating the subband structure and transport properties of thin film systems. Power factor calculations for n-type InSb thin films are presented as a function of film thickness.

3. Material parameters: Size-dependent power factor curves are presented for a range of material band parameters (carrier mobility and effective mass values) for nanowire and thin film systems.

4. Temperature: Size-dependent power factor curves are reported for n-type InSb nanowire and thin film systems at different temperatures.

3.2 Modeling Thermoelectric Transport Properties of Square Nanowires

The model used for calculating the thermoelectric transport properties of square nanowires differs from the one developed in Chapter 2 for cylindrical nanowires through (1) a modification of the coefficient of the "L-integrals" and (2) a change in the form of the electronic subband structure. Except for these two changes, the assumptions made in the model outlined below and the procedure for calculating the transport properties are identical to those described in Chapter 2.

The 1D form of Eq. (2.5) for a square nanowire with width *l*, can be written as:

$$\mathbf{L}^{(\alpha)} = \sum_{nm} 2 \frac{e^2}{\pi l^2 \hbar} \sqrt{\frac{2}{m_\parallel^*}} \int_{E_{nm}}^{\infty} dE \cdot \tau(E) \sqrt{E - E_{nm}} \cdot \left(-\frac{\partial f}{\partial E}\right) \cdot \left(E - E_f\right)^{\alpha}. \qquad (3.1)$$

where $m_\parallel^*$ is the effective mass in the direction of transport and the sum is taken over the subband energies E_{nm}.

For nanowires with a square cross-section, the subband energies in the expression for the 1D dispersion relation $(E(\mathbf{k}) = E_{nm}(k_x) = \frac{\hbar^2 k_x^2}{2m_\parallel^*} + E_{nm})$ are found by solving a "particle in a box" problem for electrons confined in two dimensions (Eq. (2.12)). We have assumed that the potential has the form

$$V(y,z) = \begin{cases} \infty & y = l \text{ or } z = l \\ 0 & y < l \text{ and } z < l \end{cases}. \tag{3.2}$$

The eigen-energies are then given by

$$E_{nm} = E_{nm}(k_x) - \frac{\hbar^2 k_x^2}{2m_\parallel^*} = \frac{\hbar^2 \pi^2 (n^2 + m^2)}{2m_\perp^* l^2}, \tag{3.3}$$

where n and m are quantum numbers and $m_\perp^*$ is the effective mass in the directions of confinement. The subband energy E_{nm} marks the bottom edge (for k_x=0) of the dispersion relation for subband nm (see schematic in Figure 2.3).Calculations presented in this section were done with the constant relaxation time approximation $(\tau(E) = \tau = \mu m_\parallel^*/e)$ and the same material parameters assumed in Chapter 2 (those of n-type InSb).

The first 10 subband energies (including degenerate energies) calculated for n-type InSb cylindrical and square nanowires of identical cross-sectional areas ($l^2 = \pi r^2 = 100\pi$ nm^2) are compared in Table II.

Table II. The first 10 subband energies calculated for cylindrical and square nanowires of n-type InSb with cross-sectional area 100π nm^2. Shading indicates pairs of degenerate energies.

E_{nm}, Cylindrical Nanowires (eV)	E_{nm}, Square Nanowires (eV)
0.168	0.183
0.428	0.458
0.428	0.458
0.768	0.732
0.768	0.915
0.887	0.915
1.186	1.189
1.186	1.189
1.433	1.555
1.433	1.555

The subband energies calculated for the square nanowire are generally higher than those of the cylindrical nanowire, indicating stronger confinement. In addition, we see a change in the ordering of the degenerate pairs of subbands (see the 4-6th subbands for both geometries). Calculations done for nanowires of the two geometries can therefore be best understood as calculations done for 1D systems with somewhat different electronic subband structures.

Transport property calculations were done for n-type InSb nanowires with a square cross-section as a function of Fermi energy for a range of wire widths (l=10-190nm) using Eq. (3.1) and (2.6). These calculations were done using the "many-subband model" assuming that the conduction band consists of 300 subbands. The

procedure used, as well as a more detailed explanation of the many-subband model, is given in Chapter 2.

In order to investigate the effect of nanowire geometry, we compare the power factor values calculated for square and cylindrical nanowires. The calculated power factor values for these two geometries, normalized with respect to the bulk value, are given as a function of nanowire cross-sectional area in Figure 3.1(a). For each choice of l and r, the power factor is optimized with respect to Fermi energy ($E_f=E_{f,opt}$, see Sect. 2.9 for additional information). As was done for circular nanowires (see Sect.2.7), we verified that the number of subbands required for convergence of the power factor values is less than 300 for the range of nanowire widths investigated here (Figure 3.1(b)). We note that 300 subbands is enough to accurately calculate the
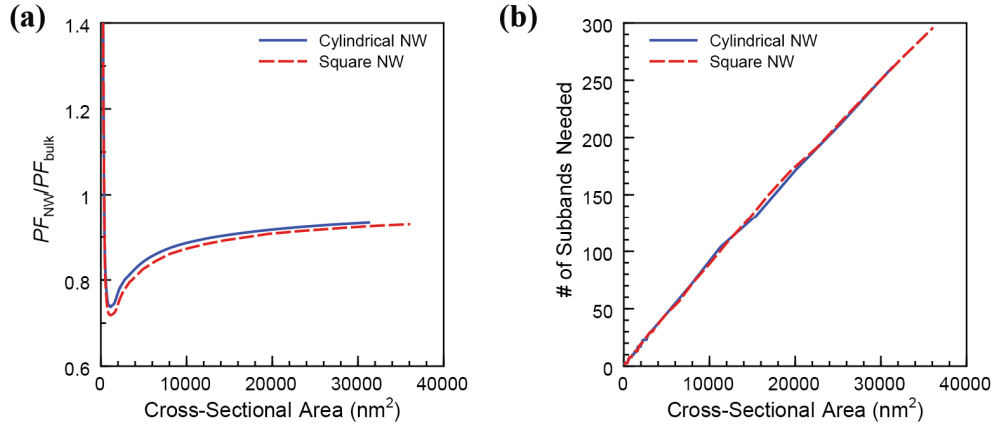
Figure 3.1: (a) Calculated power factor values, normalized with respect to bulk, as a function of nanowire cross-sectional area for cylindrical and square nanowire geometries. Band parameters for InSb were assumed. (b) Number of subbands required for convergence of the calculated power factor values as a function of nanowire width.

transport properties of cylindrical nanowires up to 100nm in radius, and square nanowires up to 190nm in width.

The power factor curves are similar, exhibiting minima near cross-sectional areas of ~1100 nm^2. For areas smaller than 1100 nm^2, a single subband contributes to transport and, despite the fact that the single subband energies differ for the two geometries, the *PF* values are identical (see Sect. 2.6). For larger systems in which additional subbands contribute, the difference in the subband structure for the two geometries becomes important and the *PF* values of cylindrical nanowires differ from those of square nanowires. For a given cross-sectional area, the power factor values calculated for square nanowires fall below those calculated for cylindrical nanowires. This includes the minimum power factor value, which falls 28% below the bulk value (compare with 26% for cylindrical nanowires). The differences between the two curves are the result of the slightly larger separations between the subband energies (see Table II) for the square geometry. Because of this somewhat stronger confinement, a larger nanowire size is required to recover bulk transport properties. These results indicate that, regardless of the nanowire cross-sectional shape, the power factor shows qualitatively the same dependence on nanowire size. However, the slight change in the electronic subband structure when moving from cylindrical nanowires to stronger confined square nanowires leads to lower power factor values.

3.3 Modeling Thermoelectric Transport Properties of Thin Films

In this section, a model is presented for calculating the thermoelectric transport properties of thin films. The model presented here is based on the same general framework (relaxation time approximation, effective mass approximation)

described in Sect. 2.2-2.3. The derivation given below is brief; a detailed discussion can be found in [43].

For two-dimensional thin films, we take the z-axis to be perpendicular to the film and the electric field and temperature gradient along the x-direction. For this system, confining potential is given by

$$V(z) = \begin{cases} \infty & z = a \\ 0 & z < a \end{cases} \qquad (3.4)$$

and the imposed boundary condition is a vanishing wave function $\psi(\mathbf{r})$ at the thin film surfaces. The one-dimensional Schrodinger equation is then given by

$$-\frac{\hbar^2}{2m_\perp^*}\frac{\partial^2 Z}{\partial z^2} = \left[E - \frac{\hbar^2 k_x^2}{2m_\parallel^*} - \frac{\hbar^2 k_y^2}{2m_\perp^*}\right] \cdot Z(z) \qquad (3.5)$$

The eigen-energy solutions of Eq. (3.5) are of the form

$$E_n = E - \frac{\hbar^2}{2}\left(\frac{k_x^2}{m_\parallel^*} + \frac{k_y^2}{m_\perp^*}\right) = \frac{\hbar^2 \pi^2 n^2}{2m_\perp^* a^2} \qquad (3.6)$$

where a is the film thickness and n is the quantum number. The subband energy E_n is the quantized energy level resulting from confinement in the z-direction, and marks the bottom edge ($k_x=k_y=0$) of the subband dispersion relation.

The thermoelectric transport properties are calculated by solving the following two-dimensional form of Eq. (2.5):

$$\mathbf{L}^{(\alpha)} = \sum_n \frac{e^2}{\pi\hbar^2 a}\sqrt{\frac{m_\perp^*}{m_\parallel^*}}\int_{E_n}^{\infty} dE \cdot \tau(E)(E - E_n) \cdot \left(-\frac{\partial f}{\partial E}\right) \cdot \left(E - E_f\right)^{\alpha} \qquad (3.7)$$

where the sum is taken over all subbands. Differences between the 1D (Eq. (2.15) and (3.1)) and 2D (Eq. (3.7)) forms of the "L-integrals", which arise from differences in the electron density-of-states (see schematics in Figure 1.4), can be seen both in the coefficient and in the energy-dependent integrand.
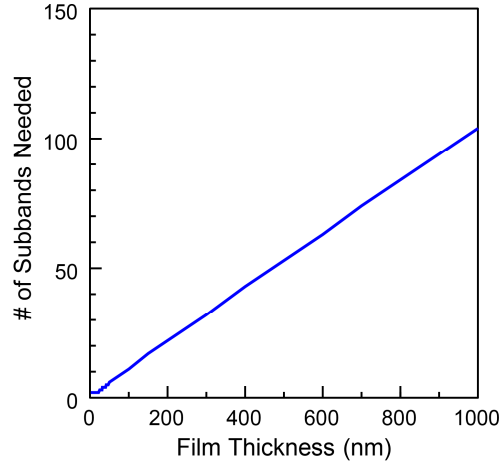
Figure 3.2: Number of subbands required for convergence of the calculated power factor values as a function of film thickness.

Transport property calculations were done assuming the band parameters of n-type InSb for thin films with thicknesses a=1-1000nm using the "many-subband model" described in Chapter 2. The procedure for these calculations is analogous to what is described in Sect. 2.5 for cylindrical nanowires. The number of subbands required for convergence of the power factor (see Sect.2.7), plotted in Figure 3.2, is less than 300 for the range of thicknesses investigated here.

Power factor values, optimized with respect to Fermi energy, are given as a function of film thickness in Figure 3.3. The optimized bulk power factor value is marked by a horizontal dashed line. The non-monotonic relationship between *PF* and a is similar to what was seen for nanowire systems. The minimum *PF* value, which falls 22% below the bulk, is seen for a film thickness of 27 nm, confirming that smaller system sizes are required for strong confinement in 2D films as compared with 1D nanowires (for which the minimum is located at $2r$=38 nm or l=34 nm).

54
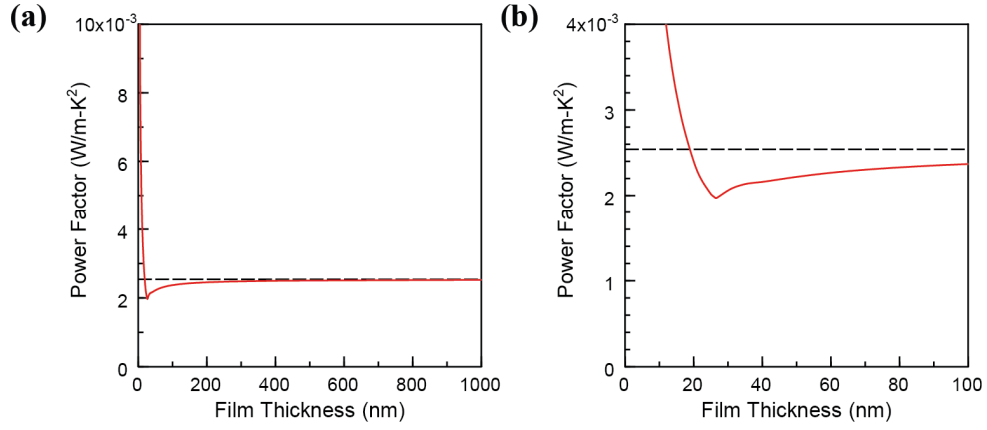
Figure 3.3: Calculated power factor values as a function of thin film thickness, assuming band parameters for n-type InSb. (b) shows the same data as in (a), focusing on the minimum in the *PF(a)* curve. The bulk value is marked by a horizontal dashed line.

The non-monotonic dependence of the power factor on thin film thickness, like what was seen for nanowire systems, indicates the presence of two competing effects: confinement and increasing magnitude of the density of states. For small sizes, confinement is strong and the power factor increases monotonically with *decreasing size*. In this range of thicknesses, a single subband contributes to transport and, by an argument analogous to the one described in Sect. 2.6, it can be shown that the optimized power factor has a a^{-1} dependence originating from the coefficient of Eq. (3.7). Confinement is weaker in the thin films than in the nanowire systems; as a result, the minimum 2D power factor value does not fall as far below bulk as the minimum in the 1D power factor.

3.4 Effect of Changing Band Parameters on the Size-Dependence of the Thermoelectric Power Factor

3.4.1 Introduction

In this section, we investigate the effect of *material* on the size-dependence of the thermoelectric power factor. The calculated results are influenced by the choice of material through the material-specific values of $\mu, m_{\parallel}^*, m_{\perp}^*$ and τ (not all independent). The calculations presented here are limited to materials with a single spherical Fermi pocket $(m^* = m_{\parallel}^* = m_{\perp}^*)$ in which the relaxation time does not depend on carrier energy, and to room temperature. The values for the effective mass, carrier mobility and relaxation times are in the range $m^* = 0.01\text{-}0.06 m_0$, $\mu = 1 \times 10^5 - 7 \times 10^5 \frac{cm^2}{V-s}$ and $\tau = 5 \times 10^{-13} - 2 \times 10^{-12}$s. These values are typical of single crystal thermoelectric materials.

We note that the characteristics of the majority carriers are only several of the material-specific parameters that influence the thermoelectric properties of real materials. The reader is referred to several excellent theoretical publications in which the thermoelectric transport properties of a single material are calculated, taking into account many additional material-specific properties. [35, 55, 56]

3.4.2 Results and Discussion

We first discuss the power factor of bulk systems. At a given temperature T, the bulk power factor can be written as a function of the carrier parameters and the Fermi energy as

$$PF(E_f) = \left\{ \frac{\mu(m^*)^{3/2}}{3\pi^2\hbar^3} \frac{\sqrt{8}}{eT^2} \right\} \left[\frac{\left[\int_0^\infty dE \cdot \sqrt{E^3} \cdot \left(-\frac{\partial f}{\partial E} \right) \cdot (E - E_f) \right]^2}{\int_0^\infty dE \cdot \sqrt{E^3} \cdot \left(-\frac{\partial f}{\partial E} \right)} \right] \tag{3.8}$$

by plugging Eq. (2.16) into Eq. (2.17). The effective mass and mobility dependence comes solely from the energy-independent coefficient (surrounded by { }). For each choice of Fermi energy E_f^* , we can then write that $PF(E_f^*) \propto \mu(m^*)^{3/2}$. Since the optimal Fermi energy $E_{f,opt}$ depends only on the ratio of integrals and is constant with respect to μ, m^* and τ, we can then write that $PF(E_{f,opt}) \propto \mu(m^*)^{3/2}$. Optimized bulk power factor values $PF(E_{f,opt})$ are given as a function of effective mass m^* in Figure 3.4. When the mobility is held constant and the effective mass is varied, $PF(E_{f,opt}) \propto (m^*)^{3/2}$ (solid black line). If the scattering time τ is kept constant while the effective mass is varied, $PF(E_{f,opt}) \propto e\tau \cdot (m^*)^{-1}(m^*)^{3/2} \propto (m^*)^{1/2}$ (dashed black line). The benefits of high effective mass and mobility values for thermoelectric
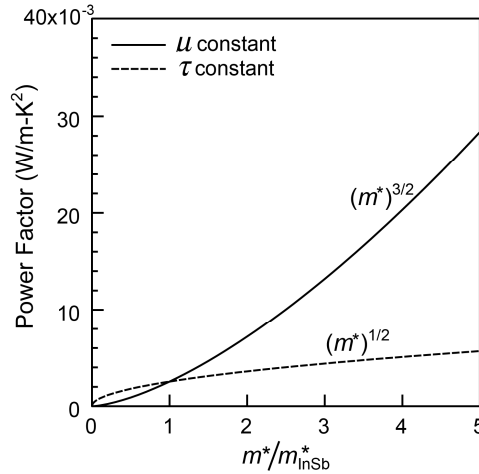
Figure 3.4: Optimal bulk power factor values as a function of effective mass when the mobility is held constant (solid line) and the relaxation time is held constant (dashed line).

transport are well-known—in the absence of additional experimental information (e.g. the magnitude of the Seebeck coefficient), the quantity $\mu(m^*)^{3/2}/\kappa_l$ is often used as a "figure of merit" for thermoelectric materials.[23]

Next, we present power factor calculations for nanowire systems. In this section, we focus on nanowires with a circular cross-section; for a similar discussion on the power factor of square nanowires, see [57]. Power factor values calculated for cylindrical nanowires are given as a function of nanowire radius r in Figure 3.5. The optimal power factor values for nanowires with various values of the electron effective mass but the same mobility are compared as a function of r in Figure 3.5(a). Figure 3.5(b) compares the nanowire PF calculated assuming various effective mass values, keeping the electron relaxation time constant. For each set of parameters, the power factor curve is cut off when 300 subbands are not enough to accurately model
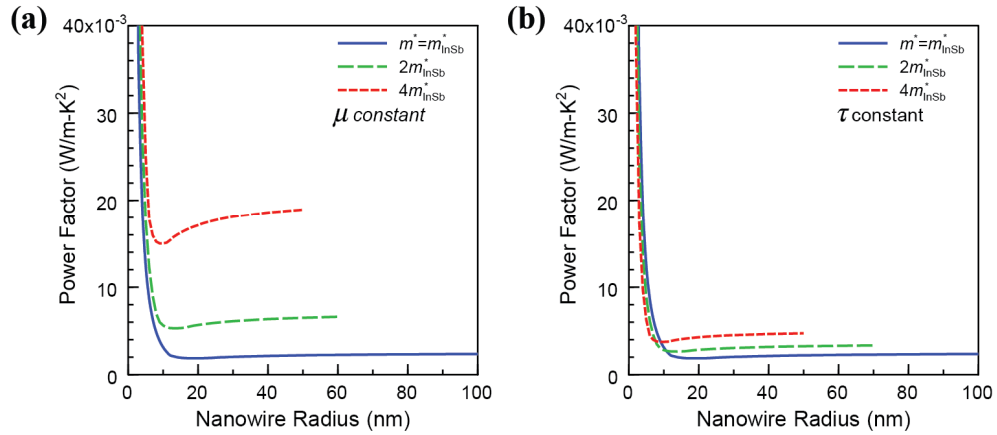
Figure 3.5: Calculated power factor values for cylindrical nanowires assuming different band parameters. (a) The effective mass value is varied while the mobility is held constant. (b) The effective mass value is varied while the relaxation time is held constant. The solid blue curves were calculated assuming the band parameters of n-type InSb.

transport in the system. This cut-off size is different for each set of band parameters. The power factor exhibits a non-monotonic dependence on nanowire size for each choice of material parameters. The details of each curve (e.g.: the magnitude of the power factor values, the size corresponding to the minimum power factor value), however, clearly depend on the values of μ, m^* and τ. The effect of electron mobility can be seen in Eq. (2.18): For each Fermi energy, the power factor increases linearly with μ. Changing the effective mass has two effects on the power factor curves. First, for each r an increase in m^* generally leads to an increase in the power factor value (e.g. compare the red dashed and blue curves in Figure 3.5 (a)). This is due to the $(m^*)^{1/2}$ factor in the energy-independent coefficient of the power factor (see Eq. (2.18)), and is clearly more significant when the mobility is held constant. Second, as the effective mass increases, the minimum in the power factor curve becomes narrower and shifts to smaller sizes. This trend is the result of weakening confinement. For a given nanowire radius, the subband energies E_{nm} are proportional to $(m^*)^{-1}$. With an increase in m^*, the subband energies decrease in magnitude and become closer together. This is an effect analogous to (and more pronounced than) what was seen when comparing the power factor values of nanowires of square and circular cross-section (see Figure 3.1(a)): The minimum in the power factor is narrower and occurs at lower sizes in cylindrical relative to square nanowires (due to higher values of E_{nm}).

Analogous transport property calculations were done for two-dimensional thin films as a function of film thickness a. The optimized power factor is shown as a function of a for model systems with various electron effective mass values and the
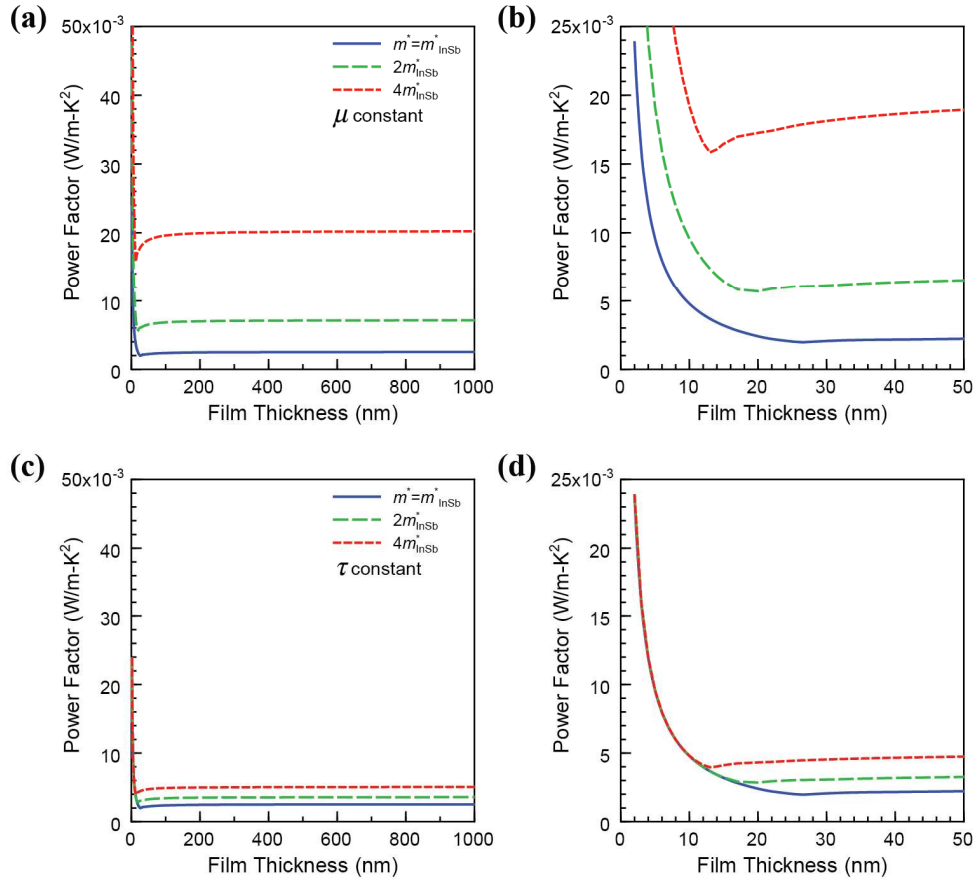
Figure 3.6: Calculated power factor values for thin films assuming different band parameters. (a) The effective mass value is varied while the mobility is held constant (plot focusing on the minima given in (b)). (c) The effective mass value is varied while the relaxation time is held constant (plot focusing on the minima given in (d)). The solid blue curves were calculated assuming the band parameters of n-type InSb.

same mobility, in Figure 3.6(a) and (b), and for systems with various effective masses and the same relaxation time in Figure 3.6(c) and (d). The non-monotonic relationship between *PF* and *a* persists in all the systems studied. For the nanostructures discussed here, we have identified several common trends in the relationship between optimal power factor and system size, and how this relationship is affected by changes to the single-carrier parameters. (1) For all of the nanostructures (cylindrical and square nanowires, thin films), increasing the electron effective mass results in a narrower

minimum, shifted to a smaller system size (indicative of weakening confinement). (2) For all structures and system sizes, the power factor increases monotonically with electron mobility. (3) For all materials and systems investigated, the dependence of the optimized power factor on system size can be split into two size-ranges separated by a minimum. For small systems, confinement is strong and the *PF* increases with decreasing size. For large systems, confinement is weak and the *PF* increases with increasing size up to the bulk value. The minimum in the power factor is predicted to be between 72 and 78% of the bulk value.

The calculations presented in Sect. 3.4 indicate that the trends shown in Sect. 2.6 and 3.1-3.3 are not exclusive to n-type InSb: The non-monotonic size-dependence of the power factor is predicted for isotropic, one-band conductors assuming a range of carrier parameters. It is important to note, however, that the exact sizes corresponding to the minimum power factor as well as the size reduction required for improvement in the power factor over bulk depend on the specific materials parameters used. In the absence of analytical relationships between thermoelectric power factor, system size and materials parameters, in-depth modeling of each individual material is required in order to extract this practical information.

3.5 Effect of Temperature

3.5.1 Introduction

In this section, we focus on how the size-dependence of the power factor is affected by changes in the system temperature. The material parameters of n-type InSb are assumed for this investigation, but (as was shown in Sect. 3.3 for room temperature) the qualitative results given below are expected for any choice of m^*, μ and τ.

61

The transport properties of n-type InSb nanowires and thin films were calculated at various temperatures between 10 and 600K. For the investigation here, the temperature-dependence of electron transport is assumed to come exclusively from [the broadening of] the Fermi-Dirac distribution. Other effects that are material-specific (temperature-dependence of the effective masses or bandgap, changes in dominant scattering mechanism, etc.) are not addressed here.

3.5.2 Temperature Dependence of the Bulk Power Factor

Bulk power factors calculated for various temperatures between 10 and 600K are shown in Figure 3.7(a) and (b) as a function of Fermi energy. At a fixed Fermi energy, the bulk power factor increases with increasing temperature. As T increases, the Fermi energy corresponding to the maximum in the power factor ($E_{f,opt}$) shifts further into the band. The temperature dependence of the bulk $PF(E_{f,opt})$ is given in Figure 3.7(c). As noted in the plot and explained in detail below, the optimized bulk power factor value scales as $T^{3/2}$. The $T^{3/2}$ dependence of the bulk power factor can be explained by showing that the temperature-dependence of the bulk power factor comes exclusively from the energy-independent coefficient of the "L-integrals", and that while $E_{f,opt}$ increases with temperature, the normalized optimal Fermi energy $E_{f,opt}/k_B T$ is constant with respect to temperature.

Starting with Eq. (3.8) and defining normalized variables $x \equiv E/k_B T$ and $x_f \equiv E_f/k_B T$, the bulk power factor at temperature T can be re-written as

$$PF(x_f, T) = \left\{ \frac{\mu m_{\perp}^*}{3\pi^2 \hbar^3} \frac{(k_B)^2 \sqrt{8m_{\parallel}^*}}{e} (k_B T)^{3/2} \right\} \cdot B(x_f) \qquad (3.9)$$

where $B(x_f)$ is the ratio of integrals given by
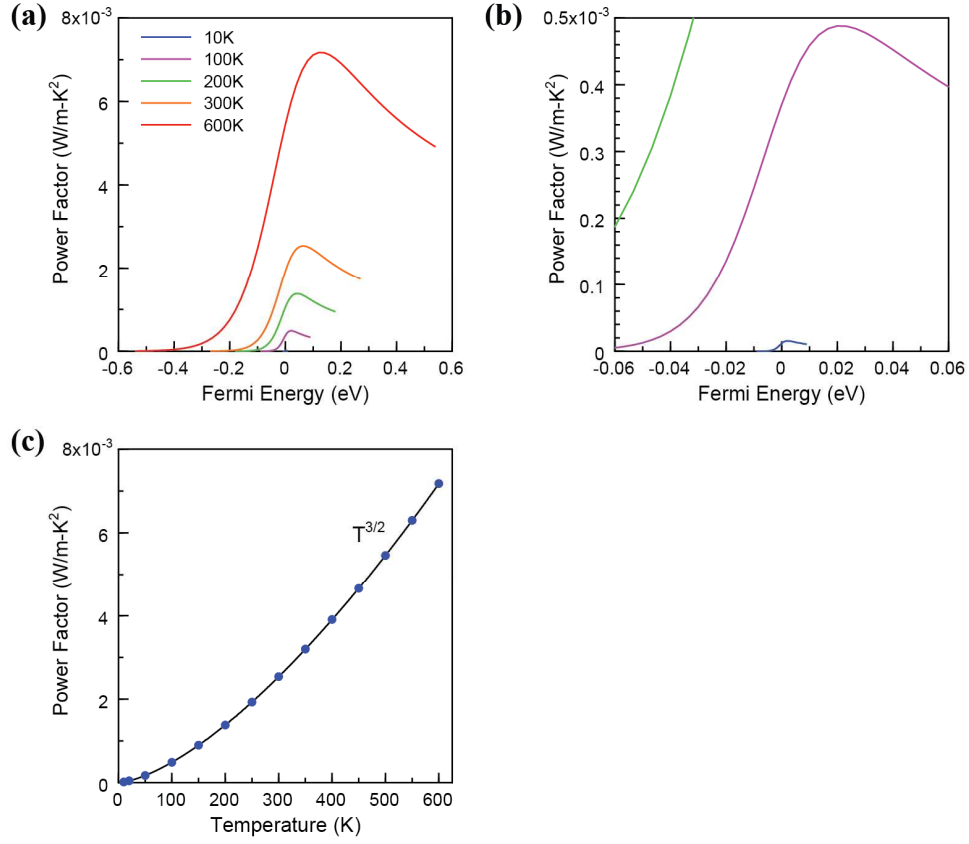
Figure 3.7: (a) Bulk power factor values as a function of Fermi energy for InSb at different temperatures between 10 and 600K. (b) Same data as shown in (a), with a focus on low-temperature curves. (c) Optimized bulk power factor values as a function of temperature. Solid line traces the function $T^{3/2}$.

$$B(x_f) = \frac{\left[\int_0^\infty dx \cdot \sqrt{x^3} \cdot \left(-\frac{\partial f}{\partial x}\right) \cdot (x - x_f)\right]^2}{\int_0^\infty dx \cdot \sqrt{x^3} \cdot \left(-\frac{\partial f}{\partial x}\right)}. \tag{3.10}$$

The x_f-dependence of the power factor then comes solely from B, so the x_f that maximizes the power factor ($x_{f,opt}$) also maximizes B. Further, Eq. (3.10) indicates that $x_{f,opt}$ and $B(x_{f,opt})$ are constant with respect to temperature. This means that the Fermi energy corresponding to the maximum power factor scales with T (i.e. $E_{f,opt}/k_B T$ is constant) and (2) the temperature-dependence of the optimal power

factor $(PF(E_{f,opt}/k_BT))$ comes solely from the energy-independent coefficient (surrounded by {} in Eq. 3.9), which is proportional to $T^{3/2}$.

3.5.3 Temperature-Dependence of the Power Factor of Cylindrical Nanowires

Radius-dependent power factor values calculated for cylindrical nanowires and thickness-dependent power factor values calculated for thin films at various temperatures are shown in Figure 3.8(a) and (b), respectively. All power factor values have been optimized with respect to Fermi energy. Similar to what was seen in the optimized bulk values (Figure 3.7(c)), for each nanowire radius r and film thickness a an increase in temperature leads to an increase in the power factor. In addition, as the temperature increases the minimum in the power factor curve narrows and shifts lower in size. This result is similar to what was seen with an increase in effective mass; however, an increase in temperature does not lead to weakening confinement (the subband energies do not change with T). As will be shown below, increasing
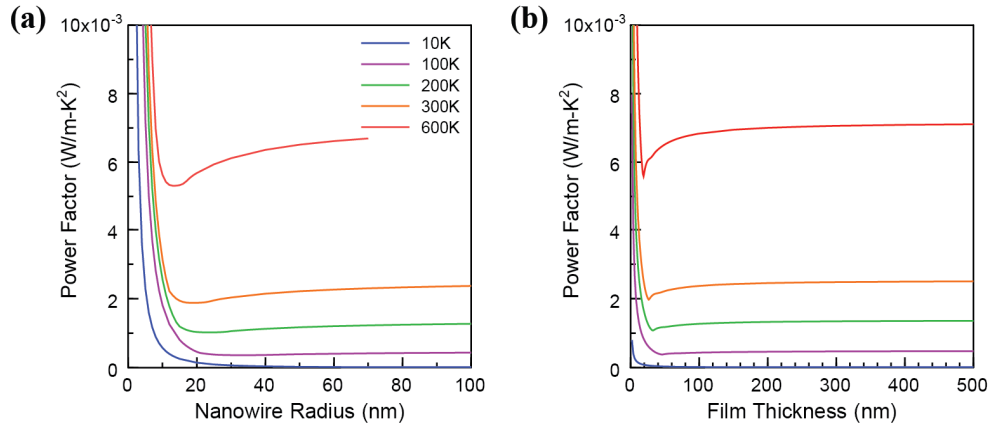
Figure 3.8: Power factor values calculated for InSb (a) as a function of nanowire radius and (b) as a function of thin film thickness for various temperatures 10-600K.
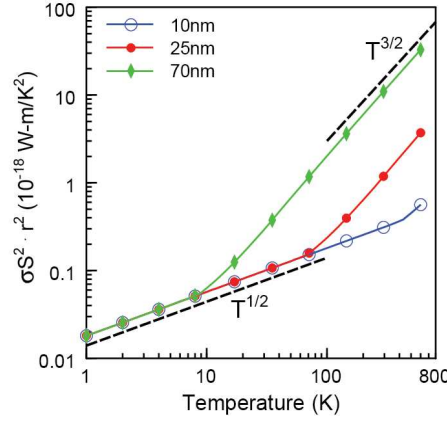
Figure 3.9: Log-log plot of the radius-normalized power factor $PF \cdot r^2$ for InSb as a function of temperature for different nanowire radii (solid lines). Power-law temperature-dependences (dashed lines) are shown as a guide.

temperature instead weakens the *effect* of confinement.

The optimal power factor of cylindrical nanowires of radius r=10, 25, 70nm are shown as a function of temperature on a log-log scale in Figure 3.9. For ease of comparison of data calculated for different radii, the power factor values have been normalized by the factor r^2 (as discussed in Sect. 2.6, the single-subband power factor is proportional to r^{-2}). For low temperatures (T<10K), the $PF \cdot r^2$ values are identical for all three radii--an indication that a single subband contributes to transport. In addition, the $PF \cdot r^2$ values for all three radii are proportional to $T^{1/2}$ in this range of low temperatures. At higher temperatures, $PF \cdot r^2$ is instead proportional to $T^{3/2}$, the temperature-dependence we saw for bulk systems. The temperature at which we see a transition from a $T^{1/2}$-dependence to a $T^{3/2}$-dependence varies depending on the nanowire radius. As one might expect, for large nanowires we see bulk-like behavior

for a wider range of temperatures (ex: for r=70nm, the power factor has a $T^{3/2}$-dependence at temperatures as low as 10K).

The temperature-dependence of the nanowire power factor, and the transition from $T^{1/2}$ the bulk $T^{3/2}$ dependence, can be understood with an argument analogous to the one given above for bulk systems. For highly confined nanowires in which a single subband E_{10} contributes to transport (an assumption appropriate for small nanowire radii or low temperatures), the power factor for a nanowire of radius r can be written

$$PF(r, E_f, T) = \left\{ 2 \frac{\mu}{\pi^2 r^2 \hbar} \cdot \frac{\sqrt{2m_\parallel^*}}{eT^2} \right\} \left[\frac{\left[\int_{E_{11}}^{\infty} dE \cdot \sqrt{E - E_{11}} \cdot \left(-\frac{\partial f}{\partial E} \right) \cdot (E - E_f) \right]^2}{\int_{E_{11}}^{\infty} dE \cdot \sqrt{E - E_{11}} \cdot \left(-\frac{\partial f}{\partial E} \right)} \right]. \quad (3.11)$$

where we have omitted the sum over the contributions of multiple subbands. We define normalized variables $x \equiv E/k_B T$ and $x_f \equiv E_f/k_B T$, and Eq. (3.11) becomes

$$PF(r, E_f, T) = \left\{ 2 \frac{\mu}{\pi^2 r^2 \hbar} \cdot \frac{\sqrt{2m_\parallel^*}}{e} (k_B)^2 (k_B T)^{1/2} \right\} \cdot C(x_f) \quad (3.12)$$

where

$$C(x_f) = \frac{\left[\int_{x_{11}}^{\infty} dx \cdot \sqrt{x - x_{11}} \cdot \left(-\frac{\partial f}{\partial x} \right) \cdot (x - x_f) \right]^2}{\int_{x_{11}}^{\infty} dx \cdot \sqrt{x - x_{11}} \cdot \left(-\frac{\partial f}{\partial x} \right)}$$

(3.13)

is the ratio of integrals. The normalized Fermi energy that maximizes both C and the power factor $(x_{f,opt})$ is independent of temperature, and it follows that $C(x_{f,opt})$ is also constant with respect to T. This means that for a given nanowire radius $r,$ the temperature-dependence of the optimized single-subband power factor therefore comes from the factor of $T^{1/2}$ in the energy-independent coefficient in Eq. (3.12).

66
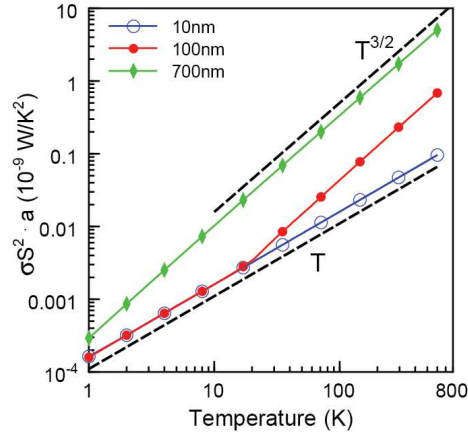
Figure 3.10: Log-log plot of the thickness-normalized power factor $PF \cdot a$ for InSb as a function of temperature for different film thicknesses. Power-law temperature-dependences (dashed lines) are shown as a guide.

Optimal power factor values calculated for thin films systems are shown as a function of temperature for various thicknesses (a=10, 100, 700nm) in Figure 3.10. The power factor values shown have been normalized by multiplying by a (for thin films, the single-subband power factor is proportional to a^{-1}). In thin films, $PF \cdot a$ is proportional to T at low temperatures and regains the bulk-like temperature dependence of $T^{3/2}$ at high temperatures.

The temperature dependence seen for low temperatures and small sizes ($T^{1/2}$ for nanowires, T for thin films) therefore indicates strong confinement, and that a single subband contributes to transport. The transition from a $T^{1/2}$ or T dependence to a $T^{3/2}$ dependence marks the transition from highly confined to weakly confined, bulk-like behavior. The sharp transition in the temperature dependence can therefore be used to determine the ranges of temperature and size in which the single-subband model is appropriate.
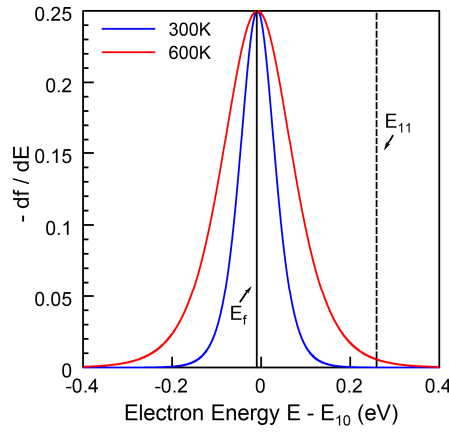
Figure 3.11: Derivative of the Fermi-Dirac distribution as a function of energy $E\text{-}E_{10}$ for temperatures of 300 and 600K. Also shown: the Fermi energy (vertical black line) and the second subband energy E_{11} (dashed vertical line) calculated for an InSb nanowire of radius 10nm.

For a specific nanowire radius or thin film thickness, the set of subband energies E_{nm} or E_n do not depend on temperature. However, the distribution of electrons around the Fermi energy *does* depend on temperature—the electrons that contribute to transport have energies that fall within several $k_B T$ of the Fermi energy. As the temperature increases, this distribution of electrons broadens, and the number of relevant subband energies increases (see Figure 3.11). An increase in temperature therefore results in weakened effects of confinement. This explains why the temperature of the transition between single-subband and bulk-like behavior is higher for smaller nanostructures.

3.6 *Summary*

In this chapter, we described a parametric study of the size-dependence of the power factor. We presented models for calculating the transport properties of square nanowires and thin films. Assuming the parameters of n-type InSb, the power factor

of these systems (like that of cylindrical nanowires) is non-monotonic with system size and falls below the bulk value for most of the size-range investigated. Then calculated the nanowire and power factor values for a range of material-specific parameters and different temperatures, and similar qualitative results were found.

The results in this chapter indicate that a non-monotonic size-dependence of the power factor of nanostructures is predicted for one-band isotropic conductors regardless of the nanostructure dimension or geometry (square nanowires, cylindrical nanowires and thin films), the particular carrier parameters assumed (effective mass, mobility and carrier relaxation time) and the temperature. The minimum in the power factor as a function of size, seen for each nanostructured system investigated, narrows and shifts to a smaller system size with decreasing confinement, e.g. through an increase in effective mass or through an increase in temperature.

Though all power factor results presented in this chapter for a *range* of material and system parameters show qualitatively the same dependence on size, the exact details of the size-dependent power factor curves (ex: the size corresponding to the minimum power factor value) vary for each system investigated. In Chapter 4, we develop analytical expressions for the size-dependent power factor of nanoscale systems that allow us to determine these system-specific details for *any arbitrary* set of material and system parameters.

Chapter 4 Derivation of Universal Scaling Relations for the Thermoelectric Power Factor of Nanostructures Under the Constant Relaxation Time Approximation

4.1 *Introduction*

In Chapter 3, we presented a parametric study of the effect of various system parameters on the thermoelectric power factor of nanostructures. The key finding of this study is that the size-dependence of the power factor of a single-carrier isotropic semiconductor is predicted to show qualitatively the same behavior regardless of the nanostructure geometry or dimension, temperature or specific values assigned to material parameters. The size-dependent power factor curves are all found to be non-monotonic, and the power factor of nanoscale systems is generally lower than that of bulk.

Despite these common characteristics, significant computational work was required to obtain the system-specific details presented in Chapter 3. In this chapter, we derive analytical expressions for the power factor of nanostructures that allow us to determine these details for all nanostructured systems. The power factor of nanostructured and bulk systems is a complicated function dependent on many material and system parameters: $PF_{nano,opt}(w, \mu, m_\parallel^*, m_\perp^*, T)$. In contrast, the universal curves derived here, $U_{nano}(s(w, \mu, m_\parallel^*, m_\perp^*, T))$, condense the complicated power factor function into a function that depends only on a single variable s. The

relationship between PF and U is given by

$$U_{nano}(s) = \frac{PF_{nano,opt}(w,\mu,m_\parallel^*,m_\perp^*,T)}{PF_{3D,opt}(\mu,m_\parallel^*,m_\perp^*,T)} \tag{4.1}$$

and the variable s is a function of size, effective mass and temperature (i.e. $s = s(w, m_\perp^*, T)$). The universal curves $U_{nano}(s)$ presented in this chapter then include all of the data presented in Chapter 2 and Chapter 3, and can be used to predict the power factor value of any single-carrier semiconducting nanostructure *without any additional computational effort.*

A detailed derivation of the universal curve for cylindrical nanowires is presented first, followed by brief derivations of the universal curves for other systems. The universal curves, like the calculated power factor results in Chapter 2 and Chapter 3, are derived under the constant relaxation time approximation ($\tau(E) = \tau = \mu m_\parallel^*/e$). The single carrier assumed is characterized by an ellipsoidal Fermi pocket with effective masses $m_\parallel^* \neq m_\perp^*$.

4.2 Universal Curve for Cylindrical Nanowires

To determine the dependence of the power factor on all system variables, we re-examine Eq. (2.18) (used to calculate the power factor of cylindrical nanowires with a single carrier type under the constant relaxation time approximation):

$$PF_{1D,circ}(r, E_f, \mu, m_\parallel^*, m_\perp^*, T) = \left\{ 2\frac{\mu}{\pi^2 r^2 \hbar} \cdot \frac{\sqrt{2m_\parallel^*}}{eT^2} \right\} \left[\frac{\left[\sum_{nm} \int_{E_{nm}}^{\infty} dE \cdot \sqrt{E-E_{nm}} \cdot \left(-\frac{\partial f}{\partial E}\right) \cdot (E-E_f) \right]^2}{\sum_{nm} \int_{E_{nm}}^{\infty} dE \cdot \sqrt{E-E_{nm}} \cdot \left(-\frac{\partial f}{\partial E}\right)} \right]$$

$$\tag{4.2}$$

where we have added the subscript "1D,*circ*" to distinguish from other forms of the power factor in this chapter. In Eq. (4.2), the power factor is the product of (1) an

energy-independent coefficient (surrounded by {}), and (2) the ratio of integrals (surrounded by [ ]) which depend on the set of subband energies $E_{nm}(r, m_\perp^*)$ and E_f.

Defining the normalized energy, $x \equiv \frac{E}{k_B T}$, the normalized Fermi energy $x_f \equiv \frac{E_f}{k_B T}$ and the normalized subband energies $x_{nm} \equiv \frac{E_{nm}}{k_B T}$, Eq. (4.2) becomes

$$PF_{1D,circ}\left(r, x_f, \mu, m_\parallel^*, m_\perp^*, T\right) =$$

$$\left\{ 2 \frac{\mu(k_B)^2}{\pi^2 r^2 \hbar} \cdot \frac{\sqrt{2m_\parallel^*}}{e} (k_B T)^{1/2} \right\} \cdot \left[\frac{\left[\sum_{nm} \int_{x_{nm}}^\infty dx \cdot \sqrt{x - x_{nm}} \cdot \left(-\frac{\partial f}{\partial x}\right) \cdot (x - x_f)\right]^2}{\sum_{nm} \int_{x_{nm}}^\infty dE \cdot \sqrt{x - x_{nm}} \cdot \left(-\frac{\partial f}{\partial x}\right)} \right].$$

$$(4.3)$$

We define new functions

$$D_{1D,circ}\left(r, \mu, m_\parallel^*, T\right) = 2 \frac{\mu(k_B)^2}{\pi^2 r^2 \hbar} \cdot \frac{\sqrt{2m_\parallel^*}}{e} (k_B T)^{1/2} \qquad (4.4)$$

and

$$B_{1D,circ}\left(x_f, x_{nm}\right) = \frac{\left[\sum_{nm} \int_{x_{nm}}^\infty dx \cdot \sqrt{x - x_{nm}} \cdot \left(-\frac{\partial f}{\partial x}\right) \cdot (x - x_f)\right]^2}{\sum_{nm} \int_{x_{nm}}^\infty dE \cdot \sqrt{x - x_{nm}} \cdot \left(-\frac{\partial f}{\partial x}\right)} \qquad (4.5)$$

such that

$$PF_{1D,circ}\left(r, x_f, \mu, m_\parallel^*, m_\perp^*, T\right) = D_{1D,circ}\left(r, \mu, m_\parallel^*, T\right) \cdot B_{1D,circ}\left(x_f, x_{nm}\right).$$

$$(4.6)$$

Note that the Fermi energy dependence of the power factor comes solely from $B_{1D,circ}\left(x_f, x_{nm}\right)$, so that the normalized Fermi energy that maximizes $B_{1D,circ}$ is the same as $x_{f,opt}$ (the normalized Fermi energy that optimizes $PF_{1D,circ}$). At the optimal Fermi energy, $B_{1D,circ}$ depends only on x_{nm} and we can write

$$B_{1D,circ}\left(x_{f,opt}, x_{nm}\right) = B_{1D,circ,opt}(x_{nm}). \qquad (4.7)$$

We use Eq. (2.13) to write

72

$$x_{nm} = \frac{E_{nm}}{k_B T} = \frac{j_{mn}^2 \hbar^2}{(2m_\perp^* r^2 k_B T)}, \tag{4.8}$$

so that

$$B_{1D,circ,opt}(x_{nm}) = B_{1D,circ,opt}(k_B T \cdot (m_\perp^* r^2 / \hbar^2)). \tag{4.9}$$

Thus, if we choose two nanowire systems a and b characterized by T_i, $m_{\perp,i}^*, r_i$ ($i=a$ and b) such that $k_B T_a \cdot (m_{\perp,a}^* r_a^2 / \hbar^2) = k_B T_b \cdot (m_{\perp,b}^* r_b^2 / \hbar^2)$, it follows that

$$x_{nm,a} = x_{nm,b}$$

$$B_{1D,circ}(x_f, x_{nm,a}) = B_{1D,circ}(x_f, x_{nm,b}) \tag{4.10}$$

$$x_{f,opt,a} = x_{f,opt,b} \; .$$

The unitless quantity $s_{1D,circ} \equiv k_B T \cdot (m_\perp^* r^2 / \hbar^2)$ is inversely proportional to the ratio of the quantization energy to the thermal energy $k_B T$: $x_{11} = \frac{j_{11}^2}{2s_{1D,circ}}, x_{12} = \frac{j_{11}^2}{2s_{1D,circ}}$, etc. This variable can be understood as a measure of the effective confinement in the nanowire: it takes into account the effects of size and effective mass on the subband structure and the effect of temperature on the distribution of electrons among the available subbands.

The power factor for cylindrical nanowires, optimized with respect to Fermi energy, can therefore be written as

$$PF_{1D,circ,opt}(r, \mu, m_\parallel^*, m_\perp^*, T) = D_{1D,circ}(r, \mu, m_\parallel^*, T) \cdot B_{1D,circ,opt}(s_{1D,circ.}). \tag{4.11}$$

We note that in the limit that a single-subband contributes to transport, $B_{1D,circ,opt}$ is constant (see Sect. 2.6) and $PF_{1D,circ,opt}(r) \propto 2 \frac{\mu (k_B)^2}{\pi^2 r^2 \hbar} \cdot \frac{\sqrt{2m_\parallel^*}}{e} (k_B T)^{1/2}$. This

73

expression shows the expected r^{-2} and $T^{1/2}$ dependences of the nanowire power factor in the single-subband model.

The universal curve for cylindrical nanowires is derived by dividing Eq. (4.11) by the optimized bulk power factor (from Eq. (3.9) and (3.10))

$$PF_{3D,opt}(\mu, m_{\parallel}^*, m_{\perp}^*, T) = D_{3D}(\mu, m_{\parallel}^*, m_{\perp}^*, T) \cdot B_{3D}(x_{f,opt}) \qquad (4.12)$$

where $D_{3D(\mu, m_{\parallel}^*, m_{\perp}^*, T)} = \left\{ \dfrac{\mu m_{\perp}^*}{3\pi^2 \hbar^3} \dfrac{(k_B)^2}{e} \sqrt{8 m_{\parallel}^*} (k_B T)^{3/2} \right\}$ and $B_{3D}(x_{f,opt}) = B_{3D,opt}$ is a

constant. As explained in Sect. 3.4.2 and 3.5.2, the dependence of the optimized bulk power factor on $\mu, m_{\parallel}^*, m_{\perp}^*$ and T comes solely from the energy-independent coefficient D_{3D}. The universal curve $U_{1D,circ.}$ for cylindrical nanowires is then defined as

$$U_{1D,circ.}(r, \mu, m_{\parallel}^*, m_{\perp}^*, T) = \frac{PF_{1D,circ.,opt}(r, \mu, m_{\parallel}^*, m_{\perp}^*, T)}{PF_{3D,opt}(\mu, m_{\parallel}^*, m_{\perp}^*, T)}$$

$$= \frac{D_{1D,circ.}(r, \mu, m_{\parallel}^*, T)}{D_{3D}(\mu, m_{\parallel}^*, m_{\perp}^*, T)} \cdot \frac{B_{1D,circ.,opt}(s_{1D,circ.})}{B_{3D,opt}}$$

$$= \frac{3\hbar^2}{k_B T \cdot (m_{\perp}^* r^2)} \cdot \frac{B_{1D,circ.,opt}(s_{1D,circ.})}{B_{3D,opt}}$$

$$= \frac{3}{B_{3D,opt}} \cdot \frac{1}{s_{1D,circ.}} \cdot B_{1D,circ.,opt}(s_{1D,circ.})$$

$$(4.13)$$

such that $U_{1D,circ.}$ is a function only of $s_{1D,circ.}$. The universal curve for cylindrical nanowires, shown as a function of the unitless quantity $s_{1D,circ.}$ in Figure 4.1, was derived without setting the values of r, μ, $m_{\parallel}^*, m_{\perp}^*$ or T; therefore, the curve in Figure 4.1 contains *all* of the optimized power factor data presented for cylindrical
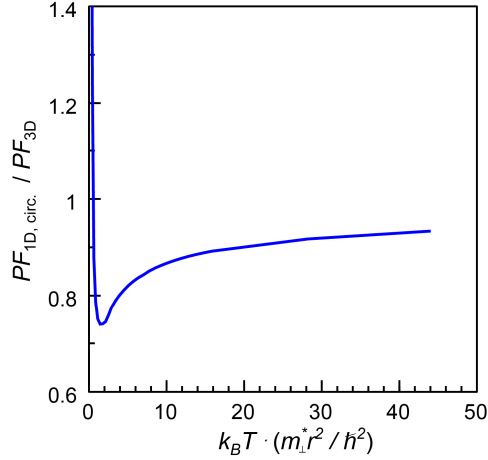
Figure 4.1: Universal curve derived for cylindrical nanowires.

nanowires in the parametric study in Chapter 2 and Chapter 3. This universal curve is common to all cylindrical nanowires of single-carrier materials with a spherical Fermi surface ($m_\parallel^* = m_\perp^*$), as well as those with an ellipsoid of revolution Fermi surface ($m_\parallel^* \neq m_\perp^*$).

The universal curve in Figure 4.1 exhibits a minimum at $s_{1D,circ.}$=1.427. At the minimum, the nanowire power factor falls 26% below the bulk value. For large values of $s_{1D,circ.}$ (weak effective confinement), the 1D power factor approaches that of bulk ($U \to 1$). In order for the nanowire power factor to be larger than bulk ($U \geq 1$), $s_{1D,circ.} \leq 0.5683$ is required.

4.3 *Universal Curve for Square Nanowires*

The universal curve for square nanowires is defined as the ratio of the optimized nanowire power factor to the optimized bulk power factor:

$$U_{1D,sq.}(l,\mu,m_\parallel^*,m_\perp^*,T) = \frac{PF_{1D,sq.,opt}(l,\mu,m_\parallel^*,m_\perp^*,T)}{PF_{3D,opt}} \qquad (4.14)$$

75

By a similar derivation to that given in Sect. 4.2, it can be shown that $U_{1D,sq.}$ depends on a single variable. The power factor of a square nanowire of width l is given by

$$PF_{1D,sq.}(l, E_f, \mu, m_\parallel^*, m_\perp^*, T) =$$

$$\left\{ 2\frac{\mu}{\pi l^2 \hbar} \cdot \frac{\sqrt{2m_\parallel^*}}{eT^2} \right\} \left[\frac{\left[\sum_{nm} \int_{E_{nm}}^\infty dE \cdot \sqrt{E-E_{nm}} \cdot \left(-\frac{\partial f}{\partial E}\right) \cdot (E-E_f) \right]^2}{\sum_{nm} \int_{E_{nm}}^\infty dE \cdot \sqrt{E-E_{nm}} \cdot \left(-\frac{\partial f}{\partial E}\right)} \right]. \tag{4.15}$$

We define $x \equiv \frac{E}{k_B T}$, $x_f \equiv \frac{E_f}{k_B T}$ and $x_{nm} \equiv \frac{E_{nm}}{k_B T}$ and Eq. (4.15) becomes

$$PF_{1D,sq.}(l, x_f, \mu, m_\parallel^*, m_\perp^*, T) = D_{1D,sq.}(l, \mu, m_\parallel^*, T) \cdot B_{1D,sq.}(x_f, x_{nm}) \tag{4.16}$$

where

$$D_{1D,sq.}(l, \mu, m_\parallel^*, T) = 2\frac{\mu(k_B)^2}{\pi l^2 \hbar} \cdot \frac{\sqrt{2m_\parallel^*}}{e} (k_B T)^{1/2} \tag{4.17}$$

and

$$B_{1D,sq.}(x_f, x_{nm}) = \frac{\left[\sum_{nm} \int_{x_{nm}}^\infty dx \cdot \sqrt{x-x_{nm}} \cdot \left(-\frac{\partial f}{\partial x}\right) \cdot (x-x_f) \right]^2}{\sum_{nm} \int_{x_{nm}}^\infty dE \cdot \sqrt{x-x_{nm}} \cdot \left(-\frac{\partial f}{\partial x}\right)} \tag{4.18}$$

For square nanowires, the normalized subband energies are given by

$$x_{nm} = \frac{E_{nm}}{k_B T} = \frac{\hbar^2 \pi^2 (n^2 + m^2)}{2m_\perp^* l^2 k_B T}. \tag{4.19}$$

Systems with identical values of the unitless quantity $s_{1D,sq.} \equiv k_B T \cdot (m_\perp^* l^2 / \hbar^2)$ therefore have the same set of normalized subband energies x_{nm}. $s_{1D,sq.}$ is inversely proportional to the normalized quantization energies (in fact, $s_{1D,sq.} = \left(\frac{x_{11}}{\pi^2}\right)^{-1}$) and can be understood as a measure of confinement in the system.

At the optimal Fermi energy, it follows from Eq. (4.18) and (4.19) that

$$B_{1D,sq.}(x_{f,opt}, x_{nm}) = B_{1D,sq.,opt}(s_{1D,sq.}). \tag{4.20}$$

The universal curve for square nanowires (Eq. (4.14)) is then given by

$$U_{1D,sq.}(l,\mu,m_\parallel^*,m_\perp^*,T) = \frac{PF_{1D,sq.,opt}(l,\mu,m_\parallel^*,m_\perp^*,T)}{PF_{3D,opt}}$$

$$= \frac{D_{1D,sq.}(l,\mu,m_\parallel^*,T)}{D_{3D}(\mu,m_\parallel^*,m_\perp^*,T)} \cdot \frac{B_{1D,sq.,opt}(s_{1D,sq.})}{B_{3D,opt}}$$

$$= \frac{2\dfrac{\mu(k_B)^2}{\pi l^2 \hbar} \cdot \dfrac{\sqrt{2m_\parallel^*}}{e}(k_B T)^{1/2}}{\dfrac{\mu m_\perp^*}{3\pi^2 \hbar^3}\dfrac{(k_B)^2\sqrt{8m_\parallel^*}}{e}(k_B T)^{3/2}} \cdot \frac{B_{1D,sq.,opt}(s_{1D,sq.})}{B_{3D,opt}}$$

$$= \frac{3\pi\hbar^2}{k_B T \cdot m_\perp^* l^2} \cdot \frac{B_{1D,sq.,opt}(s_{1D,sq.})}{B_{3D,opt}}$$

$$U_{1D,sq.}(s_{1D,sq.}) = \frac{3\pi}{B_{3D,opt}} \cdot \frac{1}{s_{1D,sq.}} \cdot B_{1D,sq.,opt}(s_{1D,sq.})$$

$$(4.21)$$

The universal curve for square nanowires is given as a function of $s_{1D,sq.}$ in Figure 4.2. In this case, the minimum in the nanowire power factor, located at
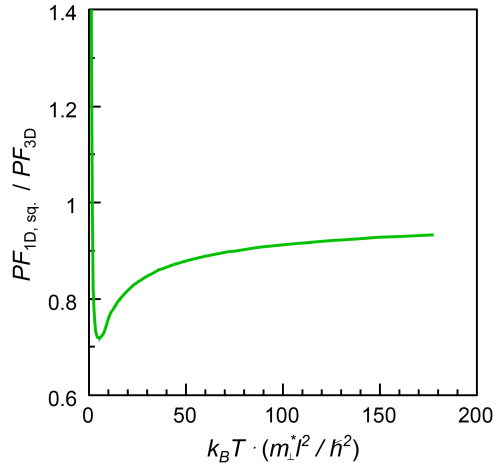
Figure 4.2: Universal curve for square nanowires.

$s_{1D,sq.} = 5.135$, is 28% below the bulk value is. For an increase in the power factor over the bulk value, systems must satisfy $s_{1D,sq.} \leq 1.733$.

4.4 *Universal Curve for Thin Films*

The universal curve for thin films is defined as

$$U_{2D}\left(a, \mu, m_{\parallel}^*, m_{\perp}^*, T\right) = \frac{PF_{2D,opt}\left(a, \mu, m_{\parallel}^*, m_{\perp}^*, T\right)}{PF_{3D,opt}}. \tag{4.22}$$

Through the derivation below, we show that U_{2D} is a function only of a single parameter s_{2D}.

For a thin film for thickness a, the power factor can be written as a function of Fermi energy as

$$PF_{2D}\left(a, E_f, \mu, m_{\parallel}^*, m_{\perp}^*, T\right) = \left\{2\frac{\mu}{\pi a \hbar^2} \cdot \frac{\sqrt{m_{\parallel}^* m_{\perp}^*}}{eT^2}\right\} \left[\frac{\left[\sum_n \int_{E_n}^{\infty} dE \cdot (E - E_n) \cdot \left(-\frac{\partial f}{\partial E}\right) \cdot (E - E_f)\right]^2}{\sum_n \int_{E_n}^{\infty} dE \cdot (E - E_n) \cdot \left(-\frac{\partial f}{\partial E}\right)}\right]. \tag{4.23}$$

In terms of normalized Fermi energy, $x_f \equiv \frac{E_f}{k_B T}$ and and subband energy $x_n \equiv \frac{E_n}{k_B T}$, Eq. (4.23) becomes

$$PF_{2D}\left(a, x_f, \mu, m_{\parallel}^*, m_{\perp}^*, T\right) = D_{2D}\left(a, \mu, m_{\parallel}^*, m_{\perp}^*, T\right) \cdot B_{2D}\left(x_f, x_n\right) \tag{4.24}$$

where

$$D_{2D}\left(a, \mu, m_{\parallel}^*, m_{\perp}^*, T\right) = 2\frac{\mu(k_B)^2}{\pi a \hbar^2} \cdot \frac{\sqrt{m_{\parallel}^* m_{\perp}^*}}{e} (k_B T) \tag{4.25}$$

and

$$B_{2D}\left(x_f, x_n\right) = \frac{\left[\sum_n \int_{x_n}^{\infty} dx \cdot (x - x_n) \cdot \left(-\frac{\partial f}{\partial x}\right) \cdot (x - x_f)\right]^2}{\sum_n \int_{x_n}^{\infty} dx \cdot (x - x_n) \cdot \left(-\frac{\partial f}{\partial x}\right)}. \tag{4.26}$$

The normalized subband energies have the form

$$x_n = \frac{\hbar^2 \pi^2 n^2}{2 m_\perp^* a^2 k_B T}. \tag{4.27}$$

Evaluated at the optimal Fermi energy, Eq. (4.26) is a function *only of the quantity* $s_{2D} \equiv k_B T \cdot (m_\perp^* a^2 / \hbar^2)$:

$$B_{2D}\left(x_{f,opt}, x_n\right) = B_{2D,opt}(s_{2D}). \tag{4.28}$$

The unitless variable s_{2D} is inversely proportional to the normalized subband energies x_n (e.g. $s_{2D} = \left(\frac{2x_1}{\pi^2}\right)^{-1} = \left(\frac{x_2}{2\pi^2}\right)^{-1} \ldots$). s_{2D} is then a measure the effect of confinement through the spread between subband energies and the distribution of relevant electrons (defined by temperature T) within this electronic subband structure.

The optimal thin film power factor can be written as

$$PF_{2D,opt}\left(a, \mu, m_\parallel^*, m_\perp^*, T\right) = 2 \frac{\mu (k_B)^2}{\pi a \hbar^2} \cdot \frac{\sqrt{m_\parallel^* m_\perp^*}}{e} (k_B T) \cdot B_{2D,opt}(s_{2D}).$$

$$(4.29)$$

For strongly confined films, in which a single-subband contributes to transport, the optimized ratio of integrals $B_{2D,opt}$ is a constant, leading to $PF_{2D,opt} \propto 2 \frac{\mu (k_B)^2}{\pi a \hbar^2} \cdot \frac{\sqrt{m_\parallel^* m_\perp^*}}{e} (k_B T)$. This relation shows the a^{-1} and T dependences demonstrated in Sect. 3.3.

The universal curve for two-dimensional thin films from Eq. (4.22) can then be written as

$$U_{2D}\left(a, \mu, m_\parallel^*, m_\perp^*, T\right) = \frac{PF_{2D,opt}\left(a, \mu, m_\parallel^*, m_\perp^*, T\right)}{PF_{3D,opt}}$$

$$= \frac{D_{2D,opt}\left(a, \mu, m_{\parallel}^*, m_{\perp}^*, T\right)}{D_{3D}\left(\mu, m_{\parallel}^*, m_{\perp}^*, T\right)} \cdot \frac{B_{2D,opt}\left(k_B T \cdot (m_{\perp}^* a^2/\hbar^2)\right)}{B_{3D,opt}}$$

$$= \frac{2\dfrac{\mu}{\pi a \hbar^2} \cdot \dfrac{\sqrt{m_{\parallel}^* m_{\perp}^*}}{eT^2}}{\dfrac{\mu m_{\perp}^*}{3\pi^2 \hbar^3} \dfrac{(k_B)^2 \sqrt{8 m_{\parallel}^*}}{e}} \cdot \frac{B_{2D,opt}\left(k_B T \cdot (m_{\perp}^* a^2/\hbar^2)\right)}{B_{3D,opt}}$$

$$= \frac{3\pi}{\sqrt{2}} \cdot \frac{\hbar}{\sqrt{k_B T \cdot m_{\perp}^* a^2}} \cdot \frac{B_{2D,opt}(s_{2D})}{B_{3D,opt}}$$

$$U_{2D}(s_{2D}) = \frac{3\pi}{\sqrt{2}B_{3D,opt}} \cdot \frac{1}{\sqrt{s_{2D}}} \cdot B_{2D,opt}(s_{2D}).$$

$$(4.30)$$

U_{2D} is a function only of s_{2D}.

The universal curve for thin films is shown as a function of s_{2D} in Figure 4.3. The single curve in Figure 4.3 can be used to predict the optimal power factor of a thin film for any arbitrary choice of sizes, carrier parameters and temperatures (and therefore includes all of the thin film data in Chapter 3). The minimum for thin film
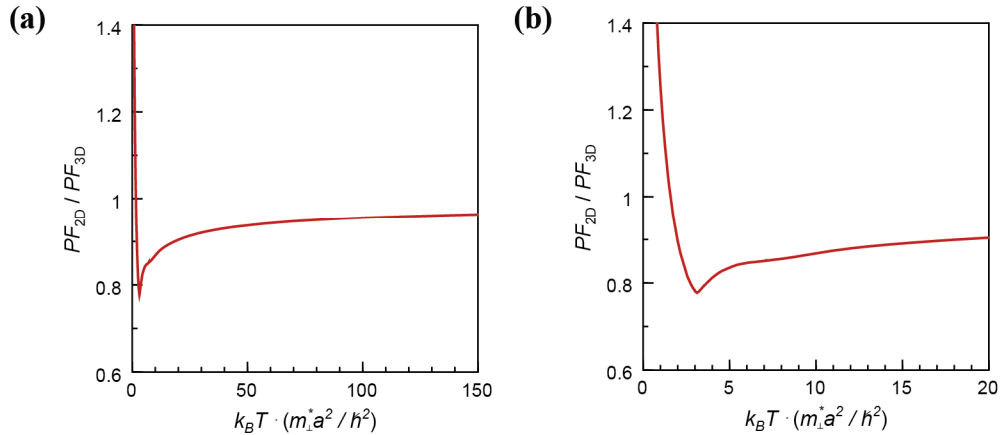
Figure 4.3: Universal curve for thin films. Plot in (b) focuses on the minimum.

systems, at $s_{2D}=3.120$, is 22% below the bulk value. Improvement over bulk requires $s_{2D} \leq 1.591$.

4.5 *Comparison of the Universal Curves for Different Systems*

In the above discussion, we analyzed the power factor functions

$$PF\left(w,\mu,m_\parallel^*,m_\perp^*,T,x_f\right) = \left\{D\left(w,\mu,m_\parallel^*,m_\perp^*,T\right)\right\} \cdot B\left(x_f,w,m_\perp^*,T\right) \qquad (4.3)$$

for various nanostructured systems where w is the nanostructure size. For each choice of x_f, the function B (the ratio of integrals) depends only on the effective confinement in the system, $s(w,m_\perp^*,T)$.

The functions D, B and s are compared for the nanostructure systems studied here in Table III. The corresponding bulk forms (which do not depend on size) are given for reference in the bottom row.

Table III. Forms of the components (D and B) of the thermoelectric power factor, the variable s and the normalized subband energies x_{nm} or x_n are compared for nanowire, thin film and bulk systems.

System	$D(w,\mu,m_\parallel^*,m_\perp^*,T)$	$B(x_f,s(w,m_\perp^*,T))$	$s(w,m_\perp^*,T)$	$x_n(s)$ or $x_{nm}(s)$
1D, Cylindrical Nanowires	$2\frac{\mu(k_B)^2}{\pi^2 r^2 \hbar}\cdot\frac{\sqrt{2m_\parallel^*}}{e}(k_BT)^{1/2}$	$\dfrac{\left[\sum_{nm}\int_{x_{nm}}^\infty dx\cdot\sqrt{x-x_{nm}}\cdot\left(-\frac{\partial f}{\partial x}\right)\cdot(x-x_f)\right]^2}{\sum_{nm}\int_{x_{nm}}^\infty dE\cdot\sqrt{x-x_{nm}}\cdot\left(-\frac{\partial f}{\partial x}\right)}$	$k_BT\cdot\frac{m_\perp^* r^2}{\hbar^2}$	$\dfrac{j_{nm}^2}{2s}$
1D, Square Nanowires	$2\frac{\mu(k_B)^2}{\pi l^2 \hbar}\cdot\frac{\sqrt{2m_\parallel^*}}{e}(k_BT)^{1/2}$	$\dfrac{\left[\sum_{nm}\int_{x_{nm}}^\infty dx\cdot\sqrt{x-x_{nm}}\cdot\left(-\frac{\partial f}{\partial x}\right)\cdot(x-x_f)\right]^2}{\sum_{nm}\int_{x_{nm}}^\infty dE\cdot\sqrt{x-x_{nm}}\cdot\left(-\frac{\partial f}{\partial x}\right)}$	$k_BT\cdot\frac{m_\perp^* l^2}{\hbar^2}$	$\dfrac{\pi^2(n^2+m^2)}{2s}$
2D, Thin Films	$2\frac{\mu(k_B)^2}{\pi a\hbar^2}\cdot\frac{\sqrt{m_\parallel^* m_\perp^*}}{e}(k_BT)$	$\dfrac{\left[\sum_n\int_{x_n}^\infty dx\cdot(x-x_n)\cdot\left(-\frac{\partial f}{\partial x}\right)\cdot(x-x_f)\right]^2}{\sum_n\int_{x_n}^\infty dx\cdot(x-x_n)\cdot\left(-\frac{\partial f}{\partial x}\right)}$	$k_BT\cdot\frac{m_\perp^* a^2}{\hbar^2}$	$\dfrac{\pi^2 n^2}{2s}$
3D, Bulk Systems	$2\frac{\mu(k_B)^2}{3\pi^2\hbar^3}\frac{m_\perp^*\sqrt{2m_\parallel^*}}{e}(k_BT)^{3/2}$	$\dfrac{\left[\int_0^\infty dx\cdot\sqrt{x^3}\cdot\left(-\frac{\partial f}{\partial x}\right)\cdot(x-x_f)\right]^2}{\int_0^\infty dx\cdot\sqrt{x^3}\cdot\left(-\frac{\partial f}{\partial x}\right)}$	N.A.	N.A.

The universal curve is then defined as the power factor of the nanostructured system evaluated at the optimal Fermi energy divided by the optimized bulk power factor. The ratio

$$U(w.\mu,m_\parallel^*,m_\perp^*,T) = \frac{PF_{nano,opt}(w,\mu,m_\parallel^*,m_\perp^*,T)}{PF_{3D,opt}} \tag{4.32}$$

then simplifies to

$$U(s) = G(s)\cdot\frac{B_{nano,opt}(s)}{B_{3D,opt}} \tag{4.33}$$

where $G(s) = \frac{\{D(w,\mu,m_\parallel^*,m_\perp^*,T)\}}{\{D_{3D}(\mu,m_\parallel^*,m_\perp^*,T)\}}$ is only a function of s. The various forms of $G(s)$ for this set of nanostructures are given in Table IV.

Table IV. Forms of the function $G(s)$ and characteristic values of the universal curves for each nanostructured system.

System	$G(s)$	s @ $U(s)$=1	s @ $U_{\min}$	$U_{\min}$
1D, Cylindrical Nanowires	$3 \cdot \dfrac{1}{s}$	0.5683 ($\pi \cdot s$ =1.7854)	1.427 ($\pi \cdot s$ =4.4831)	0.74
1D, Square Nanowires	$3\pi \cdot \dfrac{1}{s}$	1.7333	5.135	0.72
2D, Thin Films	$\dfrac{3\pi}{\sqrt{2}} \cdot \dfrac{1}{\sqrt{s}}$	1.591	3.120	0.78

The non-monotonic universal power factor curves $U(s)$ are the product of $G(s)$ and $\dfrac{B_{nano,opt}(s)}{B_{3D,opt}}$. $G(s)$ decreases monotonically with s for each of the nanostructured systems. G is a slightly weaker function of s in thin film systems than in nanowire systems, indicating that the effect of confinement is less significant. The function $B_{nano,opt}(s)$, on the other hand, increases monotonically with s. $B_{nano,opt}(s)$ includes a sum over the contributions of many subbands to transport (Eq. (4.5), (4.18), (4.26)); as s increases (i.e. as confinement weakens through an increase in size, temperature and/or effective mass), the number of subbands contributing to transport increases. The minimum in the universal curve is the result of these two competing trends: (1) In the limit highly confined single-subband systems, $B_{nano,opt}(s)$ is constant and $U(s) \propto G(s)$ decreases with increasing s. (2) As s increases and confinement weakens, $B_{nano,opt}(s)$ increases and $U \to 1$.

We note that while the power factor of each particular system depends on mobility and effective mass in the transport direction (see Table III) these parameters do not appear in the universal curves in Table IV. This result indicates that high values of μ and $m_\parallel^*$, which equally affect the power factor of nanostructures and bulk systems, are not essential for $PF_{nano} > PF_{3D}$.

The characteristic values of the universal curves for each system are also compared in Table IV. The characteristic values of the universal curves for each system are also compared in Table IV. s @ $U(s)=1$ denotes the maximum s value for which the power factor of the nanostructure is larger than bulk, s @ U_{min} is the s value corresponding to the minimum in the universal curve, and U_{min} is the value of U at the minimum. For cylindrical nanowires, the values in parentheses have been multiplied by π to take into account the difference in cross-sectional area when comparing with the s-values for square nanowires. Due to weaker confinement, the characteristic s-values are lower and the minimum U value is higher for 2D compared with 1D systems. For highly confined nanowires in which a single subband contributes to transport, $U(s) \propto G(s)$ is identical for a given cross-sectional area, regardless of the nanowire shape. As such, the values of s @ $U(s)=1$, which fall within this range of highly confined systems, are within 5% for square and cylindrical nanowires. The minimum in the universal curve, on the other hand, also depends on the function $B_{nano,opt}(s)$. Thus, s @ U_{min} is smaller for the stronger confined square nanowires than for cylindrical nanowires.

4.6 Summary

In this chapter, we derived universal scaling relations for the thermoelectric power factor of nanowires and thin films. There are two important consequences of these universal curves. First, they allow us to make general conclusions about the power factor of nanostructured materials. The non-monotonic size-dependence of the power factor, and the decrease in the power factor relative to bulk, is due to *fundamental changes* in the electronic subband structure, and is not system-, material- or temperature-specific. Second, the universal curves derived here can be used to predict the power factor value of any single-carrier isotropic semiconductor in any system configuration, without additional computational effort. As described below, these universal curves are therefore an essential guide for experimental work in the field of nanostructured thermoelectrics.

The universal curves presented here indicate that, for most configurations, the power factor of nanoscale systems is lower than the bulk value. For the simple nanostructures studied thus far (nanowires and thin films), improvement over bulk is only predicted for *small sizes, low temperatures and/or low effective mass values*. However, the optimal bulk power factor is proportional to $m_\perp^* \sqrt{m_\parallel^*} (T)^{3/2}$ (see Eq. 4.11). Finding materials systems that are both promising in bulk *and* have the potential for power factor improvement with nanostructuring requires balancing these material and system parameters, and should therefore prove difficult.

In light of this, the most significant impact of the universal curves on future experimental work may lie in prediction of the minimum in the power factor of simple nanostructures. For a given material and temperature, the universal curves can

be used to determine the range of nanowire radii or thin film thicknesses such that the expected decrease in the power factor relative to bulk is more than made up for by a decrease in thermal conductivity.

Chapter 5 Effect of the Energy Dependence of the Carrier Scattering Time on the Size-Dependence of the Thermoelectric Power Factor of Thin Films

5.1 *Introduction*

The models for calculation of the thermoelectric transport properties of nanowires and thin films presented in Chapter 2 and Chapter 3 were derived employing the constant relaxation time approximation (CRTA): all carriers are assumed to have the same value of τ (and μ), independent of carrier energy. However, in typical thermoelectric materials (highly doped semiconductors) at room temperature, the dominant scattering mechanisms are scattering off of phonons (acoustic and optical) and ionized impurities. In general, the relaxation times associated with these scattering mechanisms are dependent on the carrier energy. In this chapter, we investigate the size-dependence of the power factor of nanoscale systems for which the scattering time varies with carrier energy. We present results for a range of scattering models which includes those relevant to room temperature thermoelectric materials. We explore the effect of the particular energy dependence of the scattering time on the magnitude of the power factor, and discuss introducing an additional scattering mechanism (e.g. scattering at grain boundaries) as a potential means for increasing the power factor of thermoelectric materials.

5.2 Theory and Procedure

The relaxation time associated with many scattering mechanisms can be modeled as a function of carrier energy as

$$\tau(E) = C \left(\frac{E}{k_B T} \right)^p \tag{5.1}$$

where $\tau(E)$ is the scattering time, C is a constant with units of time and p defines the exponential energy-dependence of the scattering time (frequently referred to as the "scattering parameter"[24, 58]). In Eq. (5.1), the carrier energy E is given relative to the conduction band edge (defined earlier as E_c in bulk, E_1 in thin film systems and E_{10} in nanowire systems). When multiple scattering processes are relevant to transport, the total scattering rate $\tau(E)^{-1}$ can be written via Matthiessen's rule:

$$\tau(E)^{-1} = \sum_i \tau_i(E)^{-1} = \sum_i \left(C_i \left(E \frac{E}{k_B T} \right)^{p_i} \right)^{-1} \tag{5.2}$$

where the sum in Eq. (5.2) is taken over the different i scattering mechanisms. In this work, we investigate systems with a range of scattering parameters between -0.8 and 1.5. The p-values associated with scattering processes relevant in thermoelectric materials generally fall within this range. For example, the scattering rate may be proportional to the density of final states; for bulk this corresponds to p=-0.5, for quantum wells p=0 and nanowires p=0.5.[59] This model is often associated with scattering of electrons by acoustic phonons.[60] Another example is a system in which the scattering rate is proportional to the carrier velocity. For the parabolic band assumed here, this corresponds to p=-0.5 for all dimensions.[59] The range of energy-dependences studied also includes those associated with scattering by ionized impurities[61] and polar optical phonons[62], though the equations frequently used to model the relaxation times for these mechanisms cannot be written explicitly in terms

of a single exponent p_i.

The discussion below focuses on calculations done for thin film systems. The results presented in this chapter were calculated for room temperature n-type InSb. We note, however, that the qualitative trends shown below are not specific to this temperature or band structure. Calculations were also done for nanowire systems leading to similar results, and were reported in [63].

For each choice of $\tau(E)$, the procedure for calculating the size-dependent power factor is similar to those described in Sect. 3.3. We calculate the transport properties as a function of Fermi energy $\sigma(E_f), S(E_f), \kappa_e(E_f), PF(E_f)$ for thin films with thicknesses in the range of 10-100nm. The average scattering time $\langle \tau \rangle$, which (as explained below) is necessary to normalize the power factor values, is calculated from the conductivity and the carrier concentration using

$$\langle \tau \rangle (E_f) = \frac{m^*}{e^2} \frac{\sigma(E_f)}{n(E_f)} .$$ (5.3)

where the carrier concentration n is calculated as a function of Fermi energy via

$$n(E_f) = \int_0^\infty dE \, DOS(E) \cdot f(E, E_f)$$ (5.4)

In Eq. (5.4), DOS(E) dE is the electron density-of-states function (per m^{-3}), $f(E)$ is the Fermi-Dirac distribution and the energies are relative to the conduction band edge. For thin films,

$$DOS_{2D}(E)dE = \frac{m^*}{\pi \hbar^2 a} \sum_n H(E - E_n)dE$$ (5.5)

where H is the Heaviside function and the sum is over 300 subband energies calculated using Eq. (3.6).

Analogous bulk calculations of $\sigma(E_f), S(E_f), \kappa_e(E_f), PF(E_f)$ are done for every choice of $\tau(E)$. The bulk $\langle\tau\rangle$ and n are calculated using Eq. (5.3) and (5.4) by plugging in 3D form of the density-of-states:

$$DOS_{3D}(E)dE = \frac{\sqrt{2}(m^*)^{3/2}}{\pi^2\hbar^3}\sqrt{E}dE. \tag{5.6}$$

For each scattering term in Eq. (5.2), there are two independent parameters: (1) the coefficient C_i, which determines the magnitude of the scattering time and (2) the exponent p_i, which controls the energy-dependence of the scattering time. From the equations for the thin film and bulk power factor, it can be shown that the power factor increases monotonically with the magnitude of the scattering time. For example, if $\tau(E) = C\left(\frac{E}{k_BT}\right)^p$ (Eq. 3.1), the power factor $PF(E_f) \propto C$. We are interested in how the thermoelectric power factor is affected specifically by changes in the *energy-dependence* of τ. To eliminate the effect of changing the *magnitude* of the scattering time, the power factor values shown in this chapter are normalized such that the magnitude of $\langle\tau\rangle$ is equal for all systems. This is done by multiplying the power factor $PF(E_f)$ by the ratio $\frac{\tau_{CRTA}}{\langle\tau\rangle(E_f)}$, where $\tau_{CRTA} = 5.18x10^{-13}$sec is the constant relaxation time in n-type InSb. The optimal Fermi energy $E_{f,opt}$ is then defined for this investigation as the Fermi energy that maximizes the quantity $PF(E_f)\cdot\left(\frac{\tau_{CRTA}}{\langle\tau\rangle(E_f)}\right)$. This normalization is equivalent to choosing coefficients C_i such that at $E_{f,opt}$, the average scattering time is fixed:

$$\langle\tau\rangle(E_{f,opt}) = \tau_{CRTA}. \tag{5.7}$$

This normalization is done for each set of calculations: for all scattering models, for each thickness a and for bulk systems. In the following discussion, the optimal power factor or PF then refers to power factor values that have been normalized and optimized in this way (i.e. $PF(E_{f,opt}) \cdot \left(\frac{\tau_{CRTA}}{\langle \tau \rangle (E_{f,opt})} \right)$).

5.3 Scattering Time Modeled with Single Power Dependence

We first focus on systems in which the scattering time is modeled with a single power-dependence on energy: $\tau(E) = C \left(\frac{E}{k_B T} \right)^p$. Optimized power factor values are given as a function of a for p values between -0.8 and 1.5 in Figure 5.1(a). For each choice of p, the power factor exhibits a similar non-monotonic dependence on film thickness. For thicknesses smaller than that of the minimum, the power factor
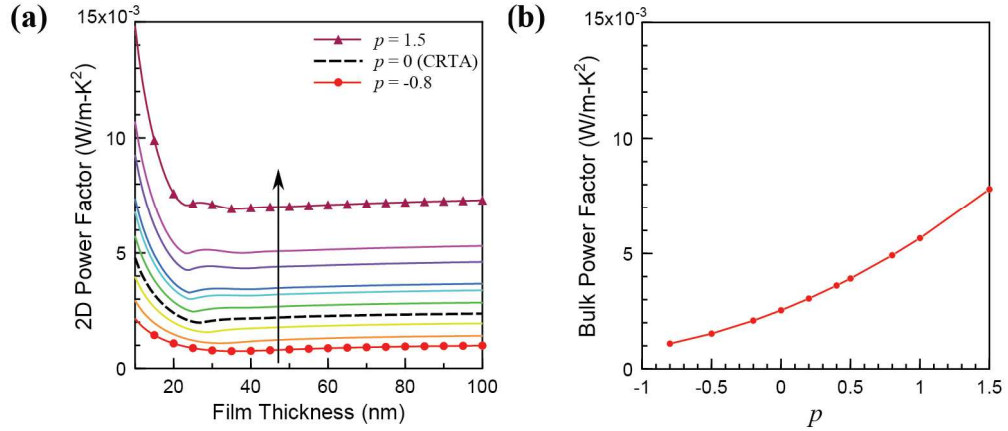
Figure 5.1: (a) Optimal power factor values as a function of film thickness for n-type InSb for the range of p values investigated. The black arrow indicates the trend of increasing p. Starting with the bottom curve, the values of p are -0.8, -0.5, -0.2, 0 (CRTA), 0.2, 0.4, 0.5, 0.8, 1 and 1.5. (b) Optimized bulk power factor values as a function of p.

values increases monotonically with decreasing size. For larger thicknesses, the thin film power factor increases up to the bulk value (Figure 5.1(b)). For $p>0.2$, this increase is not monotonic: Slight oscillations, most exaggerated for $p=1.5$, can be seen in the thickness-dependence of the power factor. For each thin film thickness a, on the other hand, the optimized power factor increases monotonically with p. A similar increase with p is seen for optimized bulk power factor values (see Figure 5.1(b)).

The contour plot in Figure 5.2(a) shows the optimized power factor values from Figure 5.1(a) as a function of a and p, normalized with respect to the optimized bulk value (Figure 5.1(b)) for each p. This analysis therefore implies that for the material of interest, the value of p in Eq. (5.1) is independent of size. The dashed black line marks the thickness at which the thin film power factor is equal to the bulk
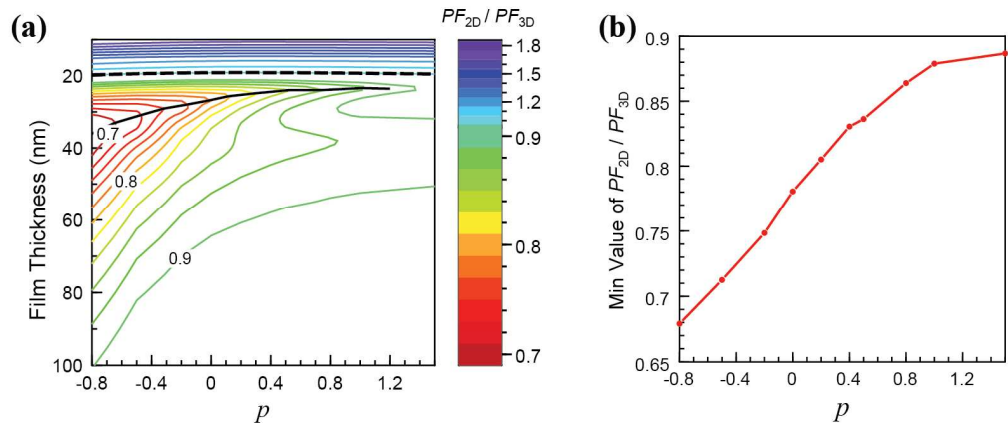
Figure 5.2: (a) Thin film power factor values, normalized with respect to bulk, as a function of film thickness and p. The dashed black line marks $\frac{PF_{2D}}{PF_{3D}} = 1$, and the minimum $\frac{PF_{2D}}{PF_{3D}}$ for each p is marked by a solid black line. (b) Minimum $\frac{PF_{2D}}{PF_{3D}}$ value as a function of p.

power factor ($\frac{PF_{2D}}{PF_{3D}} = 1$), and is between 19 and 20nm for the entire range of p

values. For all thicknesses larger than 20nm (regardless of the particular scattering

model), the thin film power factor is lower than that of bulk. The minimum in the *PF*

vs. *a* curve is marked as a solid black line, and varies smoothly between *a*=36nm (*p*=-

0.8) and *a*=23nm (*p*=1). As discussed in Sect. 3.4, this indicates weakening

confinement. For *p*=1.5, the minimum in the power factor jumps to 36nm. The value

of the minimum $\frac{PF_{2D}}{PF_{3D}}$, given as a function of *p* in Figure 5.2(b), increases from 0.68

for *p*=-0.8 to 0.89 for *p*=1.5. As *p* increases and confinement weakens, the thin film

power factor values do not fall as far below bulk. This result indicates nanostructuring

may be most counterproductive in systems with a low effective *p* value.

The results in Figure 5.1 and Figure 5.2 reveal several trends: (1) For each

thickness *a* and for bulk systems, the optimized power factor increases monotonically

with *p*. (2) Unlike what was seen for calculations done with the CRTA, for large *p*

values the optimized power factor of thin films exhibits secondary minima and

maxima as a function of thickness. (3) For thicknesses larger than 31nm, the ratio

$\frac{PF_{2D}}{PF_{3D}}$ increases monotonically with *p*. These trends are explained below. We note

that similar results and trends are also seen for cylindrical nanowires, and are

described in [63].

1. The optimized power factor of all systems increases with *p* due to an increase in

the scattering time of *high-energy electrons,* which has two effects. First, through the

energy-dependence of the scattering time, electrons are weighted based on their

energy relative to the conduction band edge, creating an additional asymmetry in the
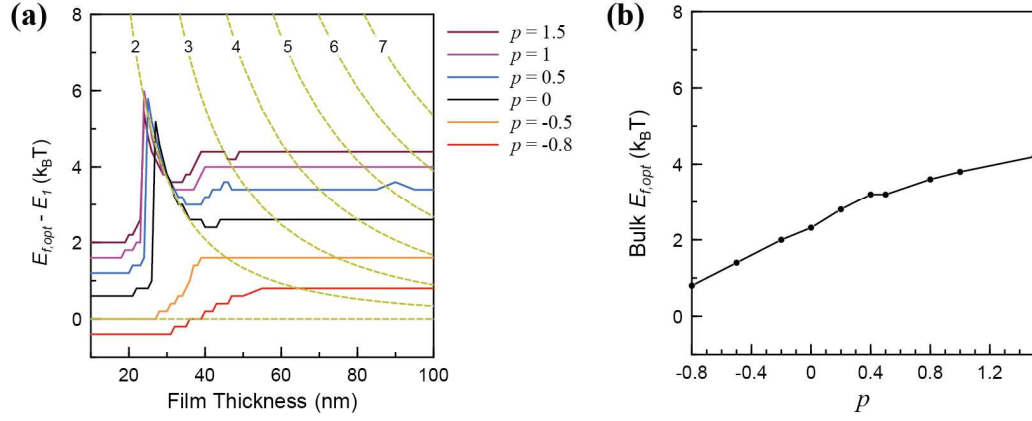
Figure 5.3: (a) The optimal Fermi energy, $E_{f,opt} - E_1$ (solid lines) as a function of film thickness for several p values. Dashed yellow lines mark the first seven subband energies (labeled by subband number) as a function of film thickness. (b) Optimal Fermi energy for bulk systems, as a function of p.

integrand of $\mathbf{L}^{(1)}$ around the Fermi energy (Eq. (2.5)). In general, this kind of asymmetry (in $DOS(E - E_f) \cdot \tau(E - E_f)$) leads to an increase in the Seebeck coefficient.[64]

The second effect is understood by looking at the data in Figure 5.3: In (a), the optimal Fermi energy $E_{f,opt} - E_1$ is given as a function of thickness for various p values and in (b), bulk $E_{f,opt}$ values are given as a function of p. As p increases, for each film thickness and for bulk the optimal Fermi energy increases further into the band, giving rise to a higher carrier concentration and a higher electrical conductivity. This is due to the increasing contribution of high energy electrons. Transport is dominated by the subbands that fall within several $k_B T$ of the Fermi energy. As p increases, the states weighted with the highest value of τ move from those very close to the band edge ($p<0$) to those far into the band ($p>0$). As the result of these two effects, an increase in p corresponds to an increase in the optimized thermoelectric

94

power factor of 1D[63], 2D and 3D systems.

2. The oscillations in the thickness-dependent power factor curves for $p>0.2$ (Figure 5.1(a)) are attributed to the movement of the subband energies (shown in Figure 5.3(a) as dashed yellow lines) relative to the Fermi energy as the thickness changes. The oscillations in the thin film power factor are strongest for large p values, for which the contribution of high-energy subbands is strongest. $E_{f,opt} - E_1$ then jumps significantly as a function of size to meet these higher-energy subbands. For $p<0$, on the other hand, low-energy subbands are weighted the most and the optimal Fermi energy moves smoothly between the single-subband value and the bulk value (remaining close to E_1). As a result, no oscillations are seen in the thickness-dependent power factor.

3. For all thicknesses larger than 31nm, the ratio $\frac{PF_{2D}}{PF_{3D}}$ increases monotonically with p. This, like the increase in PF_{2D} and PF_{3D} with p, can be explained by the movement of the thin film Fermi energy $E_{f,opt} - E_1$ with changing p (Figure 5.3(a)). As the optimal Fermi energy increases into the band, additional subbands become close to $E_{f,opt} - E_1$ and are relevant to transport. For a given thickness (under these weakly confined conditions), the density-of-states is more bulk-like at higher Fermi energies. Thus, an increase in p translates to a power factor value closer to bulk (PF_{2D} approaches PF_{3D}), and $\frac{PF_{2D}}{PF_{3D}}$ increases.

5.4 Calculations for Systems with Two Scattering Terms

In this section, we consider thin film systems in which the scattering rate is the combination of two terms:

$$\tau^{-1} = \tau_1^{-1} + \tau_2^{-1} = \left(\frac{1}{C_1\left(\frac{E}{k_B T}\right)^{p_1}} + \frac{1}{C_2\left(\frac{E}{k_B T}\right)^{p_2}} \right) \qquad (5.8)$$

where C_1 (C_2) and p_i (p_2) are the constant coefficient and scattering parameter associated with mechanism 1 and 2, respectively. For this study, we select $p_1=-0.5$ and $p_2=0.4$. As mentioned above, $p=-0.5$ is typically used to model scattering of carriers by acoustic phonons in bulk systems. The second scattering parameter, $p=0.4$, represents a scattering mechanism that most affects low-energy carriers (ex: ionized impurity scattering). Taking $\frac{C_1}{C_2} = 1$ as an example, the scattering times τ_1, τ_2 and the total τ are given as a function of energy relative to the conduction band edge in Figure 5.4(a). Depending on the choice of coefficient ratio $\frac{C_1}{C_2}$, the total scattering time τ may decrease monotonically (e.g. $\frac{C_1}{C_2} = 0$), increase monotonically (e.g. $\frac{C_1}{C_2} = \infty$) or
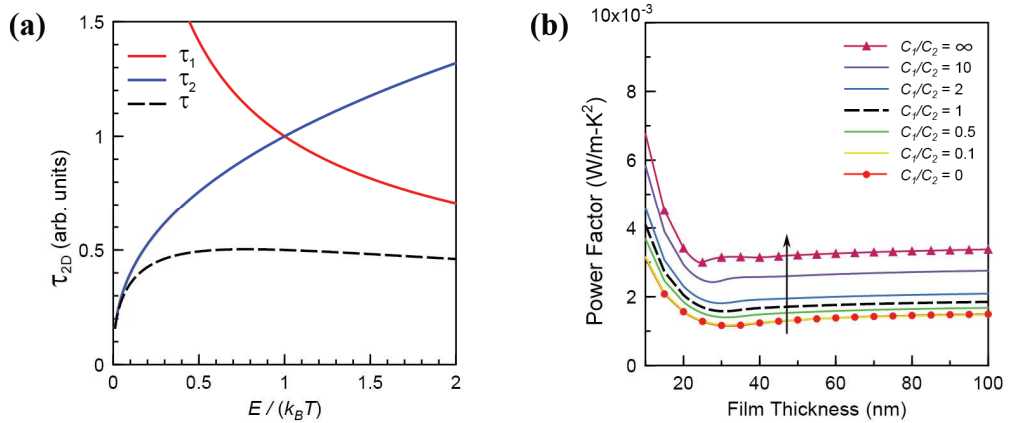
Figure 5.4: (a) Scattering times $\tau_1 = C_1 \left(\frac{E}{k_B T}\right)^{-0.5}$, $\tau_2 = C_2 \left(\frac{E}{k_B T}\right)^{0.4}$ and the total $\tau = (\tau_1^{-1} + \tau_2^{-1})^{-1}$ (the example $\frac{C_1}{C_2} = 1$) as a function of energy relative to the conduction band edge. (b) Optimized power factor values as a function of film thickness for $p_1=-0.5$ and $p_2=0.4$ and various ratios of coefficients C_1 and C_2. The black arrow indicates the direction of increasing $\frac{C_1}{C_2}$.

exhibit a maximum (e.g. $\frac{C_1}{C_2} = 1$, as in Figure 5.4(a)).

Optimized thin film power factor values are shown in Figure 5.4(b) as a function of film thickness for various coefficient ratios. The black dashed line marks calculations done for $\frac{C_1}{C_2} = 1$ (the same τ shown in Figure 5.4(a)). For each thickness a, the power factor values increase monotonically between the two extreme cases: (1) $\frac{C_1}{C_2} = 0$, corresponding to a single scattering term with $p=-0.5$, and (2) $\frac{C_1}{C_2} = \infty$, corresponding to a single scattering term with $p=0.4$. The minimum in the power factor, seen for each curve, shifts from 32nm (for $\frac{C_1}{C_2} = 0$) to 25nm (for $\frac{C_1}{C_2} = \infty$).

We note that with the normalization described in Sect. 5.3, we have assumed that the magnitude of the total scattering time *does not change* with the addition of a second scattering term. Physically, the addition of a second scattering mechanism should decrease the total scattering time. Preliminary calculations were done to determine whether or not an improvement in the power factor may still be possible, despite the expected decrease in τ. We calculated the transport properties of bulk systems in which the scattering time of the dominant scattering mechanism is given by $\tau(E) \sim \left(\frac{E}{k_B T}\right)^{-0.5}$, and investigate the effect of introducing a second scattering mechanism $\tau(E) \sim \left(\frac{E}{k_B T}\right)^{1.4}$. Experimentally, this second energy-dependent scattering ($p \gg 0$, frequently referred to as "energy-filtering" [65, 66]) can be achieved through the introduction of grain boundaries, which preferentially scatter low-energy (cold) electrons over high-energy (hot) electrons. Increases in the power factor via "energy-

filtering" have been demonstrated in InGaAs/InGaAlAs superlattices[67] and Pb/PbTe nanocomposites[68].

The total scattering rate then has the form

$$\tau(E)^{-1} = \left(\left(\frac{E}{k_BT}\right)^{-0.5}\right)^{-1} + \frac{1}{C}\left(\left(\frac{E}{k_BT}\right)^{1.4}\right)^{-1} \tag{5.9}$$

where the coefficient C determines the magnitude of the second scattering time (p=1.4) relative to the first (p=-0.5). The scattering times for several values of C are given as a function of electron energy in Figure 5.5(a). In general, the total scattering time for two scattering mechanisms is lower than that of a single scattering mechanism.

Bulk power factor calculations, normalized by the optimal power factor value calculated for the "original system" (a single scattering term with p=-0.5), are shown
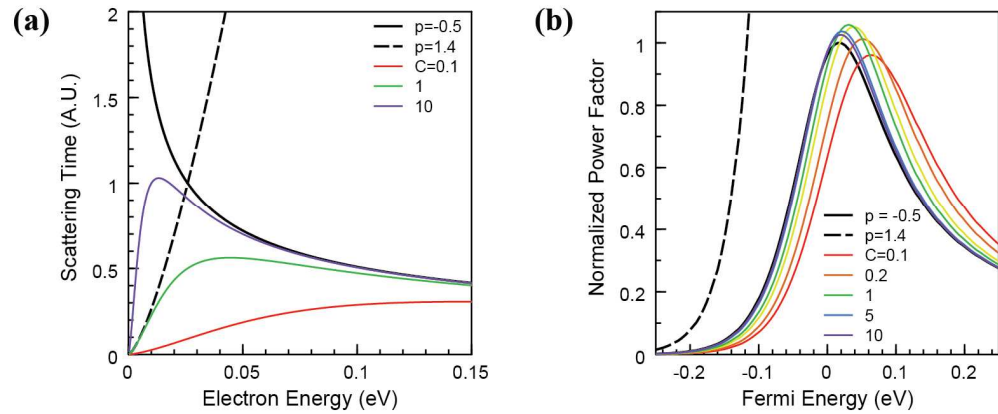
Figure 5.5: (a) Scattering times as a function of electron energy for various values of C. (b) Bulk power factor values, normalized by the maximum value for a single scattering mechanism with p=-0.5, as a function of Fermi energy for various values of C.

as a function of Fermi energy in Figure 5.5(b). Despite the decrease in the scattering time (Figure 5.5(a)), the addition of a second scattering term can lead to as high as a 6% increase in the maximum bulk power factor value. We note that these are preliminary calculations, and a more thorough theoretical investigation is necessary to determine the optimal functional form of the second scattering mechanism.[5, 69]

5.5 Size-Dependence of the Scattering Time

With the model presented in this chapter, we have assumed no explicit *size-dependence* of the scattering time. For the analysis here we have assumed a single scattering model applies for each *PF(a)* curve. This approximation means that for the systems investigated here, the dominant scattering mechanism does not change with size. Further, $\langle\tau\rangle$ is set to τ_{CRTA} regardless of size. As nanostructure size is varied, the characteristics of the scattering time may be affected through (i) changes in the electronic subband structure, (ii) changes in the phonon dispersion relations, (iii) interface effects (ex: boundary scattering) and (iv) changes in the optimal Fermi energy, and therefore the carrier and impurity concentrations. Literature indicates that there is a critical size at which these modifications become significant and large deviations from bulk are observed. Theoretical and experimental work, which includes a wide range of thin film[35, 70-73] and nanowire [4, 35, 74-78] material systems, suggests that this critical size is smaller than 20 nm.

For systems larger than 20nm, which includes the majority of structures discussed here, a detailed investigation of the relevant scattering mechanisms is expected to yield at most a 20% variation in the magnitude of the power factor.[35] For systems below 20nm, however, the approach to $\tau(E)$ taken here is not reliable.

The trends observed for these highly confined systems should be revisited through the investigation of specific materials and their size-dependent scattering rates.

5.6 Summary

In this chapter, we investigated the size-dependence of the thermoelectric power factor of systems for which the scattering time is a function of carrier energy. We find that the power factor of nanostructures exhibits the same qualitative behavior as a function of size, regardless of the particular scattering model. For each scattering model, whether the scattering time increases, decreases or exhibits a maximum as a function of carrier energy, the power factor has a non-monotonic dependence on film thickness and nanowire radius (see [63]). In addition, independent of $\tau(E)$, the power factor of thin films (nanowires) falls below the bulk value for all thicknesses larger than 20nm (radii larger than 12nm).

We find that for each thickness, the power factor of thin films increases monotonically with the scattering parameter p. This is the result of the increasing contribution of high energy electrons, pushing the optimal Fermi energy far into the band. In addition, we report that for weakly confined films (with thicknesses larger than 31nm), the ratio $\frac{PF_{2D}}{PF_{3D}}$ also increases with p. The decrease in the power factor when moving from bulk to thin films is therefore less significant in systems characterized by large p values.

Finally, we discussed the potential for introducing an additional scattering mechanism with a preferable energy dependence ($p \gg 0$) as a potential means for increasing the thermoelectric power factor. Our preliminary results indicate that such an improvement is possible despite a calculated decrease in the magnitude of the

100

scattering time. Future modeling work should therefore focus on determining optimized conditions for which even higher power factor improvements can be realized.

Chapter 6 Novel Instrumentation for Fabrication and Characterization of Thermoelectric Thin Films

6.1 Introduction

In this chapter, we present tools and methods we developed for the fabrication and characterization of thermoelectric thin films. We start by introducing pulsed laser deposition as an attractive technique for fabricating thin film thermoelectric materials. The design and set-up of a unique dual pulsed laser deposition (PLD) and thermal evaporation (TE) system is then described. This system was custom designed and built for our group in 2012 by Blue Wave Semiconductors, with the help of a former postdoctoral student Dr. Hasina Ali. The PLD-TE system can accommodate multiple targets for PLD and multiple boats for thermal evaporation and is ideal for the fabrication and doping of simple thin films as well as synthesis of more complex multi-layer structures.

Experimental techniques were also developed for measurement of the room temperature thermoelectric transport properties (Seebeck coefficient and sheet resistance) of thin films. Both measurements are done using an in-house probe station, allowing for quick turn-around in characterizing the thin films. The set-up for measurement of the Seebeck coefficient, designed to be entirely self-contained, allows for rapid switching between Seebeck and resistance measurements and between different samples.

Pulsed Laser Deposition of Thin Films

The transport properties of thermoelectric materials are strongly dependent on composition and stoichiometry—slight changes in the carrier concentration can lead to substantial deviations from the optimal thermoelectric power factor and *ZT* values. Pulsed laser deposition, described below, is therefore an ideal technique for the deposition of thin films for thermoelectric application.[9, 79, 80]

Pulsed laser deposition, a physical vapor deposition process done in a vacuum system, is particularly attractive when compared with other deposition techniques in that it is easy to implement and can be used to deposit a wide range of thin film structures, including complex oxides, epitaxial films and superlattices and polymer
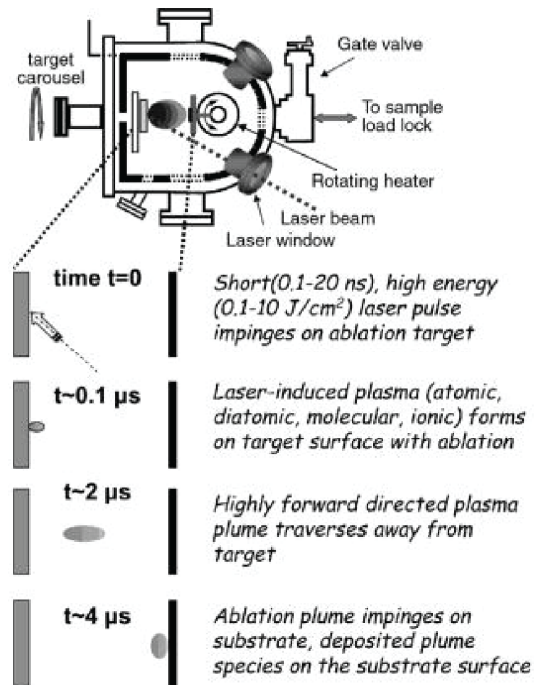
Figure 6.1: Schematic of pulsed laser deposition from [1]. A pulsed laser beam is focused onto a target inside a vacuum chamber. Each pulse of the laser creates a directional plasma, which condenses on the surface of the substrate.

films.[1] A schematic of a PLD system and the processes that occur during deposition are shown in Figure 6.1. A laser is focused on a target inside of the deposition chamber. For each pulse of the laser, a small amount of target material is vaporized creating a plasma plume. The highly-directional plume is discharged from the target towards the substrate. In this way, a thin film is grown on the substrate with many pulses of the laser.

One of the most important advantages of PLD over other deposition methods is the ability to deposit a multiple-component film from a single target with excellent transfer of stoichiometry. This is because, for an appropriate choice of laser wavelength and power, the energy absorbed by the target with each laser pulse is greater than the energy required for evaporation of each of the target elements. Thus (under optimized conditions) vaporization and deposition of the target material occurs independent of the vapor pressures of the target elements.

Pulsed laser deposition, though easy to implement, is a complicated process. In addition to the laser wavelength and power, a film deposited using PLD is affected by many factors including the pressure inside the deposition chamber, chemistry of the background gas, temperature of the substrate, choice of substrate and the distance between the target and the substrate. In general, the rate of deposition decreases with increasing background pressure and increasing distance between the target and the substrate. The background gas can be chosen either to participate in the deposition process (e.g. flow of O_2 in the deposition of an oxide[81]) or simply to control the kinetic energy of the plasma plume. High substrate temperatures may be necessary in

order to promote grain growth in the film, but can lead to re-evaporation of elements with high vapor pressures.

6.3 Dual Pulsed Laser Deposition-Thermal Evaporation System

6.3.1 Introduction

As described above, PLD is an ideal technique for the deposition of thin films for thermoelectric application. Thermal evaporation, a process by which a source material is heated to evaporation in vacuum, can be used in a variety of ways to contribute to the fabrication and characterization process. For example, co-deposition by thermal evaporation during PLD can lead to better control over the stoichiometry
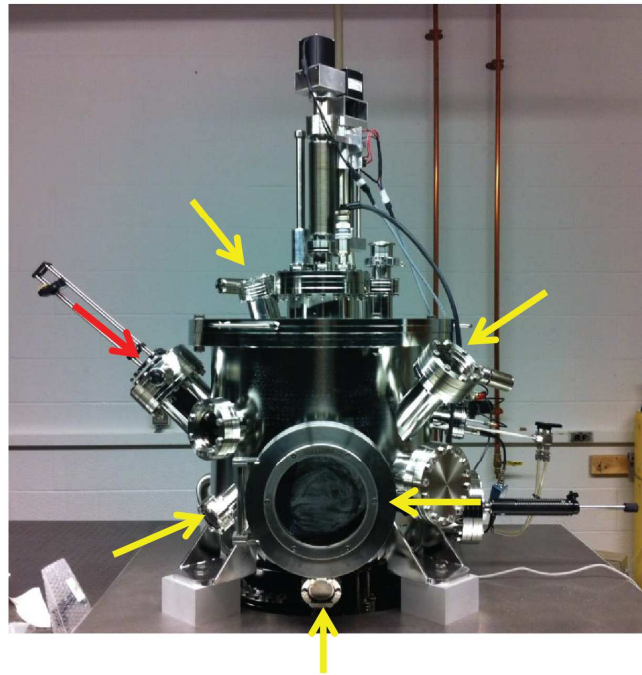
Figure 6.2: Photograph of the PLD-TE chamber. Arrows mark quartz windows and the front door to the chamber. For PLD, the laser enters the chamber through the window marked by the red arrow.

in the deposited films. Further, thermal evaporation can be used to deposit patterned metal contacts for a range of transport property measurements. The dual PLD-TE system described here therefore allows us to perform multiple processes (either simultaneously or successively) without having to remove the thin film samples from vacuum.

We note that by designing a chamber to accommodate both deposition techniques, it becomes difficult to optimize each process individually. For example, the typical separation between substrate and target for pulsed laser deposition is ~4cm, while the substrate is at a much greater distance from the source during thermal evaporation. A chamber designed for both techniques must then allow for movement of the substrate. Further, there is a question of how the substrate should be oriented relative to thermal evaporation and PLD sources. In our system, the substrate holder is not centered with either the PLD target or the thermal evaporation boats. This is a compromise for the two techniques, and it is not ideally positioned for either deposition method. Further, while one can install shutters to cover the boats during PLD and protect the targets during thermal evaporation, cross-contamination of the sources may be an issue during either process. The chamber described below was designed with these issues in mind, and engineering solutions were developed to minimize their effects.

An Appendix at the end of this thesis includes a description of the integrated front panel of the PLD-TE system, a list of the main components with part numbers, and CAD drawings of several of the components designed by Blue Wave Semiconductors.

6.3.2 Chamber Design

A photograph of the dual PLD-TE system is shown in Figure 6.2 (a CAD drawing of the chamber is given in the Appendix as Figure 10.2). The ~1 m^3 chamber is evacuated to ~10^{-3} Torr with a Pfeiffer DUO035 Roughing Pump. High vacuum (<10^{-6} Torr) is achieved with a Pfeiffer HiPace 400 Pump, the spinning speed of which is controlled by an integrated TC400 Drive Electronics system. A gate valve separates the main deposition chamber from the pumping stack and is open when the chamber is in use. The pressure is measured using a Pfeiffer PKR251 Compact FullRange Gauge, which contains both a cold cathode and a Pirani gauge for pressure ranges of 10^{-9}-10^{-4} Torr and 10^{-4}-10^2 Torr, respectively. The pressure is controlled manually using the turbo pump, the rouging pump and N_2 gas flow controlled using an MKS Mass Flow Controller and 167 Readout/Set Point Module. Pressures between 10^{-3} Torr and 2 Torr are obtained with the turbo pump off, the roughing
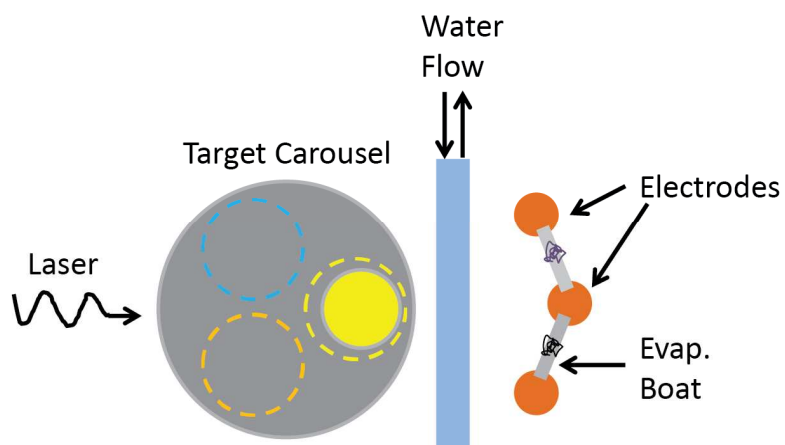
Figure 6.3: Aerial schematic of the bottom of the deposition chamber.

pump on and a gas load between 1 and 100 sccm (standard cubic cm per min). For pressures between 10^{-6} Torr and 10^{-3} Torr, the turbo pump is set to "standby mode" (a reduced spinning speed) and gas is flowed between 1 and 40 sccm.

All deposition materials and substrates are put into the chamber via the quick-access port in the front (the "front door" at the center of Figure 6.2). The target carousel for PLD and the electrodes for TE are shown in an aerial schematic of the bottom of the chamber in Figure 6.3. The target carousel can accommodate 3 targets with a maximum diameter of 5cm. The targets are mounted onto holders (either with clips or with Ag paint) for ease of transfer to and from the carousel. A stainless steel cover (shown in gray) exposes a single target at a time. The target carousel is rotated to switch between targets using a Silverpak 23C Integrated Step-Motor and control/drive unit. A second motor is used to rotate the individual targets during PLD. Both motors are controlled using a LabView program.

The electrodes for thermal evaporation are on the righthand side of the chamber and are separated from the target carousel by a water-cooled block (see CAD drawing in Appendix, Figure 10.5). The chamber can accommodate two ~1cm x 10cm evaporation boats which are attached to water-cooled molybdenum discs on top of the copper electrodes (see CAD drawing in the Appendix, Figure 10.4). An INFICON SQC-310 Thin Film Deposition Controller connected to a Sorensen DCS8-350E DC Power Supply is used to control the deposition rate and final thickness of the films deposited. The deposition controller uses a proportional integral derivative (PID) control loop based on feedback from a quartz crystal sensor inside the chamber. Evaporation is done by powering one boat at one time; a toggle connected to a solid
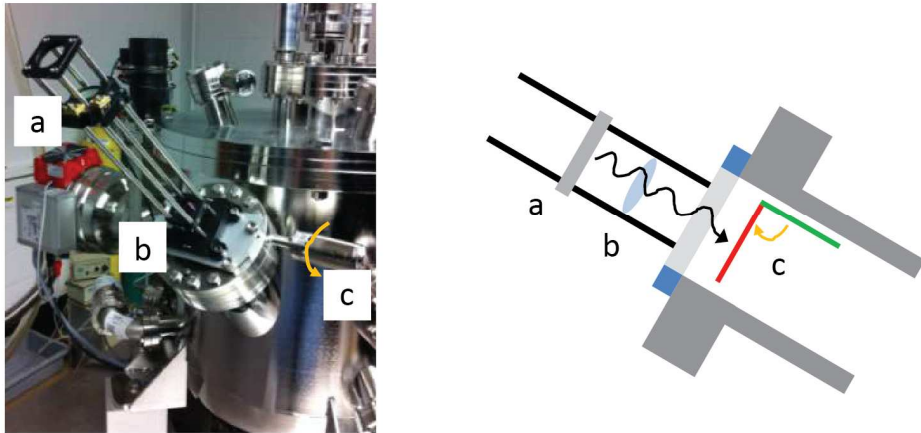
Figure 6.4: Photograph and schematic of the cage mount attached to the chamber for PLD. (a) Mirror, (b) lens and (c) shutter for quartz window.

state relay is used to select the active pair of electrodes. Two shutters are used to cover the substrate and the boats.

Pulsed laser deposition is done using a 532nm Nd:YAG Quantel Brilliant b laser. The laser beam is routed by a set of high damage-threshold mirrors and focused into the chamber with a lens on a cage mount (see Figure 6.4). A manual shutter protects the inner surface of the window during thermal evaporation processes.

6.3.3 Substrate Holder

Substrates up to 2" in diameter are mounted onto the sample holder (see CAD drawing in Appendix, Figure 10.3) using clips or Ag paint. The holder is then screwed into an upside-down chuck inside of the chamber (Figure 6.5). Using controls (Substrate Position and Substrate Rotation) on the front panel, the chuck can be moved up and down within the chamber, as well as rotated. A mask holder can be positioned over the substrate for patterned depositions.
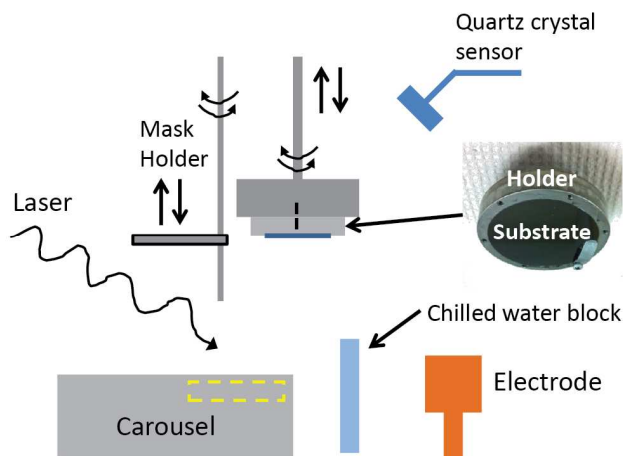
Figure 6.5: Schematic of arrangement of the components inside the deposition chamber, viewed from the front.

Unlike thermal evaporation, PLD is a highly directional deposition method. During thermal evaporation, the sample holder is typically rotated for uniform deposition over the entire substrate. For PLD, on the other hand, the thickest films are achieved without rotation by placing the substrate at an optimal position relative to the target. This optimal position was identified as follows: a 4" Si wafer was placed onto the substrate holder and the rotational position of the holder was marked by two reference scratches on the holder and the chuck (see schematic in Figure 6.6). A film was deposited onto the substrate by PLD using conditions that yield a colorful oxide. The radial color gradient of the oxide was then used to visually determine the thickest part of the deposited film. Scratches were then made on the substrate holder to mark this optimal position. Once the substrate is placed at the optimal position and the substrate holder is screwed into the chuck, the holder is rotated to the correct rotational position (the reference marks on the chuck and the holder are aligned).
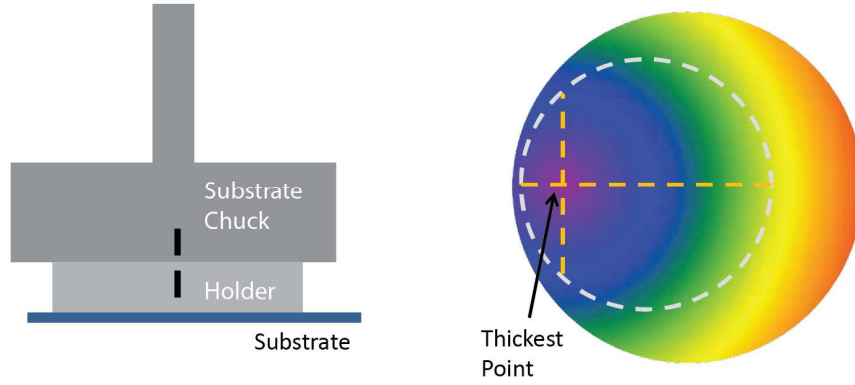
Figure 6.6: Schematics of the method used to identify the optimal position for PLD in cross-section (left) and from the top surface (right). Reference marks on the substrate chuck and holder are indicated in cross-section. The colorful thickness gradient, and the scratches on the substrate holder (dashed orange lines) are shown from the top.

The temperature of the substrate is monitored and controlled with a Eurotherm 2416 Controller/Programmer connected to a heater and a thermocouple inside the substrate chuck. Due to the spatial separation between the thermocouple (inside of the chuck) and the substrate (on the surface of the holder), the thermocouple temperature may be different from the substrate temperature. The true temperature at the surface of the holder was measured at a pressure of 10^{-6} Torr using an infrared thermometer for temperatures between 550 and 650 C. The calibration curve from this measurement is in Figure 6.7. For temperatures above 250 C, the true temperature T_{meas} can be estimated from the display temperature T_{disp} using the following regression line:

$$T_{meas} = 0.68 \cdot T_{disp} + 83°C. \tag{6.1}$$

For temperatures below 250 C, the true temperature of the substrate is taken to be equal to the display temperature. We also note that during thermal evaporation, the
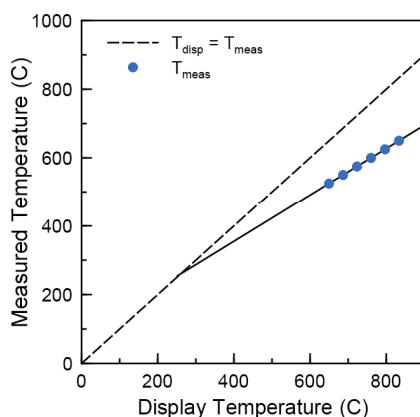
Figure 6.7: True temperature (blue dots) measured using an infrared thermometer as a function of the Eurotherm display temperature. The solid black line is a regression line calculated from the measured data.

heat generated by the boats may increase the temperature of the substrate. In this case, the display temperature (measured inside of the substrate chuck) is expected to be *lower* than the temperature of the substrate. The substrate temperatures most commonly used for PLD of $Bi_{2-x}Sb_xTe_3$ are 375 C and 390 C, and are achieved by setting the display temperature to 430 C and 450 C, respectively.

6.3.4 User Interface

A LabView program (Figure 6.8) was written to record pressure and temperature data as a function of time during the operation of the system. The pressure values are read from the Pfeiffer PKR251 Single Gauge Control Unit, and temperatures are read from the Eurotherm 2416 Controller. An additional Comment input is included and saved as a function of time so that the user can record events with a time-stamp (e.g. "1820 sec: Start of deposition"). The data recorded with this computer interface helps to elucidate trends in deposition conditions that are not immediately apparent in real-
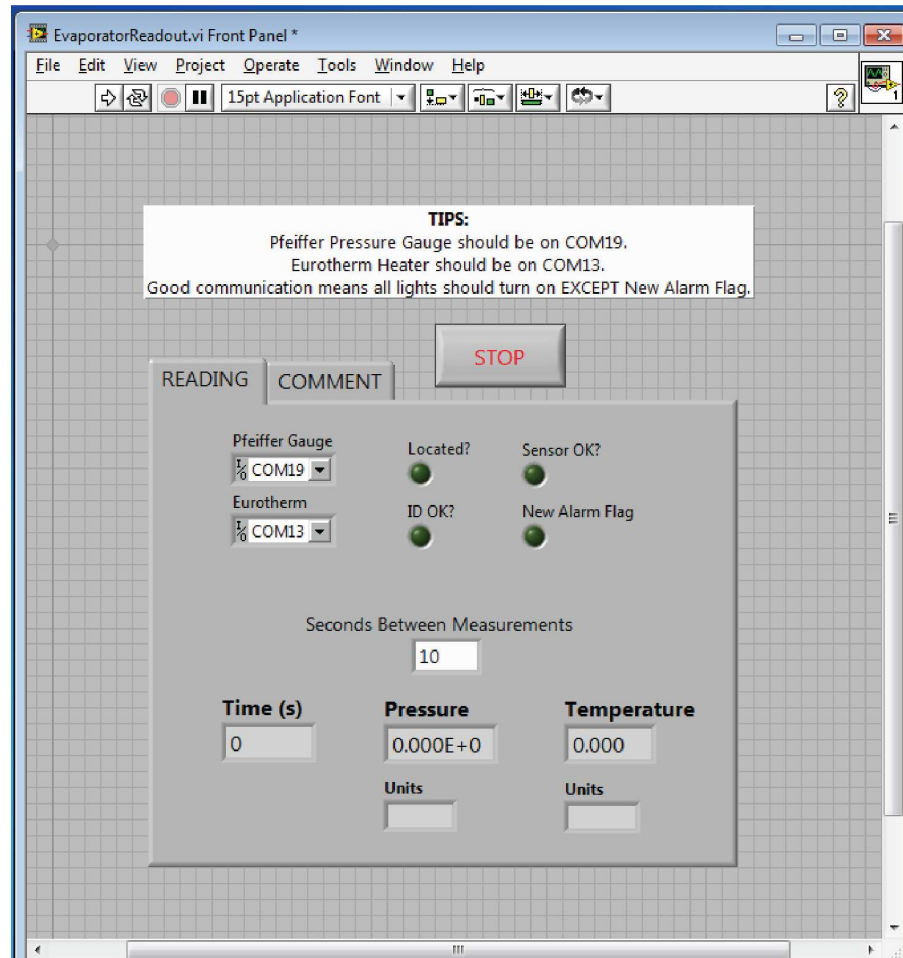
Figure 6.8: User interface of Labview program for recording real-time pressure and temperature data.

time. In addition, it allows us to consistently keep track of the "health" of the chamber (pump-down time, base pressure, etc.).

6.4 *Experimental Set-up for Measurement of Thin Film Transport Properties*

6.4.1 Seebeck Coefficient

The Seebeck coefficient is measured using a "two-thermocouple" method described in [82]. A schematic of this method is shown in Figure 6.9. The typical sample is a
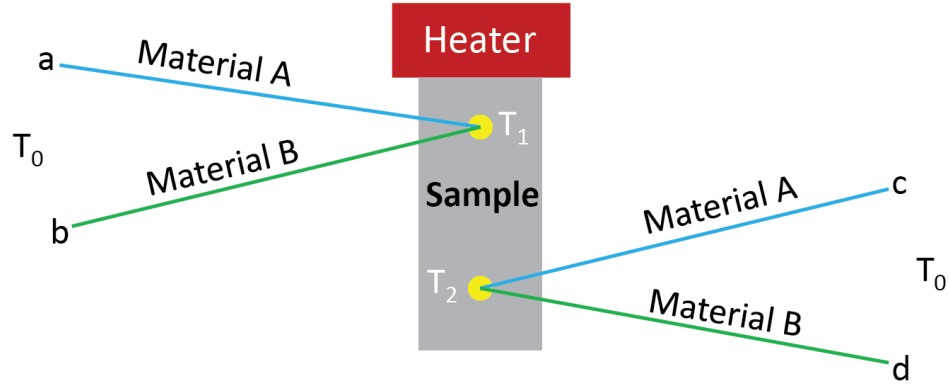
Figure 6.9: Schematic of the "two-thermocouple" method for measurement of the Seebeck coefficient. Thermocouple junctions make electrical and thermal contact with the sample at points with different temperatures. Thermocouple leads are kept at room temperature.

thin film (~100nm) on a Si substrate. A heater is positioned in contact with one end of the sample, and two identical thermocouples with known leg materials A and B are placed on top of the hot and cold ends of the film. With applied heat, a temperature gradient is established and Seebeck voltages are created in the leads of the thermocouples as well as in the sample. Commonly, the voltages $V_{ab} = V_a - V_b$ and $V_{cd} = V_c - V_d$ are measured to deduce the temperature differences $T_1 - T_0$ and $T_2 - T_0$ via:

$$V_{ab} = -S_{AB}(T_1 - T_0) \tag{6.2}$$

$$V_{cd} = -S_{AB}(T_2 - T_0)$$

where $S_{AB} = S_A - S_B$ is the Seebeck coefficient of the thermocouple. Alternatively, the voltages V_{ac} and V_{bd} can be measured

$$V_{ac} = -S_A(T_1 - T_0) - S_{sample}(T_1 - T_2) - S_A(T_2 - T_0) \tag{6.3}$$

$$V_{bd} = -S_B(T_1 - T_0) - S_{sample}(T_1 - T_2) - S_B(T_2 - T_0)$$

and can be used to derive the Seebeck coefficient of the sample S_{sample} and the temperature drop $T_1 - T_2$:

$$S_{sample} = \frac{V_{bd}S_A - V_{ac}S_B}{V_{bd} - V_{ac}} = \frac{V_{ac}}{V_{bd} - V_{ac}}S_{AB} + S_A \qquad (6.4)$$

$$T_1 - T_2 = \frac{V_{ac}}{S_A - S_{sample}}.$$

We can therefore calculate the Seebeck coefficient of the sample with these voltage measurements and with knowledge of the Seebeck coefficient of one of the thermocouple leads (Eq. (6.4) is written in terms of S_A). We have assumed in this derivation that the temperature of the thermocouple is exactly equal to the temperature of the sample at the points of contact (i.e. there is good thermal contact between the thermocouples and the sample).

The set-up used in our lab is shown in Figure 6.10. The measurement is done on a plexi-glass stage; the underside of this stage was machined to fit securely on top of a chuck inside the Signatone S1160 probe station. A temperature gradient is generated by passing current (up to 40mA) through the 1k-ohm flat resistor screwed into the plexi-glass. Good thermal contact between the heater and the sample is ensured by placing a continuous piece of Al foil under both, and positioning the sample flush with the edge of the heater.

The thermocouples typically used are 0.005"-thick foil Type E thermocouples (Omega Engineering). The leg materials of Type E thermocouples are chromel (a Ni-Cr alloy) and constantan (a Cu-Ni alloy), and the room temperature Seebeck coefficients of these materials are S_{NiCr}=22.4 μV/K and S_{CuNi}=-38.1 μV/K. These Seebeck coefficients are determined from known values for the Seebeck coefficients

115

for Cu (1.94 μV/K) [83], Type T (Cu and Cu-Ni leads, 40.08 μV/K) and Type E thermocouples (60.5 μV/K, from the Omega Catalog), and were verified using our measurement set-up. The thermocouple near the heater is attached to a spring-loaded lever, and is pressed against the sample for good contact. A large magnet pad (see Figure 6.10) is placed underneath the sample so that the second thermocouple can be sandwiched between a small magnet and the sample. Good contact with the substrate is required for the measurement of the Seebeck coefficient: We find that a 2-point resistance less than 20k-ohms between the thermocouples is required for a stable measurement. If good contact could not be achieved with this set-up, a low-Seebeck metal solder (ex: Ag paste) was used to attach the thermocouples to the film.
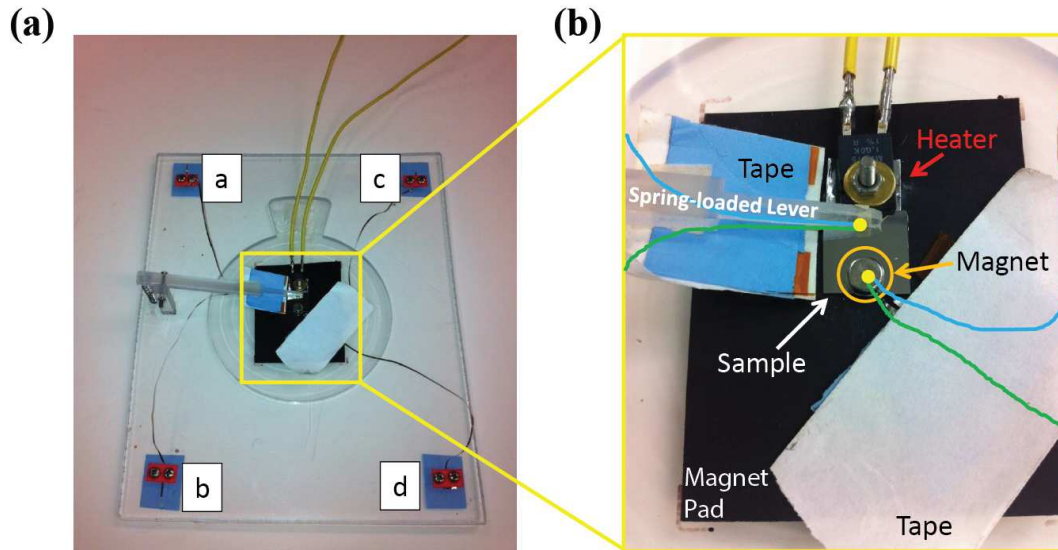
Figure 6.10: Set-up for measurement of the Seebeck coefficient of thin films. (a) Low magnification photograph showing the leads. The letters in the image correspond to the letters in the schematic in Figure 6.9. (b) High magnification photograph of the sample, heater and thermocouple junctions. The thermocouple leads are marked by colored lines. The points of contact between the thermocouples and the sample (a square wafer) are marked by yellow dots.
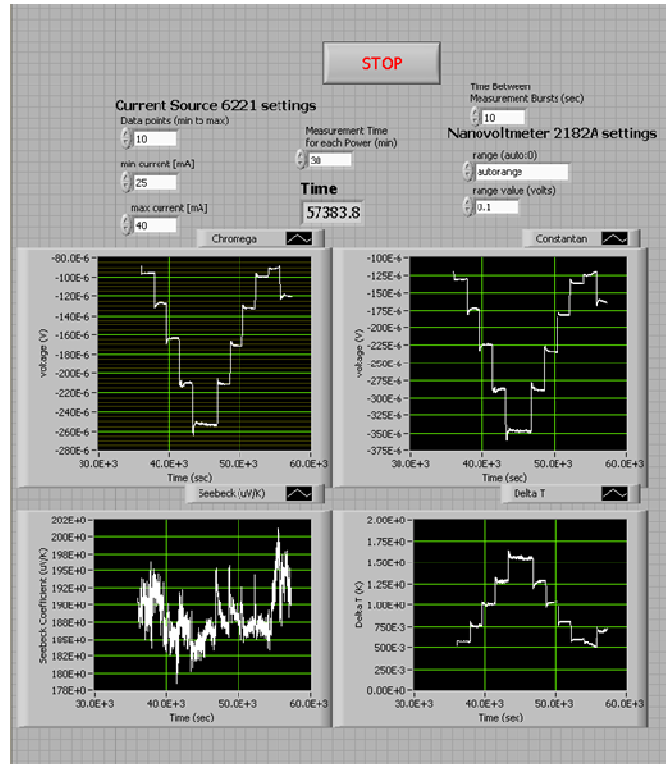
Figure 6.11: User interface of the LabView program for measurement of the Seebeck coefficient. The voltages V_{ac} and V_{bd} are plotted as a function of time in the top row; the measured Seebeck coefficient and temperature drop T_2-T_1 are shown in the bottom row.

Once inside the probe station, the voltages V_{ac} and V_{bd} are measured through the ends of the thermocouple leads at the corners of the plexi-glass stage (Figure 6.10). A LabView program was written to control the current from a Keithley 6221 Current Source sent to the heater and to collect measured voltages V_{ac} and V_{bd} from a 2-channel Keithley 2182A Nanovoltmeter in real time. For a typical measurement, the heater current is cycled between 10mA and 40mA at small intervals (for T_2-T_1 between ~0.5 and 3°C) 4 times. For each choice of heater current, the measurement takes between 20 and 30min to stabilize so a typical measurement takes 10 hours. To reduce noise, data points are averages over bursts of 10 rapid measurements. This

117
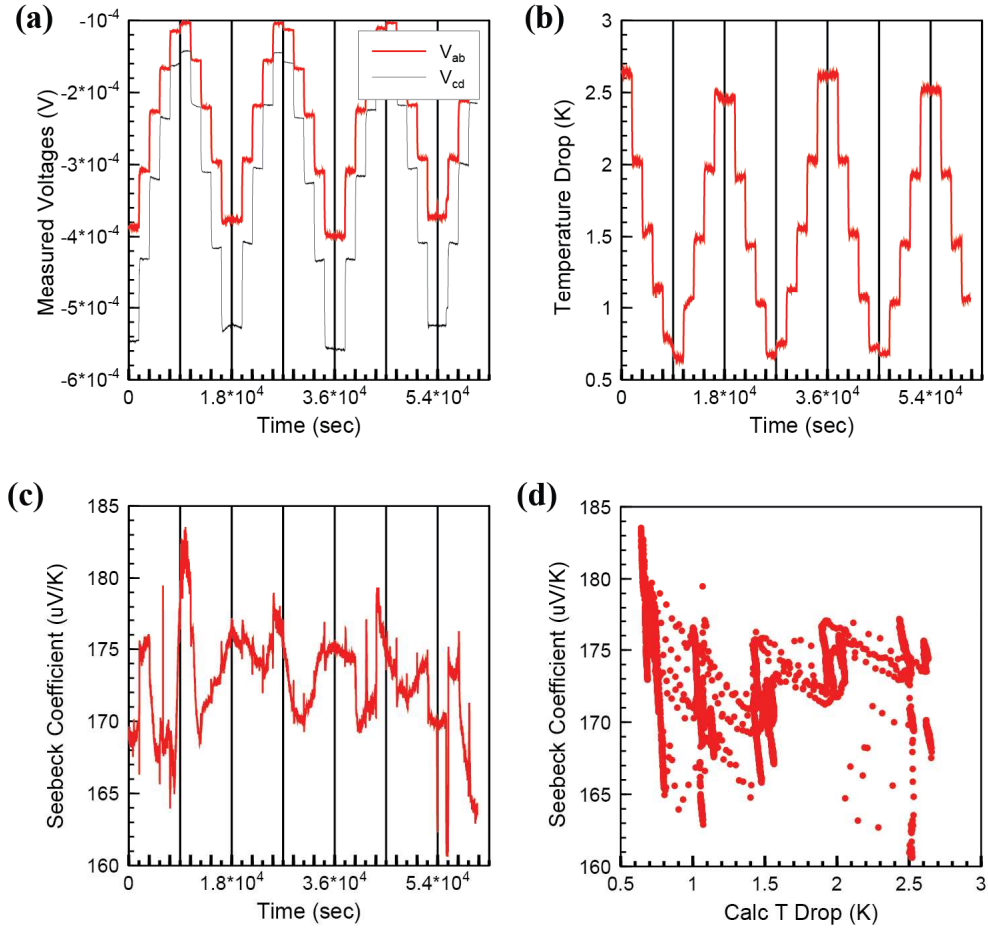
Figure 6.12: Example of data collected for a $Bi_{2-x}Sb_xTe_3$ thin film. (a) Voltages V_{ac} and V_{bd}, (b) temperature drop (calculated using Eq. (6.4)), and (c) the sample Seebeck coefficient (calculated using Eq. (6.4)) as a function of time during the measurement. Steps or jumps in the data indicate changes in the value of the heater current. (d) The Seebeck coefficient as a function of the temperature drop.

computer-controlled data acquisition allows us to monitor the stability of the measurement over time. An example of data collected during a measurement is shown in Figure 6.12.
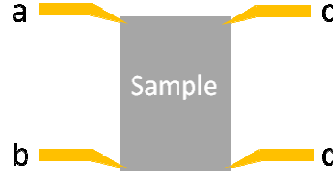
Figure 6.13: Schematic of set-up for Van der Pauw measurement.

6.4.2 Electrical Conductivity

The sheet resistance of the thin films is measured inside of the Signatone S1160 probe station by the van der Pauw method. A LabView program is used to automate the measurement using a Keithley 6221 current source and a Keithley 2182A nanovoltmeter. Typical samples are rectangular in shape and the four probes are placed at the corners (see Figure 6.13). Two separate measurements are done for each determination of the sheet resistance: (1) A range of currents is flowed between contacts a and b (I_{ab}) and voltage V_{cd} is measured and (2) a range of currents I_{ac} is applied while voltage V_{bd} is measured. The slopes of these measurements dV/dI give two resistances:

$$R_V \equiv \frac{dV_{ab}}{dI_{cd}} \tag{6.5}$$

$$R_H \equiv \frac{dV_{ac}}{dI_{bd}} \, . $$

The sheet resistance R_S can be calculated from R_V and R_H using the van der Pauw formula:[84]

$$e^{-\pi R_V / R_S} + e^{-\pi R_H / R_S} = 1 \tag{6.6}$$

An iterative Matlab program is used to solve Eq. (6.6). In the simple case of

$R_V = R_H = R$, $R_S = \dfrac{\pi R}{\ln(2)}$. The conductivity of the film is calculated as $\sigma = \dfrac{1}{\rho} = \dfrac{1}{R_S t}$

where t is the thickness of the film, determined by cross-sectional SEM.

6.5 *Summary*

In this chapter, we described the unique pulsed laser deposition, thermal evaporation chamber in our lab. The dual functionality of this system makes it ideal for depositing a wide range of thin film structures and devices. Specifically, PLD is a promising technique for deposition of thermoelectric materials, the properties of which depend strongly on stoichiometry. We also describe the in-house experimental set-up for measurement of the thermoelectric transport properties (Seebeck coefficient and sheet resistance), which allows for quick characterization of samples after deposition.

Chapter 7 Pulsed Laser Deposition of $Bi_{2-x}Sb_xTe_3$ Thin Films

7.1 Introduction

The $Bi_{2-x}Sb_xTe_3$ materials system is one of the best known room temperature p-type thermoelectric materials[85]. We investigate introducing nanoscale porosity in an effort to improve the thermoelectric power factor of $Bi_{2-x}Sb_xTe_3$ thin films. The porosity creates additional confinement within the thin film and can alter carrier scattering such that the Seebeck coefficient increases. This effort consisted of studying the pulsed laser deposition (PLD) conditions for $Bi_{2-x}Sb_xTe_3$ followed by an investigation of the effects of porosity in the deposited films.

In this chapter, we explore the characteristics of "dense" (non-porous) films deposited by PLD as a function of various deposition conditions. The effects of substrate temperature, background pressure and laser power on the pulsed laser deposited thin films were investigated. Subsequently, the effect of annealing on the properties of dense films was examined. Annealing is necessary in order to recover crystalline films; however, optimizing the annealing conditions (temperature, pressure, background gas chemistry) is necessary in order to prevent loss of highly volatile Te. Strategies for fabrication of porous thin films are given in Chapter 8.

7.2 Motivation

7.2.1 $Bi_{2-x}Sb_xTe_3$ Materials System

The excellent thermoelectric properties of $Bi_{2-x}Sb_xTe_3$ can be largely attributed to its complex crystal structure. Bi_2Te_3, Sb_2Te_3 and the alloy $Bi_{2-x}Sb_xTe_3$ are described by a rhombohedral unit cell, consisting of two Bi/Sb atoms and three Te atoms. More frequently, however, the structure is described by a hexagonal primitive cell with layers of metal and chalcogenide atoms along the [0001] direction. The hexagonal primitive cell consists of three quintets (5 layers each) (see Figure 7.1). Each quintet has the form Te(1)-Bi/Sb-Te(2)-Bi/Sb-Te(1). The Bi/Sb-Te bonds have mixed ionic and covalent character, while the Te(1)-Te(1) bonds between quintets are Van der Waals and are therefore much weaker. The room temperature hexagonal lattice parameters for Bi_2Te_3 and Sb_2Te_3 are given in Table V.

Table V. Hexagonal lattice parameters for Bi_2Te_3 and Sb_2Te_3 at 300K.[85]

Compound	a (nm)	c (nm)
Bi_2Te_3	0.43835	3.0360
Sb_2Te_3	0.4275	3.0490
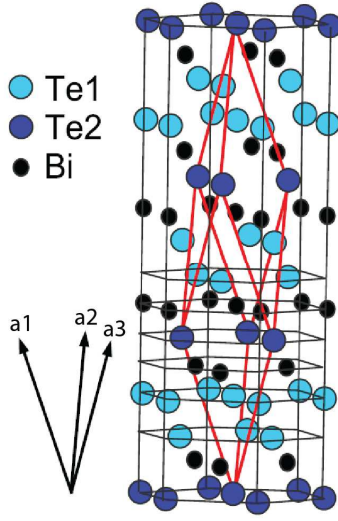
Figure 7.1: Hexagonal primitive cell of Bi_2Te_3. The rhombohedral unit cell is marked in red, with lattice vectors shown at the bottom left. Adapted from [16].

The lattice parameter a follows Vegard's law ($a_{alloy} = \frac{(2-x)}{2} \cdot a_{Bi_2Te_3} + \frac{x}{2} \cdot a_{Sb_2Te_3}$ where the alloy is assumed to be $Bi_{2-x}Sb_xTe_3$), decreasing as the alloy becomes more Sb-rich. The change in lattice parameter c with alloying is not well-documented, with some reports indicating almost no dependence on the Sb:Bi ratio[86, 87] and other reports indicating that c is actually lower for alloys than for either Bi_2Te_3 or Sb_2Te_{3}[88].

The high-symmetry rhombohedral crystal structure translates to a six-fold degeneracy of the valence and conduction bands.[39] This kind of high band degeneracy is beneficial to the thermoelectric power factor. The total electrical conductivity, the sum over the contribution of each of these degenerate bands (see the sum in Eq. (2.7)), increases by a factor of ~6 without negatively impacting the Seebeck coefficient. In addition to ideal electronic properties, the complex crystal

structure of the $Bi_{2-x}Sb_xTe_3$ materials system leads to low values of the thermal conductivity. In general, the thermal conductivity decreases with the number of atoms in the primitive unit cell.[89]

Reported literature values for the electrical and thermal conductivities and the Seebeck coefficient of p-type Bi_2Te_3, Sb_2Te_3 and $Bi_{0.5}Sb_{1.5}Te_3$ are given in Table VI. These values were measured in the hexagonal basal plane (perpendicular to the *c*-direction). The *ZT* value for Sb_2Te_3 is too low for practical application. Alloying with Bi_2Te_3 both increases the power factor and decreases the thermal conductivity. The increase in *ZT* value of the alloy over Bi_2Te_3 is largely due to a substantial decrease in the lattice thermal conductivity as the result of phonon scattering due to alloy disorder.

Table VI. Room temperature transport properties of Bi_2Te_3, Sb_2Te_3 and $Bi_{0.5}Sb_{1.5}Te_3$.

Compound	Electrical Conductivity (S/m)	Seebeck Coefficient (μV/K)	Thermal Conductivity (W/m-K)	*ZT*
Bi_2Te_3 [90]	1.0×10^5	190	2	0.54
Sb_2Te_3 [91]	4.7×10^5	79	5	0.18
$Bi_{0.5}Sb_{1.5}Te_3$ [92]	8.7×10^4	230	1.4	0.99

7.2.2 Review of Pulsed Laser Deposited $Bi_{2-x}Sb_xTe_3$ Thin Films

The first report of Bi_2Te_3 thin films deposited via pulsed laser deposition was published in 1996.[9] In this work, Dauscher *et al*. found that film composition

124
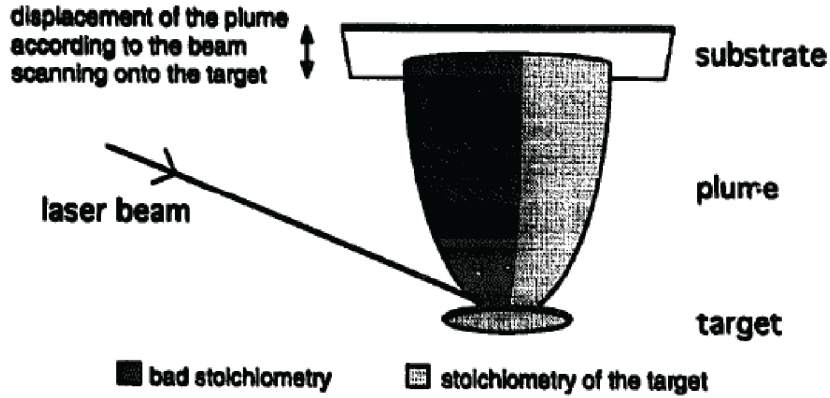
Figure 7.2: Schematic of the effect of substrate position on the stochiometry of the deposited Bi_2Te_3 film, from [9].

depends strongly on the position of the substrate relative to the target, even for room temperature depositions. The deposited film is Te-deficient at positions close to the incoming laser (see Figure 7.2), as the laser interacts with the plasma plume coming off the target.[9]   Since this original study, many groups have explored PLD as a means for depositing Bi_2Te_3-based thin films, and significant improvement has been achieved in terms of the properties of the deposited films. In 2007, Baillini *et al.* reported excellent control over the morphology of n-type Bi_2Te_3 films by varying the background Ar pressure and the substrate temperature.[93] The deposited films vary from disordered and nanocrystalline (room temperature) to highly-textured (high temperature, high pressure). The highest in-plane power factor values reported by this group ($\sim$2-5x10^{-3} W/m-K^2 at room temperature) are found for textured films deposited at 10 Pa and temperatures between 250 and 350°C (see Figure 7.3).[15]

(a)

(b)
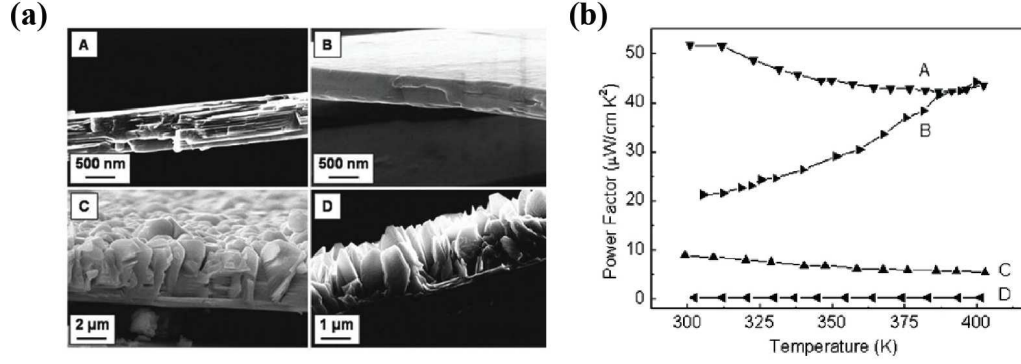
Figure 7.3: (a) Cross-sectional SEM images of Bi_2Te_3 thin films deposited by PLD at 4 different sets of conditions. (b) Power factor values as a function of temperature measured for the films on the left. From [15].

In 2003, Makala *et al.* reported the first successful pulsed laser deposition of $Bi_{2-x}Sb_xTe_3$ thin films. They found extremely low thermal conductivities (0.3-0.4W/m-K) in films deposited from an *x*=1.5 alloy target onto both mica and AlN/Si(100) substrates. However, high defect densities and issues with controlling stoichiometry (due to the high vapor pressure of Te) led to low conductivity values and low room temperature *ZT* values (0.05-0.08).[94] Obara *et al.* later demonstrated *x*=1.7 alloy films with high room temperature power factor values ($3.7x10^{-3}$ W/m-K), attributed to good control over stoichiometry.[80]

These results indicate that while PLD is a promising technique for deposition of $Bi_{2-x}Sb_xTe_3$ thin films, preventing loss of Te during deposition and annealing is crucial to achieve transport properties comparable with bulk.

7.3 Experimental Methods

In this section, we describe the general procedure used to deposit and characterize $Bi_{2-x}Sb_xTe_3$ thin films.

7.3.1 Deposition

$Bi_{2-x}Sb_xTe_3$ films were grown by PLD in the deposition system described in Sect. 6.3. For dense films, the typical substrate is 20-30 ohm-cm resistivity <100> Si with the native oxide intact. In general, the substrates are ~15x30 mm^2 in size, and are placed at the optimal position on the substrate holder to yield the thickest films (using the positioning procedure described in Sect. 6.3.3). The chamber was evacuated to a base pressure of ~10^{-6} Torr prior to deposition; for deposition, N_2 was flowed to achieve background pressures between $2x10^{-3}$ and 2 Torr. The substrate temperature was varied between 25 and ~375 C (note that the latter temperature is estimated from the calibration curve in Sect. 6.3.3). The Nd:YAG laser ($\lambda = 532$nm, repetition rate of 10Hz) was focused onto a rotating $Bi_{0.5}Sb_{1.5}Te_3$ target (purchased from American Elements, Merelex Corp.) with an average power between 0.6 and 3.6W (energy
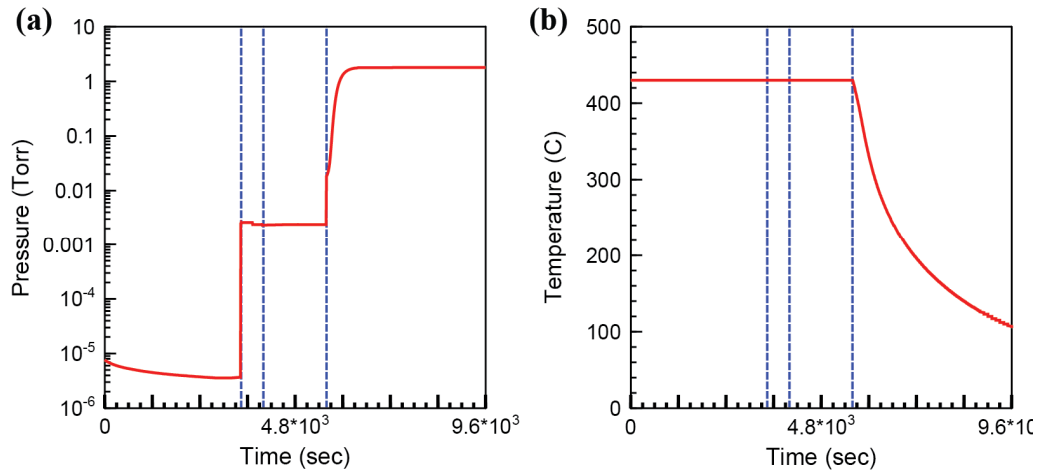
Figure 7.4: Example of the recorded (a) pressure and (b) temperature as a function of time before, during and after a deposition. The dashed vertical lines mark the flow of N_2 (yielding a pressure of 2mTorr), the start of the deposition and the end of the deposition. The deposition (26min long) was done at 2mTorr and a substrate temperature of 375 C (nominal temperature 430 C).

densities between 3 and 18 J/cm^2). Prior to deposition, the target is cleaned (with the substrate covered by a shutter) by ablating for ~1min at the desired laser power. A typical deposition is 26min long; with the substrate ~4cm from the target, the deposited films are 100-250nm thick giving a deposition rate between 0.06 and 0.15 nm/sec. An example of the pressure and temperature before, during and after a typical deposition (recorded using the LabView program described in Sect. 6.3.4) is given in Figure 7.4.

7.3.2 Characterization

The morphology of the deposited films was determined using a Hitachi SU-70 Analytical Scanning Electron Microscope (SEM) operated at 10kV. The crystal structure of the thin films was characterized by x-ray diffraction (XRD) using a Bruker D8 Advance system (Cu K$_\alpha$ radiation). 2θ values between 15 and 65° were scanned with a rate of 0.7°/min.

Preliminary analysis of the film composition was done using a Bruker Energy-Dispersive X-ray Detector attached to the SEM. However, due to errors in the measurement of small amounts of Bi and Sb on Si substrates (detailed below), more accurate measurements of the composition of dense films were done using a Perkin-Elmer 4300 Inductively Coupled Plasma Optical Emissions Spectrometer (ICP-OES). Calibration standards for Bi, Sb and Te were made by dissolving bismuth citrate ($C_6H_5BiO_7$), antimony oxide (Sb_2O_3) and tellurium oxide (TeO_2) (all purchased from Alfa Aesar) in an aqueous 10% wt nitric acid, 1.5% wt tartaric acid solution. Standards of 100-1000ppb (μg/L) were made for each element. Samples (~3x3mm^2 pieces of the deposited films on Si) were digested in ~1mL of 70% wt nitric acid.

Once completely dissolved (after ~1 hour), amounts of tartaric acid and deionized water were added to match the matrix solution. With this procedure, the typical sample solution has Bi, Sb and Te concentrations close to 200-400ppb, 200-500ppb and 600-1000ppb, respectively. The conditions for the ICP-OES measurement are listed in Table VII. The coefficient of determination for the calibration curves is generally $r^2 > 0.9995$.

Table VII. Typical conditions for ICP-OES measurement.

Parameter	Setting	Units
Power	1300	W
Auxiliary gas flow	0.2	L/min
Nebulizer gas flow	0.8	L/min
Sample uptake	1.5	mL/min
Time per measurement	10	sec
# of Repetitions	3	N.A.
Bi peak wavelength	223.061	nm
Sb peak wavelength	206.836	nm
Te peak wavelength	214.281	nm

The atomic concentrations are then calculated using the atomic weights of each element (see example in Table VIII). The film composition is then analyzed by looking at the ratios of the elements (for the example in Table VIII, Bi:Te=0.27, Sb:Te=0.84, (Bi+Sb):Te=1.1 and Sb:Bi=3.1).

Table VIII. Example of the calculated concentrations of Bi, Sb and Te of a dissolved film.

	Bi	Sb	Te
Weight Concentration (ppb)	450	800	1000
Atomic Wt (g/mol)	209.0	121.8	127.6
Atomic Concentration (nM)	2.15	6.57	7.84

Based on measurement of standard solutions with similar concentrations, we estimate the average error in the measurement of each element to be <5%.

The room temperature transport properties of the films (sheet resistance and Seebeck coefficient) were measured using methods described in Sect. 6.4. The conductivity values were then calculated using film thicknesses measured by cross-sectional SEM. For most PLD runs, we find that the film thickness varies by ~10% over the entire substrate.

7.4 *Effect of Deposition Conditions*

We first present an analysis of the effect of deposition conditions (substrate temperature, background pressure and laser power) on the properties of the $Bi_{2-x}Sb_xTe_3$ thin films. This investigation was done for depositions on <100> Si substrates. With the range of process parameters described in Sect. 7.3.1, the deposited films range between insulating and highly conducting, and between amorphous and crystalline. We note that much can be estimated from the appearance of the films: conducting films are silver in color, while insulating films are either

colorful (when amorphous) or matte gray (when a mixture of crystallites of Bi-rich and Sb-rich phases).

7.4.1 Effect of Substrate Temperature

We begin by discussing the effect of substrate temperature on the deposited films. SEM images of films deposited with a laser power of 0.6W at 90mTorr for substrate temperatures between 25° and 375°C are shown in Figure 7.5. In general, we see sintering and growth of grains in the as-deposited films as the substrate temperature increases. For a substrate temperature of less than 375°C, XRD results indicate that
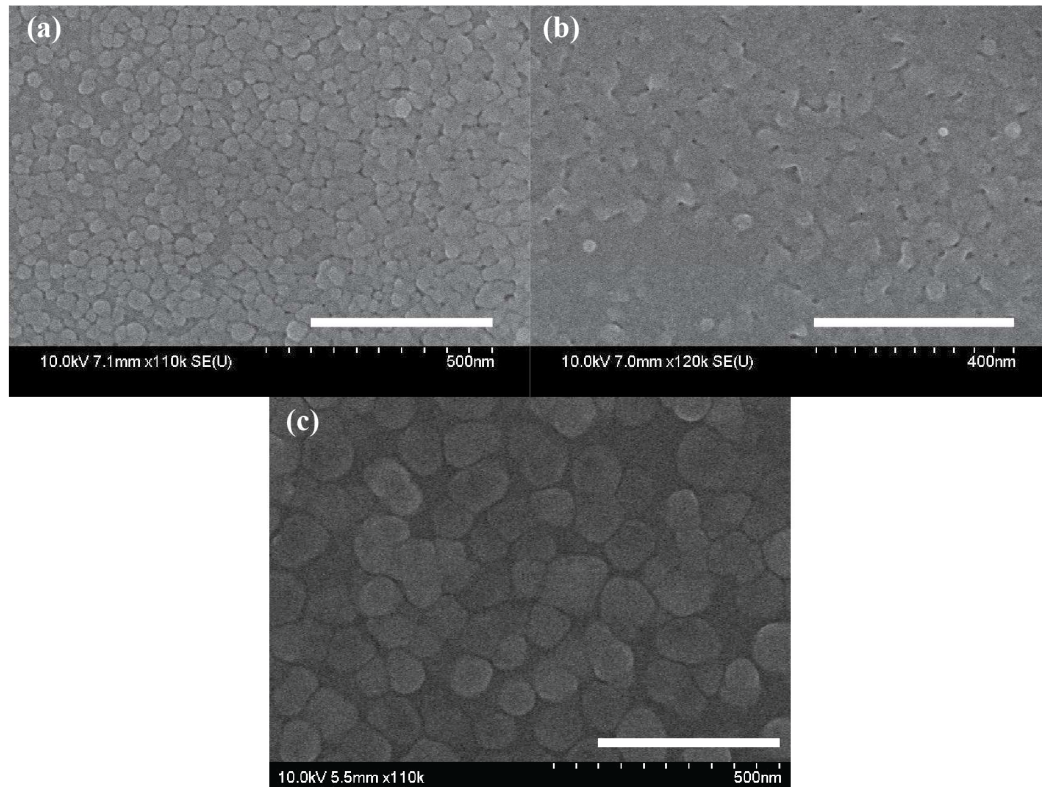
Figure 7.5: Top surface SEM images of films deposited at 0.6W, 90mTorr with substrate temperatures of (a) 25°C, (b) 100°C and (c) 375°C. All depositions were 26min long. All images were taken at 110-120kx magnification (scale bar: 400nm).

the films are amorphous. These amorphous films typically exhibit conductivity values $< 10^2$ S/m, far below the literature value for $Bi_{0.5}Sb_{1.5}Te_3$ (Table VI). Based on these results, subsequent depositions described in this chapter were done with a high substrate temperature of 375°C (nominally 430°C).

7.4.2 Effects of Background Pressure and Laser Power

The effects of the background gas pressure and the laser power on films deposited on <100> Si with a substrate temperature of 375°C was studied. Depositions were done at pressures of 2, 90, 180, 310, 590 and 1900mTorr and average laser powers of 0.6,
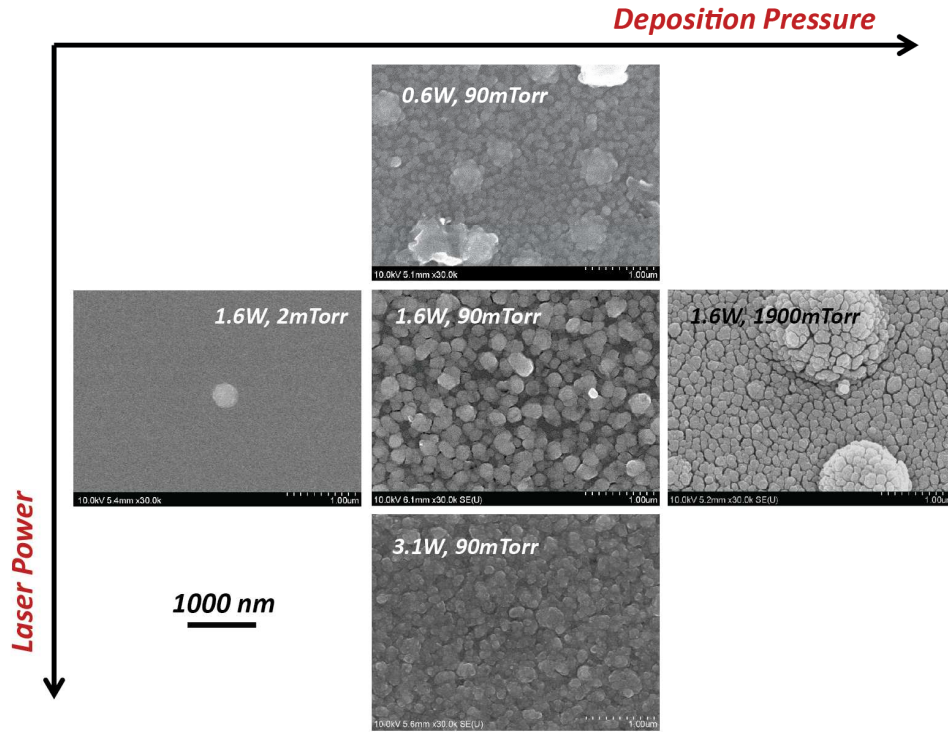
Figure 7.6: SEM images of films deposited at various pressures with various laser powers. All depositions were 26min long, and the substrate temperature was 375°C. All images taken at a magnification of 30kx (scale bar: 1000nm).
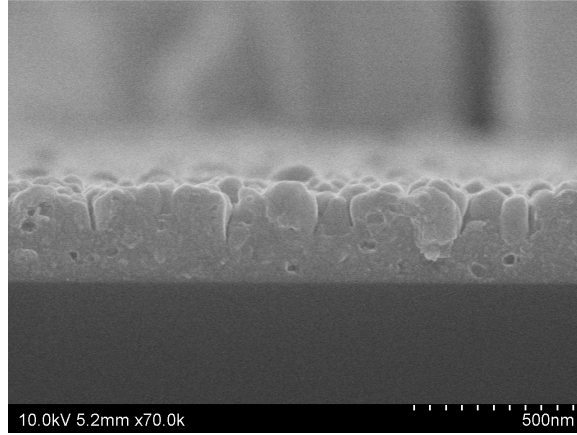
Figure 7.7: Cross-sectional SEM image of a film with a nanopillar morphology. The film was deposited at 1.6W, 590mTorr.

0.9, 1.2, 1.4, 1.6 and 3.1W. The background gas was ultra high purity nitrogen (Airgas).

The morphologies of the deposited films were compared by top-surface SEM imaging. Images of films deposited within this pressure-power parameter space are shown in Figure 7.6. The film roughness and the contrast between grains increases with both deposition pressure and laser power. However, an increase in deposition pressure also corresponds to a change in film thickness, while no such trend is clear with laser power. Low pressure (2mTorr) depositions yield extremely smooth and thin films (typically <100nm thick). For high deposition pressures (>200mTorr), the deposited film can have a pillared morphology: This is observed in the top-surface and cross-sectional SEM images (Figure 7.6, P=1900mTorr and Figure 7.7, 590mTorr). In addition to this interesting microstructure, high deposition pressures also generally lead to a strong and visible thickness gradient over the substrate area.

Examples of XRD spectra from films deposited within this range of conditions are shown in Figure 7.8. In general, low laser powers and low deposition pressures yield disordered films characterized by broad peaks (see spectrum for 1.6W, 2mTorr deposition). Crystalline films are achieved for higher powers and pressures. However, high pressure and high power depositions conditions typically
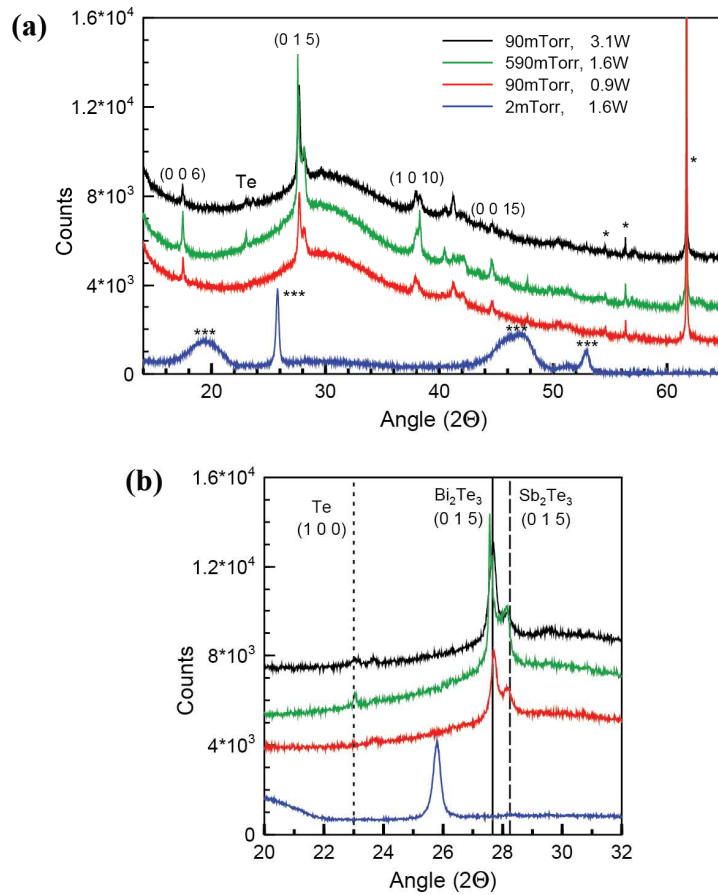
Figure 7.8: XRD spectra for films deposited with laser powers between 0.9 and 3.1W at pressures between 2 and 590mTorr. Peaks marked by * are from the Si substrate. Peaks marked by *** are from a disordered $(Bi,Sb)_x Te_y$ phase ($x:y \neq 2:3$). The peaks from (0 1 5) planes for Bi_2Te_3 and Sb_2Te_3 (JCPDS 015-0863 and 015-0874) are marked by solid and dashed black lines in (b). The (1 0 0) Te peak (JCPDS 036-1453) is seen in several of the spectra.

result in the formation of mixtures of crystalline phases, including Bi_2Te_3, Sb_2Te_3, Sb-rich alloy and/or Te (see Figure 7.8(b)). Separate Bi_2Te_3 and Sb_2Te_3 phases yield separate (015) peaks in the XRD spectrum because (as explained in Sect. 7.2.1) the a lattice parameter for these two materials is different. Separate peaks are not observed for (00l) reflections, however, because the c lattice parameters for Bi_2Te_3 and Sb_2Te_3 differ by only 0.4%.

The EDX spectrometer in the SEM was used to determine the effect of laser power and pressure on thin film composition. Before comparing the compositions of the films deposited within this set of conditions, we will discuss the challenges associated with measuring the Bi, Sb and Te content of thin films on Si by EDX. First, the EDX spectrum from a blank Si wafer exhibits a "sum" or "coincidence peak" at ~3.50keV (at 2x the energy of the $K_{\alpha 1}$ line of Si). For thin $Bi_{2-x}Sb_xTe_3$ films, this can interfere with quantification of Sb via its $L_{\alpha 1}$ peak at 3.64keV, potentially leading to an overestimation of the Sb content in the films. Second, and more significantly, the M_{z1} and M_{z2} lines from Bi have energies of 1.90keV and 1.88keV (just within the shoulder of the Si peak at 1.74keV). This can lead to a *huge* overestimation of the Bi content. In order to determine the extent of these discrepancies, ICP-OES and EDX results were compared for 21 $Bi_{2-x}Sb_xTe_3$ films deposited on Si. The fractional error f in the EDX results for the Bi:Te and Sb:Te atomic ratios for these samples, defined as

$$f = \frac{(A:Te)_{EDX} - (A:Te)_{ICP}}{(A:Te)_{ICP}} \tag{7.1}$$

(A=Bi or Sb) are given in Figure 7.9. The average value of the fractional difference between EDX- and ICP-measured Bi:Te and Sb:Te atomic ratios, marked by dashed
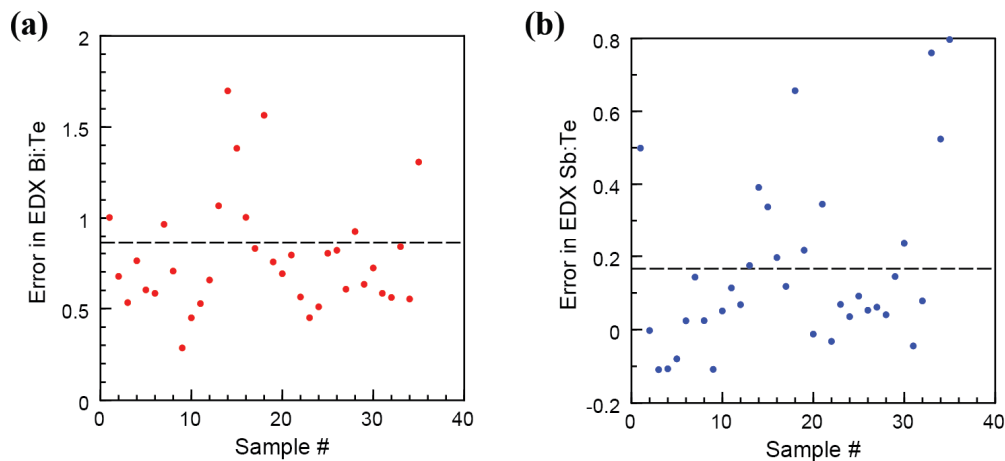
Figure 7.9: Fractional errors in the measured (a) Bi:Te and (b) Sb:Te atomic ratios for various samples. The average error is marked by a dashed black line.

horizontal lines, are +0.86 and +0.17 respectively. In the absence of ICP-OES measurements for all samples, we will use this average fractional difference to roughly estimate the true compositions of films from EDX measurements. Corrected values of the metal to tellurium (M:Te=(Bi+Sb):Te) and Sb:Bi atomic ratios for the range of deposition pressures and laser powers investigated here are given in Table IX and Table X, respectively.

Table IX. Corrected M:Te atomic ratios from EDX measurements. Cells are color-coded as follows: Red = M:Te > 1.2, Orange = 0.75 < M:Te < 1.2, Yellow= M:Te < 0.75. The target value is 0.67 (yellow).

Deposition Pressure (mTorr)

		2	90	180	310	590	1900
	0.6	1.72	0.75				
Laser	**0.9**		1.09				
Power	**1.2**	1.25	0.95	0.64	1.34	1.34	2.09
(W)	**1.4**	1.22	0.70	0.66	0.73	1.08	1.43
	1.6	1.15	0.83	0.59		0.77	1.12
	3.1		0.58				

Table X. Corrected Sb:Bi atomic ratios from EDX measurements. Cells are color-coded as follows: Red = Sb:Bi > 3.2, Orange = 2.4 < Sb:Bi < 3.2, Yellow= Sb:Bi < 2.4. The target value is 3 (orange).

Deposition Pressure (mTorr)

		2	90	180	310	590	1900
	0.6	1.43	3.26				
Laser	**0.9**		3.22				
Power	**1.2**	1.85	5.15	3.85	2.34	2.23	2.35
(W)	**1.4**	1.60	3.22	2.85	3.14	3.08	4.65
	1.6	2.88	3.03	3.20		2.75	3.75
	3.1		3.45				

The as-deposited film composition is strongly dependent on both laser power and deposition pressure. For low pressure depositions (2mTorr), the M:Te ratio is ~2x that of the target value, indicating either the presence of excess metal atoms or loss of

Te. High M:Te ratios are also seen for high deposition pressures and low laser powers. These samples also generally exhibit low values of Sb:Bi. Films closest in composition to the PLD target (M:Te=0.67, Sb:Bi=3) are obtained with intermediate deposition pressures (90 and 180mTorr) and laser powers (1.2-1.6W).

The measured room temperature electrical conductivities for this set of films are given in Table XI. These values are calculated using sheet resistances measured via the van der Pauw method (see Sect. 6.4.2) and thicknesses determined from cross-sectional SEM. An approximate error of ~10% in the conductivity values is expected due to errors and variations in thickness. The electrical conductivity increases significantly with decreasing deposition pressure and increasing laser power.

Table XI. Electrical conductivity (in S/m) for films deposited with a range of pressures and laser powers. Cells are color-coded by order of magnitude, between 10^4 (red) and 10^0 (blue).

Deposition Pressure (mTorr)

		2	90	180	310	590	1900
	0.6	5.27E+03					
Laser	0.9						
Power	1.2		1.15E+02			7.56E+00	
(W)	1.4	5.88E+04	4.99E+01	5.01E+01	1.66E+00	6.99E+01	
	1.6	4.48E+04	2.51E+02	4.39E+01	3.37E+01	1.88E+02	8.31E+01
	3.1		7.86E+01				

The measured values of the Seebeck coefficient (in units of µV/K) are given in Table XII. As mentioned in Sect. 6.4.1, the Seebeck coefficient is measured by

heating one end of the sample. Depending on the range of heating powers and the geometry of the sample, temperature drops from ΔT=0.5 to 4 C are measured across the sample, while the average temperature increases less than ~30 C above room temperature throughout the measurement. For each measurement, the Seebeck coefficient typically varies by <10% for the range of ΔT. The value of the Seebeck coefficient reported in Table XII is then an average over the values from the entire measurement (the range of ΔT). As anticipated, the magnitude of the Seebeck coefficient generally *decreases* with increasing conductivity (lower deposition pressures and higher laser powers). Interestingly, however, several films deposited at 2mTorr exhibit negative Seebeck coefficients.

Table XII. The Seebeck coefficient (in µV/K) for films deposited with a range of pressures and laser powers. "X" indicates that the conductivity is too low to perform a Seebeck measurement (i.e. good contact could not be made between the thermocouples and the film). Cells are color-coded based on their sign and magnitude.

Deposition Pressure (mTorr)

		2	90	180	310	590	1900
	0.6	60					
Laser	0.9						
Power	1.2	-16	575			X	
(W)	1.4	-32	X	X	X	X	X
	1.6	-35	X	1600	X	215	X
	3.1		395				

Table XIII. Power factor values (in W/m-K^2) for films deposited with a range of pressures and laser powers. Color denotes order of magnitude between 10^{-6} (yellow) and 10^{-4} (red).

Deposition Pressure (mTorr)

		2	90	180	310	590	1900
Laser Power (W)	0.6	2.05E-05					
	0.9						
	1.2		4.10E-05				
	1.4	6.02E-05					
	1.6	5.49E-05	7.59E-05	1.18E-04		8.71E-06	
	3.1		1.38E-05				

The power factor values for these films are given in Table XIII. The highest power factor values are measured for intermediate gas pressures and laser powers—the same deposition conditions that typically yield films closest in composition to the PLD target. The best power factor value in Table XIII, however, is still ~40x lower than the literature value for $Bi_{0.5}Sb_{1.5}Te_3$ 4.6x10^{-3} W/m-K^2. The n-type films deposited at low pressures with compositions that deviate significantly from the target exhibit power factor values comparable to the stoichiometric films. These results point to the crucial need for post-deposition annealing for improving the composition, texture and transport properties of pulsed laser deposited $Bi_{2-x}Sb_xTe_3$ films over the entire range of deposition conditions.

7.4.3 Other Deposition Considerations

- Large (~1-10μm) sized particulates can often be seen on top of the film surface (see Figure 7.10). In general, these large particulates cover <5% of the film surface (the area shown in Figure 7.10 has significantly more large particulates than is typical). We find that the density of these particulates does not depend on the deposition pressure, laser power or the separation between the substrate and the target. Based on their shape, we hypothesize that these particulates are large molten pieces that are ejected from the target onto the substrate during deposition. Future optimization of the deposition conditions should include implementation of a filter or shadow mask, which have been shown to be successful in preventing deposition of these large particles.[1]

- The pressure in the chamber after deposition (during the first ~30min of cooling) has a significant effect on the properties of the films. This is
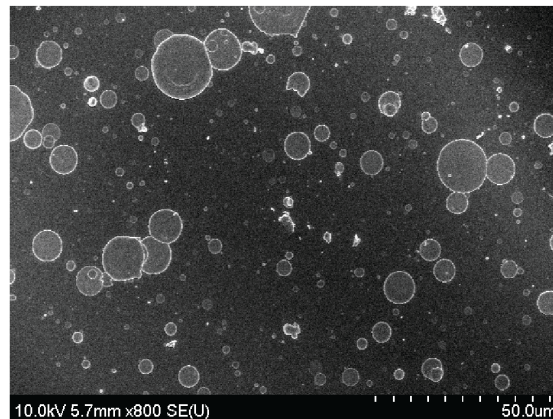
Figure 7.10: Low magnification top surface SEM image of a film with a particularly high density of large particulates.

especially important for films deposited at low pressure (2mTorr)—if the background pressure is not raised to ~2 Torr within 30min of deposition, additional Te is lost, resulting in high M:Te atomic ratios and disordered crystal structures.

7.5 *Investigation of Annealing Conditions*

The best power factor values from the as-deposited films described in Sect. 7.4.2 are still significantly lower than the literature value for $Bi_{0.5}Sb_{1.5}Te_3$. In this section, we demonstrate improvements in the properties of the films with annealing.

7.5.1 Annealing in Nitrogen

Annealing the deposited films in a N_2 atmosphere can potentially promote grain growth, leading to better thermoelectric transport properties. Below we present annealing studies for films deposited at 1.6W and 2mTorr for 26min. We note that
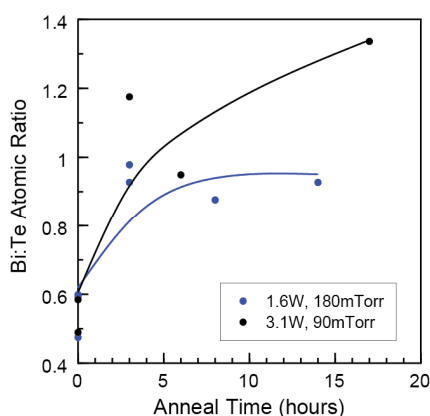
Figure 7.11: Atomic ratio Bi:Te (measured from EDX and corrected using ICP measurements of other samples) as a function of annealing time for deposition conditions of 1.6W, 180mTorr and 3.1W, 90mTorr. Solid lines are used as a guide.

annealing of films deposited at higher laser powers and deposition pressures (3.1W, 90mTorr and 1.6W, 180mTorr) was also investigated. While the crystallinity of these films improved with annealing in N_2, in general annealing did not lead to the formation of the alloy phase in these films. XRD results always indicate the presence of two separate Bi_2Te_3 and Sb_2Te_3 phases. Further, the compositions of the films deposited with these conditions actually get worse (further from the target stoichiometry) with annealing (see Figure 7.11). It is therefore not surprising that no significant improvement in the power factor values of these films could be achieved by annealing in N_2. The Seebeck coefficient (starting from >400µV/K) generally decreases with annealing suggesting an increase in carrier concentration, but even the best samples still exhibit conductivities 10x lower than bulk after annealing for 15hrs.

For the annealing study presented here, all films were deposited on <100> Si with a laser power of 1.6W and a deposition pressure of 2mTorr. Immediately after deposition, the temperature was increased from 375 to 390°C (nominally 430 to 450°C) and the N_2 flow was increased to reach a chamber pressure of 2Torr. The films were annealed at this temperature and pressure for various amounts of time between 0 and 17hrs, and then cooled to room temperature under 2 Torr of N_2.

The values of the Seebeck coefficient for this set of films are shown as a function of annealing time in Figure 7.12(a). The electrical conductivity and power factor values are given (normalized to the values measured as-deposited) as a function of annealing time in Figure 7.12(b). While the electrical conductivity is relatively constant, the Seebeck coefficient improves by a factor of nearly 3 with annealing. This leads to a factor of more than 8 increase in the power factor value with 17hrs

143
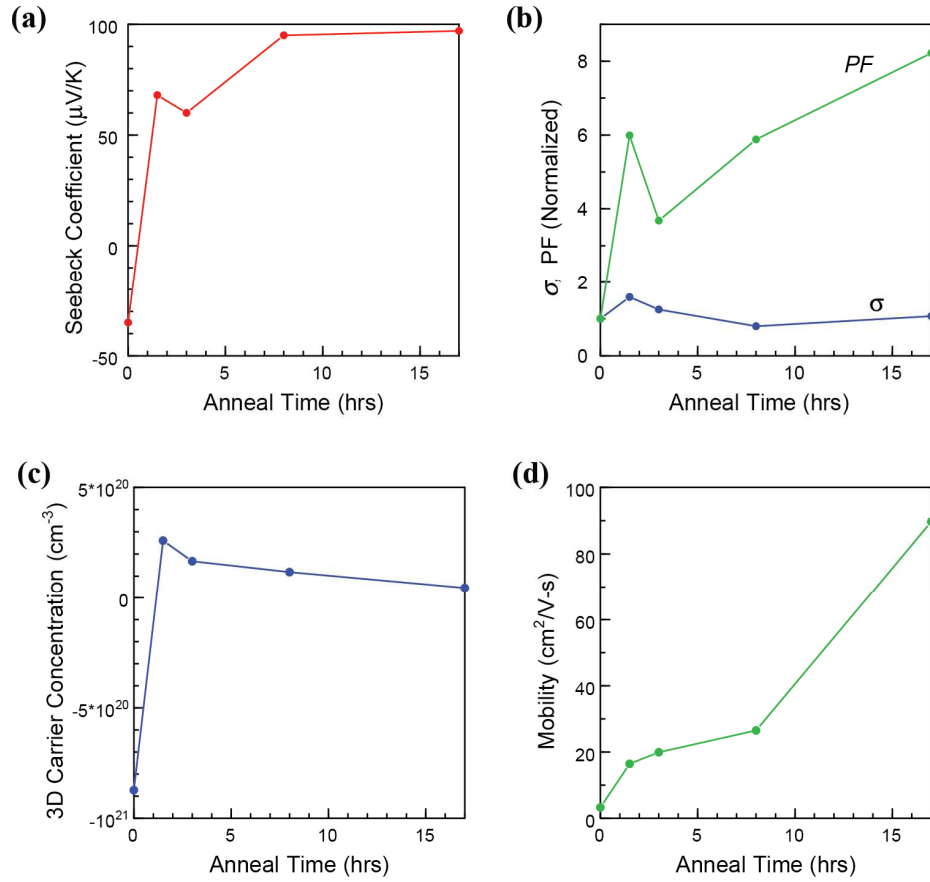
Figure 7.12: (a) Seebeck coefficient, (b) electrical conductivity and power factor (normalized to the values measured as-deposited), (c) 3D carrier concentration and (d) Hall mobility as a function of annealing time.

annealing. Measured values of the carrier concentration and Hall mobility are given as a function of annealing time in Figure 7.12(c) and (d). These values were determined from Hall measurements done using the HMS-5000 Hall Effect Measurement System in the Fablab, equipped with a 0.51T magnet. With annealing, the magnitude of the carrier mobility increases by nearly 2 orders of magnitude while the carrier concentration changes sign and decreases by a factor of 20. These results are indicative of grain growth.
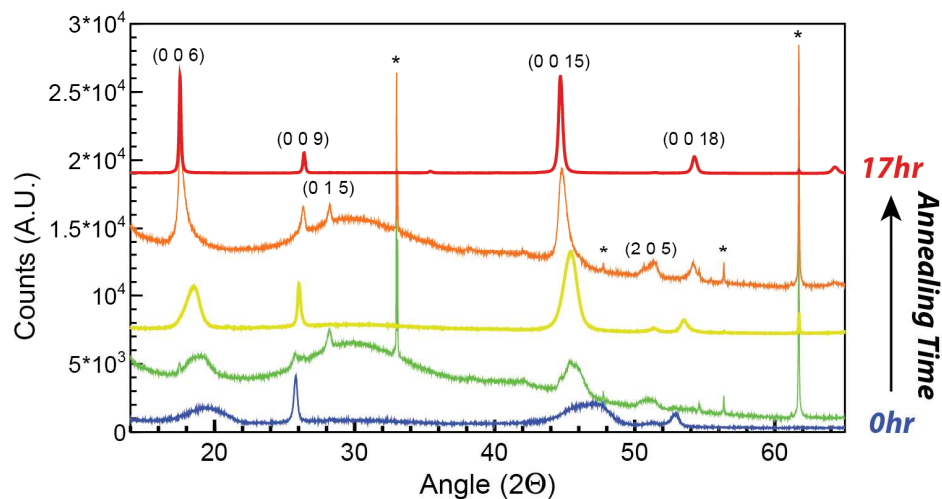
Figure 7.13: XRD spectra for films annealed in N_2 between 0 and 17hrs. Annealing time increases from blue to red (bottom to top). Several $Bi_{2-x}Sb_xTe_3$ peaks (JCPDS 072-1836) are labeled. Peaks from the Si substrate are marked by *.

The XRD spectra for this set of films are compared in Figure 7.13. With N_2 annealing, the film transforms from a disordered structure, exhibiting several broad peaks, into a crystalline and highly textured structure, exhibiting exclusively high-intensity $(00l)$ family peaks. The structural transformation is evident from changes in the peaks near 19 and 47 : these peaks narrow and shift to lower angles (higher lattice constants) with annealing. After 17hrs annealing, these peaks are aligned with expected (0 0 6) and (0 0 15) reflections for the alloy. We note that this does *not* occur for the (0 0 9) and (0 0 18) peaks, which maintain the same width and shift to *higher* angles with annealing.

The improved crystallinity of the films with annealing can also be seen in top-surface SEM images (Figure 7.14). As-deposited, the films are smooth and grain boundaries are difficult to resolve (see image for 1.6W, 2mTorr deposition conditions in Figure 7.5). With annealing, grain boundaries are visible and the grain size
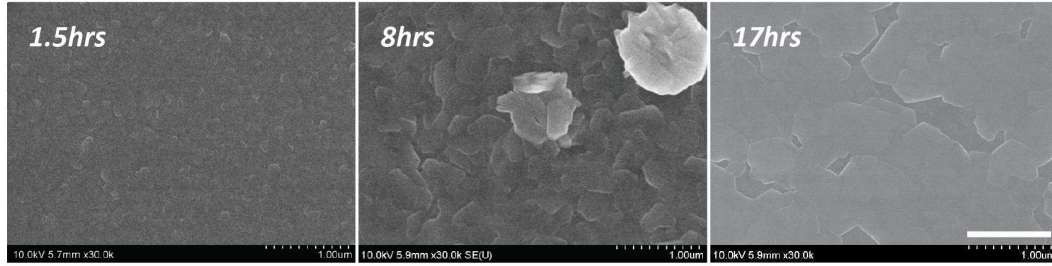
Figure 7.14: SEM images of films annealed under N_2 for 1.5, 8 and 17hrs. All images were taken at a magnification of 30kx. Scale bar: 1000nm.
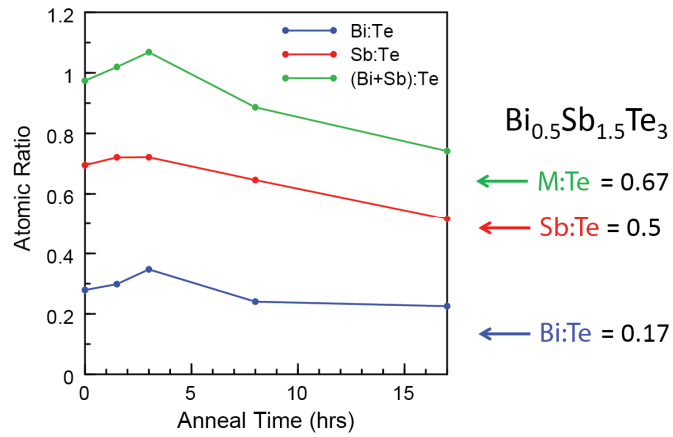
Figure 7.15: Atomic ratios (measured using ICP-OES) as a function of annealing time. Target values are indicated by arrows on the right.

increases with the length of the anneal. After 17hrs annealing, the grains are highly faceted (many exhibiting a hexagonal shape) and plate-like, parallel to the substrate.

For films annealed in N_2 for more than 1.5hrs, the XRD spectra indicate the presence of a single phase, identified as the $Bi_{2-x}Sb_xTe_3$ alloy. When separate Bi_2Te_3 and Sb_2Te_3 phases are present, two peaks are seen for many of the reflections (for example, the (0 1 5) reflection shown in Figure 7.8). The exact composition of the $Bi_{2-x}Sb_xTe_3$ alloy is difficult to determine from the XRD results, even for the highly textured 17hr-annealed sample. This is because, as explained in Sect. 7.2.1, the c
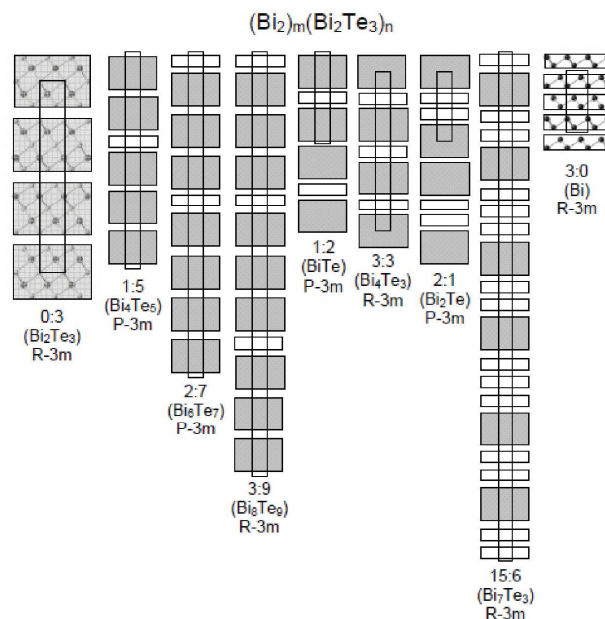
Figure 7.16: Schematic of the structure of compounds between Bi_2Te_3 and Bi_2. The Bi_2Te_3 (gray) and Bi_2 (white) "blocks" are shown on the left and right, respectively. From [7].

lattice parameters for Bi_2Te_3 and Sb_2Te_3 are nearly identical (varying by only 0.4%), and the value of c for the alloy is not well-established.

The change in composition with N_2 annealing helps to shed light on the structural transformation shown in Figure 7.13. The atomic ratios Bi:Te, Sb:Te and M:Te measured with ICP-OES are given as a function of annealing time in Figure 7.15. As-deposited, the films contain excess Sb and Bi. With annealing, the Bi:Te, Sb:Te and M:Te ratios decrease down to the target value. The ratio of Sb to Bi (not shown) is relatively constant at ~2.5 for the entire range of annealing times, indicating that Sb and Bi are maintained in the film during the N_2 annealing or lost at approximately the same rate.
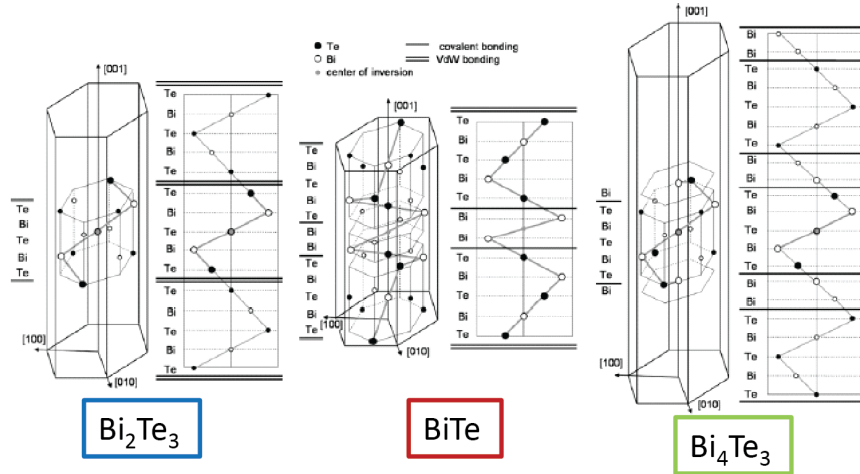
Figure 7.17: Crystal structures of Bi_2Te_3, BiTe and Bi_4Te_3, from [12]. The layers of excess Bi are sandwiched between Bi_2Te_3 unit cells.

The structural characteristics of Bi-rich phases of the Bi-Te system have been investigated recently by several groups.[7, 12, 15, 95] The range of layered compounds between pure Bi and Bi_2Te_3 are part of a homologous series $(Bi_2)_m(Bi_2Te_3)_n$; all known intermediate phases (including Bi_4Te_3 and BiTe) can be understood as stacks of Bi_2 blocks sandwiched between blocks of Bi_2Te_3 (shown schematically in Figure 7.16). The crystal structure of Bi_2Te_3 is compared to that of BiTe and Bi_4Te_3 in Figure 7.17. XRD spectra reported by Russo *et al.*[12] for films with compositions between 40% Bi and 65% Bi are shown in Figure 7.18. This range of films was deposited via PLD from a stoichiometric Bi_2Te_3 target; similar to what we have described above, textured Bi-rich films are achieved for low deposition pressures. For BiTe and Bi_4Te_3, the high-intensity (00l) reflections are (0 0 5), (0 0 12) and (0 0 9), (0 0 21), respectively (compared with (0 0 6), (0 0 15) in Bi_2Te_3). For intermediate compositions (45% and 53% Bi), peaks from two phases are typically
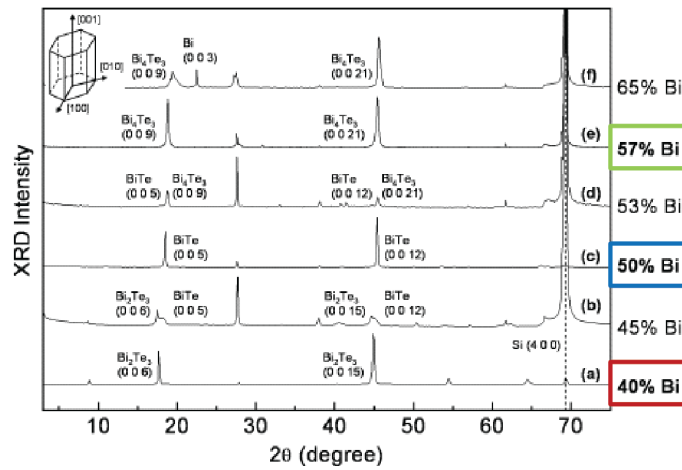
Figure 7.18: XRD spectra of pulsed laser deposited Bi-Te films with a range of compositions, from [12]. The Bi_2Te_3, BiTe and Bi_4Te_3 compositions are highlighted in red, blue and green respectively.

present. A similar series of phases has been demonstrated for the Sb-Te system[96]. Though to our knowledge no such investigation has been performed on the alloy (Bi,Sb)-Te, the layered structure of the (Bi,Sb)-Te system is the same as that of Bi-Te and Sb-Te. The structural transformation in our films with annealing (Figure 7.13) is therefore understood as a transition from a disordered metal-rich phase (potentially $Bi_{1-x}Sb_xTe$ or $Bi_{4-x}Sb_xTe_3$) into the phase of the target, $Bi_{2-x}Sb_xTe_3$. At this time, it is unclear what the source of the disorder is (nanoscale grains, variation in the lattice constant, the presence of multiple phases, misaligned layers, etc.). Further investigation of the disordered films by Raman spectroscopy could shed light on this question.[12]

The change in transport properties with annealing (see Figure 7.12) can therefore be understood as the result of both grain growth as well as a change in material (from a disordered metal-rich phase into the stoichiometry of the target).

149

These results further support the proposed structural transformation described above: Russo *et al*. reported that the metal-rich phases exhibit significantly lower magnitudes of the Seebeck coefficient and mobility, and higher carrier concentrations.

The results described in this section indicate that annealing films under N_2 leads to better crystallinity and better stoichiometry in the $Bi_{2-x}Sb_xTe_3$ pulsed laser deposited films (grain growth, and the formation of the target $Bi_{2-x}Sb_xTe_3$ phase). As a result, the power factor values increase with annealing. However, the highest power factor value achieved after annealing for 17hrs is still almost an order of magnitude lower than the literature value. In the next section, we explore the effect of annealing under a Te vapor to further improve the power factor values.

7.5.2 Annealing In Tellurium Vapor

Loss of Te in Bi_2Te_3-based nanostructures can lead to deterioration in the thermoelectric transport properties. One technique developed to resolve this issue is to anneal the nanostructures in a Te vapor (as opposed to an inert gas). This idea was originally proposed by Taylor *et al*. in 2010, and was shown to yield excellent control over the composition and carrier concentration of thermally evaporated Bi-Te thin films.[97] Improvements of 50% in the Seebeck coefficient were demonstrated after just 60min annealing in a Te vapor. Similar results have since been reported for electrochemically deposited Bi_2Te_3,[11] $Bi_{2-x}Sb_xTe_3$ and $Bi_2(Te_xSe_{1-x})_3$ [98] thin films. The results of the former study, shown in Figure 7.19, indicate that the Seebeck coefficient of Bi-rich films increases by as much as 300% as the composition becomes stoichiometric with annealing. Interestingly, Te vapor annealing was
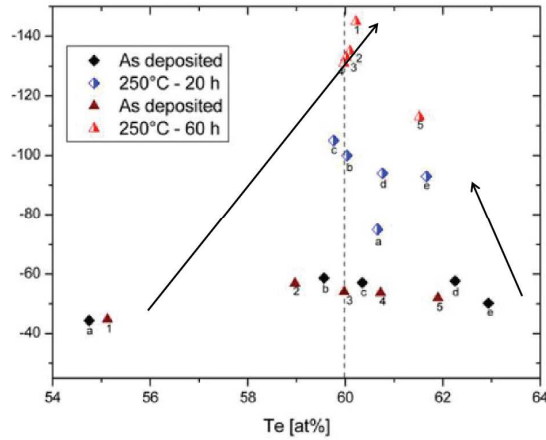
Figure 7.19: Seebeck coefficient as a function of composition for two sets of $Bi_{2+\delta}Te_3$ films as-deposited (filled markers) and annealed (half-filled markers). The arrows indicate the changes in Seebeck and composition with annealing for 2 particular samples. Adapted from [11].

beneficial both for Bi-rich and Te-rich compositions, indicating that the annealing does not result in excess incorporation of Te even for long anneal times.

The proposed transformation with annealing in a Te vapor is depicted schematically on the Bi-Te phase diagram in Figure 7.20. For Bi-rich films, the excess Bi reacts with the Te gas until a uniform Bi_2Te_3 phase is reached. As annealing continues, equilibrium is reached only when the vapor pressures of the film and the gas are equal—this happens when the Bi_2Te_3 film becomes slightly Te-rich (the phase boundary marked near 60.2% Te in Figure 7.20). Recovery of a Bi_2Te_3 stoichiometry from a more strongly Te-rich (>61% Te) film (moving from right to left in Figure 7.20) is less straight-forward and generally not seen experimentally.
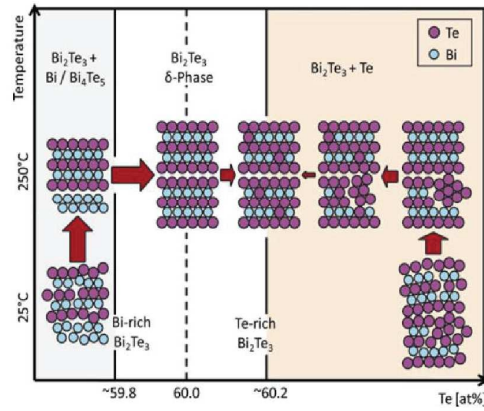
Figure 7.20: Schematic of the proposed structural transformation that occurs with annealing in a Te vapor on the Bi-Te phase diagram. From [11].

In the works just described, vapor annealing of the samples was done in evacuated glass ampoules containing powder Te sources. With the dual PLD-TE system described in Sect. 6.3, annealing in Te vapor can be done in the chamber immediately after pulsed laser deposition using the thermal evaporation system. In this section, we will describe the process used and present results for films annealed for various lengths of time. As with the previous section, we focus on the effect of annealing metal-rich films deposited on <100> Si with a laser power of 1.6W at a background pressure of 2mTorr.

Molybdenum boats coated with alumina (Kurt Lesker EVS2BA0M0) loaded with Te pellets (99.999% Te purchased from Sigma-Aldrich) are used for the thermal evaporation process. Immediately after deposition, the temperature of the substrate is increased to 390°C and the substrate is moved to ~20cm from the evaporation boats. Annealing is done at the same pressure as the deposition (2mTorr); lower pressures are avoided to prevent additional loss of Te and higher pressures make it difficult to

measure and control the Te evaporation rate. Typically, the power to the evaporation electrodes is held constant (~60mW), and the rate of Te deposition read on the Inficon Deposition Controller varies between ~0.005-0.01 Å/sec. We note, however, that this is used only as a rough estimate for the deposition rate as the value is extremely low and likely inaccurate. The films are annealed with continuous Te evaporation for various lengths of time between 0 and 22hrs, after which the pressure is increased to 2Torr for cooling.

The XRD spectra for several films annealed in Te vapor are shown in Figure 7.21. These results indicate the same transformation from disordered to textured morphologies with annealing (compare with Figure 7.13). Further, despite the large quantities of Te evaporated (ex: assuming a rate of 0.01 Å/sec, we could expect a thickness of 47nm evaporated Te on the substrate), no separate crystalline Te is seen
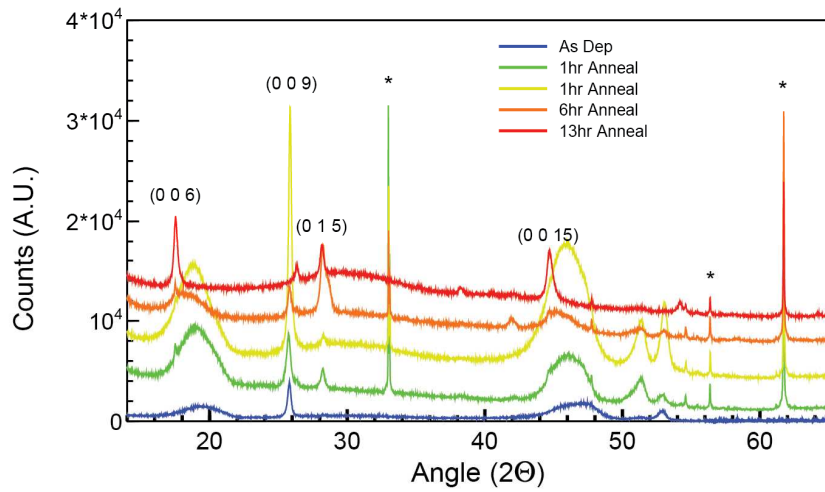
Figure 7.21: XRD spectra for several films annealed in Te vapor (1-13hrs) compared with the spectrum from a film as-deposited. Several high-intensity $Bi_{2-x}Sb_xTe_3$ peaks are marked. Peaks from the Si substrate are marked by *.

in the films. Throughout the annealing process, the Te is completely incorporated into the film or pumped away.

The compositions of the Te annealed films were measured by ICP-OES. The measured ratios (Bi+Sb):Te are shown as a function of annealing time in Figure 7.22(a). The power factor values measured for the same set of samples are shown in Figure 7.22(b). In general, the M:Te ratio approaches the target value of 0.67 and the power factor increases with annealing time (the rates of change for the M:Te atomic ratios and the power factor are given in Table XIV). However, it is important to note the significant scatter in M:Te ratios and power factor values in the sample set. The power factor values (shown in Figure 7.22(b)) range between 1×10^{-5} W/m-K^2 and 11.3×10^{-3} W/m-K^2—the high end value is 2.5x the bulk value.

Table XIV. Rates of change in the M:Te atomic ratios and the power factor values with annealing in N_2 with a Te vapor, and annealing in N_2. These values are equal to the slope of the lines in Figure 7.22.

Annealing Conditions	d(M:Te)/dt (1/hr)	d(PF)/dt (W/m-K^2-hr)
N_2 annealing with Te	$-0.76 \times 10^{-2} \pm 0.22 \times 10^{-2}$	$1.4 \times 10^{-5} \pm 1.1 \times 10^{-5}$
N_2 Annealing	$-1.7 \times 10^{-2} \pm 0.48 \times 10^{-2}$	$1.75 \times 10^{-5} \pm 0.75 \times 10^{-5}$
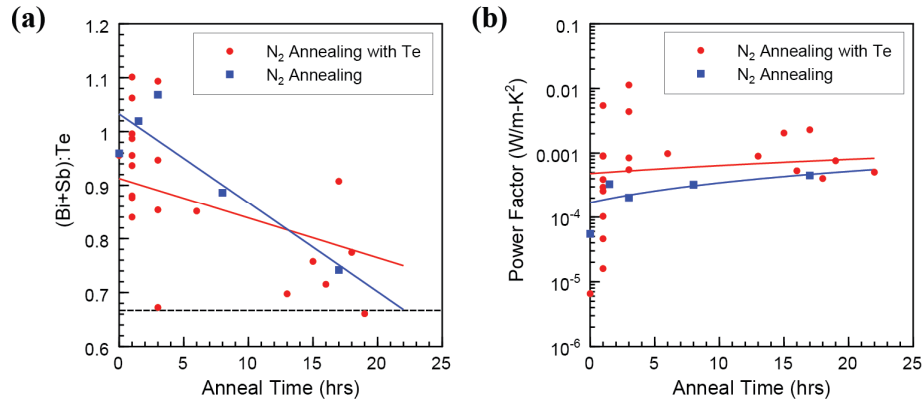
Figure 7.22: (a) Atomic ratio of metal to Te atoms (measured using ICP-OES) as a function of annealing time. Results for films annealed in Te vapor (red) are compared with those for films annealed in N_2. The stoichiometric ratio of the target is marked by a dashed horizontal line. (b) Power factor values as a function of annealing time for the same set of samples.

Annealing under Te vapor leads to higher power factor values than annealing in N_2; however, the results in Figure 7.22 indicate that (1) the power factor values are generally still lower than that of bulk and (2) the annealing process is not well-controlled. It is not yet clear from the analysis of crystal structure or composition what distinguishes the films with high power factor values ($> 4 \times 10^{-3}$ W/m-K^2) from the rest of the samples. Further investigation is needed to optimize this annealing process; preliminary work on the effect of thermal evaporation power indicates that higher Te evaporation rates may lead to consistently higher power factor values for short annealing times.

7.6 Summary

In this chapter, we presented an investigation of the effect of various deposition conditions (substrate temperature, laser power, background pressure) on the properties of $Bi_{2-x}Sb_xTe_3$ films deposited via PLD. We find that a relatively high

substrate temperature is required to yield conducting and somewhat crystalline films. The films closest to the target composition are deposited for intermediate choices of the laser power and background pressure. If the pressure is above 2mTorr, however, the deposited film contains separate Bi_2Te_3 and Sb_2Te_3 phases and we occasionally see segregation of crystalline Te.

We focused on films deposited with a laser power of 1.6W and a pressure of 2mTorr for an annealing study. As-deposited, these films consist of a metal-rich phase with structural disorder and can exhibit negative Seebeck coefficients. With annealing in N_2, the films become crystalline (reverting to the M:Te 2:3 stoichiometry of the target) and highly textured (with grains preferential aligned along the (00l) direction). This improvement in crystallinity is accompanied by decreases in the carrier concentration and increases in the mobility. While we see a change in both the sign (from n-type to the expected p-type) and the magnitude (a ~3x increase) of the Seebeck coefficient, there is little change in the conductivity with annealing. The result is a factor of more than 8 improvement in the power factor value.

Finally, we investigated the effect of annealing the films in Te vapor in the PLD-TE chamber immediately after film deposition. While the results seem promising in terms of power factor values (generally, the power factor of films annealed in a Te vapor is larger than that of films annealed in N_2), so far we do not have good enough control over the annealing process. Several films exhibit power factor values comparable to or higher than the bulk value, but with the current deposition and annealing process the thermoelectric transport results vary from run to run.

Chapter 8 Fabrication of Porous Bi$_{2-x}$Sb$_x$Te$_3$ Thin Films

In the previous chapter, we investigated the effect of deposition and annealing conditions on the properties of pulsed laser deposited Bi$_{2-x}$Sb$_x$Te$_3$ thin films, and identified conditions that yield crystalline films with relatively good thermoelectric transport properties. In this chapter, we present an approach to fabrication of porous thin films using these optimized conditions. We induce porosity in the film using a templated deposition approach: The Bi$_{2-x}$Sb$_x$Te$_3$ films are deposited onto porous substrates (typically anodic alumina templates). We discuss the methods used to fabricate these porous substrates, and then compare the properties of porous and dense films deposited using this technique.

8.1 *Introduction to Porous Thermoelectric Materials*

In light of the low power factor values reported for most "simple" nanostructures, recent work in the field of thermoelectric materials has focused on more complex nanostructuring techniques, including synthesis of nanocomposite and nanoporous materials.[99] These complex thermoelectric materials are bulk or nanostructured systems with embedded nanoparticles or nanoscale pores (see Figure 8.1). The nanoscale grain boundaries introduced through these methods will scatter phonons, leading to lower values of the thermal conductivity—a conclusion supported by ample theoretical[5, 99-101] and experimental[13, 99] work. An example of one such experimental system, holey Si nanoribbons, is shown in Figure
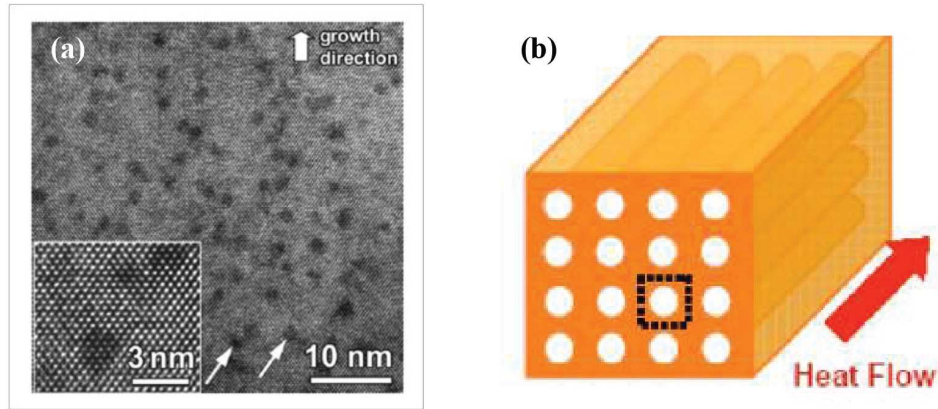
Figure 8.1: (a) High resolution TEM image of ErAs nanoparticles embedded in a matrix of InGaAs (a nanocomposites material), from [10]. (b) Schematic of nanoporous Si, from [21].

8.2. In this system, the nanopores introduced using a nanosphere lithography technique result lead to a more than 20x decrease in the thermal conductivity over non-holey nanoribbons.

Complex nanostructuring of thermoelectric materials is of interest in the context of this work for the predicted increase in the Seebeck coefficient through preferential scattering of low-energy electrons. The concept of "energy filtering" is to control carrier scattering in such a way that the improvement in the Seebeck coefficient more than makes up for any decrease in carrier mobility—the result is a net improvement in the power factor. Using the terminology from Sect. 5.2, energy filtering can be understood as the introduction of a scattering mechanism characterized by scattering parameter $p>0$ (see Figure 8.3(a)). As suggested in Sect. 5.3, preferential scattering of low-energy electrons can be good for thermoelectric transport.
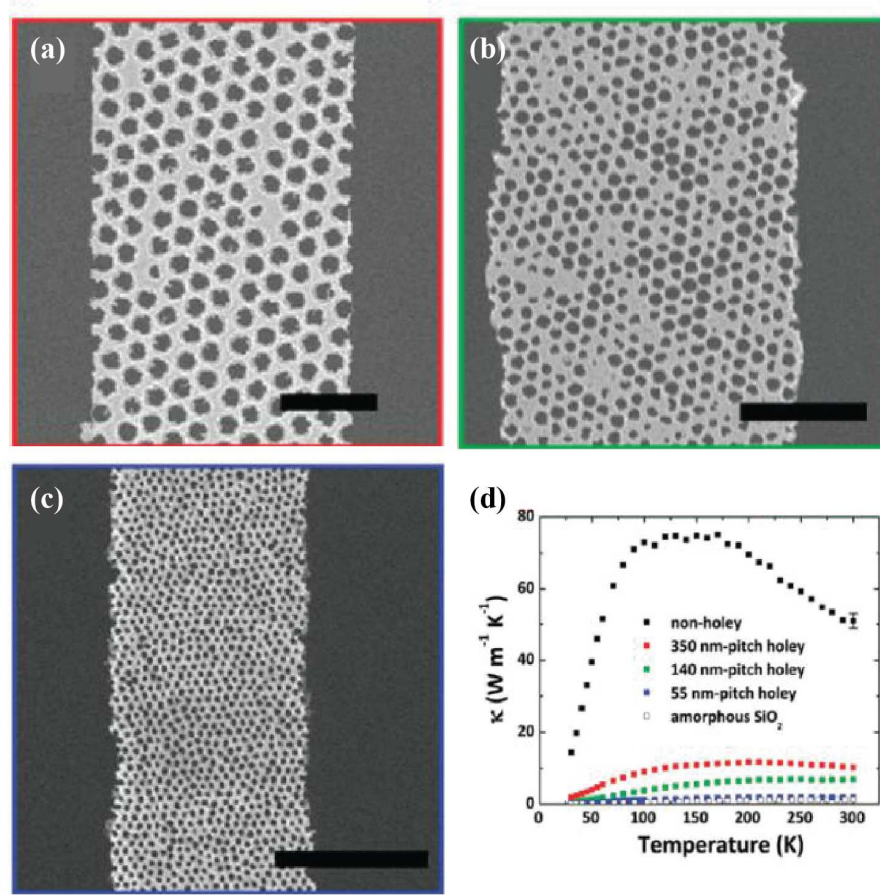
Figure 8.2: (a)-(c) SEM images of holey Si nanoribbons with various pore sizes. Scale bar: 1μm. (d) Thermal conductivity as a function of temperature for the nanoribbons in (a)-(c), compared with a non-holey nanoribbon (black) and amorphous SiO_2 (white). From [13].

The benefits of energy filtering have been reported experimentally for several nanocomposite and nanoporous materials systems.[67, 68, 99] Subsequent modeling of the thermoelectric transport properties of these systems supports the conclusion that the observed improvements in the Seebeck coefficient can be attributed to the effects of energy filtering.[5, 69, 102] In general, however, these theoretical works also predict a decrease in the magnitude of the scattering time and in the electrical
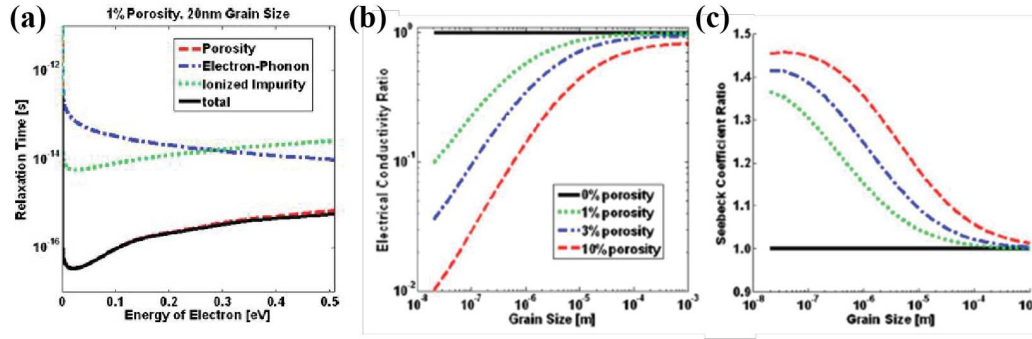
Figure 8.3: Simulations of transport properties in porous SiGe.[5] (a) Carrier relaxation time as a function of energy. (b) Electrical conductivity and (c) Seebeck coefficient as a function of pore size for various values of porosity, taken relative to comparable dense material. Grain size and pore size were assumed to be equal.

conductivity with the introduction of nanoinclusions and nanoscale pores (see Figure 8.3(a) and (b)). An improvement in the power factor value is contingent on the proper choice of material, and on the size and density of the nanoinclusions/nanopores.

8.2 *Pulsed Laser Deposition of Porous Bi$_{2-x}$Sb$_x$Te$_3$ Thin Films*

Porous thin films can be fabricated using methods within one of two general categories: (1) templating techniques, in which a porous film is formed on top of a porous substrate or (2) top-down techniques, in which a dense film is patterned to create pores. In the present work, we have focused almost entirely on the former. Porous Bi$_{2-x}$Sb$_x$Te$_3$ films were fabricated via pulsed laser deposition on porous substrates (anodic alumina templates and etched Si). In this section, we describe the techniques used to fabricate these porous substrates and present characterization of porous thin films fabricated using this method. The results reported in this section,

however, were obtained almost entirely on porous films on anodic alumina. The procedure for fabrication of porous Si is given as guidance for further investigations.

8.2.1 Fabrication of Anodic Alumina Templates

Under the right anodization conditions, the surface of aluminum can be converted into an ordered porous oxide structure, with cylindrical pores running parallel to each other and perpendicular to the surface. The depth of the pores is determined by the time of anodization. The pore diameter is controlled by the anodization conditions (voltage and acid electrolyte), and can vary between ~25 and 200nm. Anodic alumina templates are used for a wide range of applications, including as filters[103], templates for deposition of nanowires and nanotubes[104] and masks for patterning nanodots or porous thin films.[105] The steps in fabrication of anodic alumina templates on Si substrates (for mechanical support) are:

1. Deposition of Al: Al films are deposited onto <100> Si wafers at ~10^{-6} Torr using the thermal evaporation system of the PLD-TE instrument (Sect. 6.3). A ~15nm Ti adhesion layer (99.98% slugs, Alfa Aesar) is deposited, at a rate of ~0.3 Å/s using EVSBA0M0 molybdenum boats coated with alumina (Kurt Lesker). Once the substrate cools to room temperature (the high power required to evaporate Ti leads to heating of the substrate), a ~600nm thick Al film is deposited at a rate of ~2 Å/s using 99.999% Al pellets and ECS20A015W thick–gauge tungsten boats (Kurt Lesker).

2. Polishing of Al: In some cases, the deposited Al films do not have a mirror finish. Surface roughness can lead to problems during anodization. These films are polished for ~20min at 100RPM using a Buehler ECOMET 3 Grinder/Polisher with a 20nm colloidal silica nanoparticle solution (Buehler).

161

3. Anodization: Just prior to anodization, the Al films are soaked in a mixture of chromic acid (45 g/L) and phosphoric acid (3.5 vol%) to remove any native oxide layer from the surface of the Al. The wafers are then mounted onto glass slides using an insulating adhesive (Crystalbond 509-3, Ted Pella, Inc.) with the Al facing out. The films are then anodized at ~10°C using one of two anodization conditions: (1) For ~50nm pores with a period of ~100nm, the Al is anodized at 40V in a 0.3M oxalic acid solution. (2) For ~25nm pores separated by ~60nm, the Al is anodized at 25V in a 0.3M sulfuric acid solution.[106] Anodization is stopped when the Al film becomes completely transparent and the current drops to zero; in general, the Al anodizes at a rate of ~30nm/min.

4. Preparing the top surface: The anodic alumina films are polished (15-30min at 100RPM with the 20nm colloidal silica solution) to expose the ordered structure. The
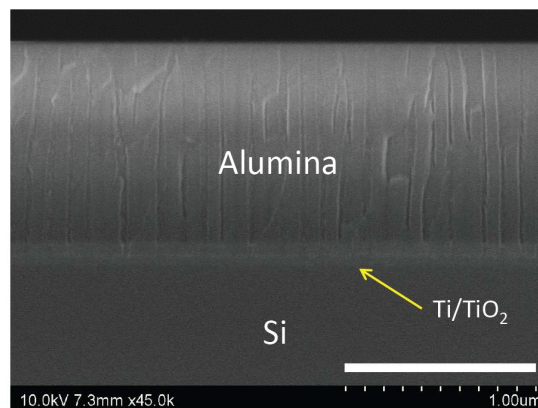
Figure 8.4: Cross-sectional SEM image of an anodic alumina template. (From bottom to top: the Si substrate, the ~30nm of Ti/TiO$_2$ layer and the porous alumina structure.) Scale bar: 1000nm.
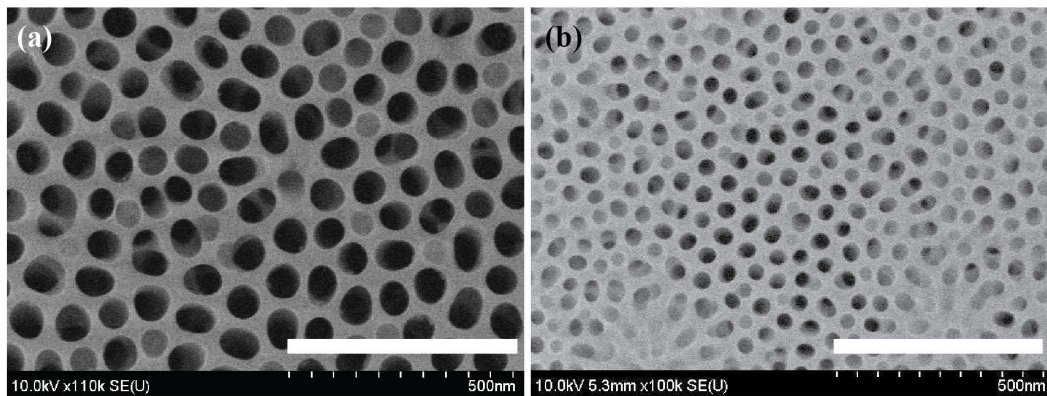
Figure 8.5: Top surface SEM images of alumina templates anodized using (a) 40V, 0.3M oxalic acid and (b) 25V, 0.3M sulfuric acid. Scale bars: 500nm.

pores are then widened slightly by etching for 30min in a 10% wt phosphoric acid solution.

A cross-sectional image of the anodic alumina structure (prepared in oxalic acid following the steps just described) is shown in Figure 8.4: between 700 and 1000nm of porous alumina sits on top of ~30nm of Ti/TiO$_2$ on the Si wafer. Top surface SEM images of anodic alumina templates prepared in oxalic acid and sulfuric acid are shown in Figure 8.5. Because of the roughness in the starting Al film, the pores in the alumina may not all be perpendicular to the substrate. While these substrates are suitable for the investigation described here, better ordering can be achieved with thicker Al films, longer anodization times and longer polishing.

8.2.2 Fabrication of Etched Si Substrates

Etched Si substrates were made by reactive ion etching through a block copolymer etch mask; a method similar to that described in [107].

1. Preparation of etching mask: Self-assembled block copolymer films were developed on <100> Si substrates by Dr. Xin Zhang, a postdoctoral fellow in Prof. Robert Briber's group at UMD, as follows. Poly (styrene-b- 4-vinyl pyridine) (PS-b-P4VP) block copolymer with 175-b-64 kDa molecular weight and poly (4-vinyl pyridine) (P4VP) homopolymer with 5.1 kDa molecular weight were purchased from Polymer Source Inc. One part 1%wt P4VP homopolymer in isopropanol and three parts 1.333%wt PS-b-P4VP block copolymer swollen in dioxane are combined and shaken until dissolved. This solution is spin-coated onto <100> Si substrates at 2000 rpm with a 1s ramp to achieve a 50nm thick film. Left in a tetrahydrofuran vapor environment for more than 12 hours, the block copolymer self-assembles into a hexagonal arrangement of P4VP cylinders in a polystyrene (PS) matrix. The homopolymer P4VP sequesters into the self-assembled P4VP cylinders. The "pores" can then be opened at the centers of the P4VP cylindrical domains by soaking the film in ethanol, which dissolves the homopolymer. A schematic of this structure is shown in Figure 8.6.
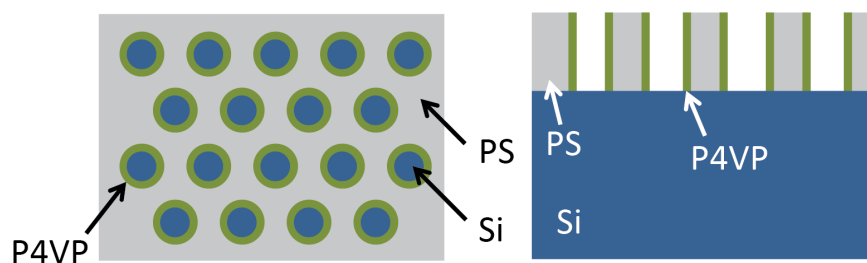

Figure 8.6: Top surface (left) and cross-section (right) schematic of the self-assembled block copolymer mask after dissolving the homopolymer. The pores, exposing the Si substrate (blue) underneath, are at the center of the P4VP cylindrical domains (green).

A 50nm PS mask could not withstand the etching conditions for the duration required for the pore depths desired in this study (>250nm), so the PS mask was coated with a thin (~5nm) Cr film using an angled deposition technique. The angled deposition technique allows preferential deposition on the top surface and the inner walls of the pores, but not on the bottom of the pores. The Si can then be patterned using the more resistant polymer/Cr bilayer as a mask.

2. Etching pores into the Si: The Si was etched in the Oxford Plasmalab System 100 Inductively Coupled Plasma etcher in the Fablab. Etching is done with the substrate at a temperature of 20°C, a pressure of 10mTorr and an ICP power of 750W. The C_4F_8 and SF_6 gas flow rates are 24 and 16sccm, respectively. With these process conditions, the vertical etch rate is close to 2nm/sec; an etch time of 3min consistently yields pore depths of ~350nm.
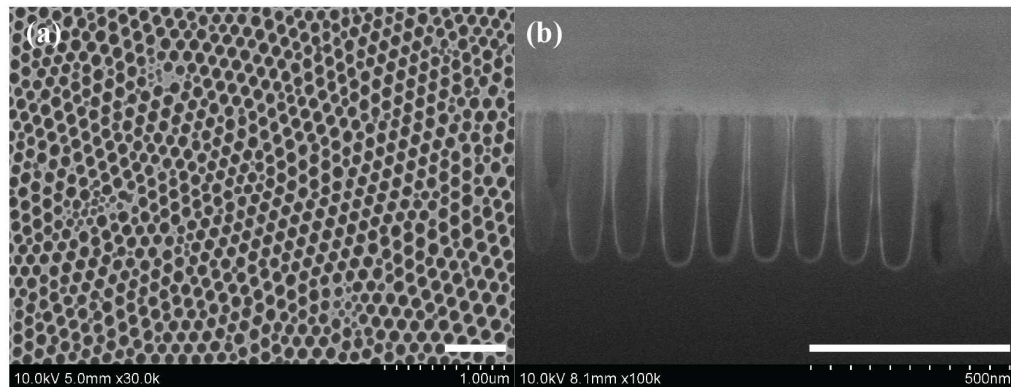

Figure 8.7: (a) Top surface and (b) cross-sectional SEM images of etched Si substrates fabricated using the block copolymer/Cr etch mask. Scale bar: 500nm.

3. Removal of the mask: The Cr is removed in a 1020 Chromium Etchant bath (Transene Company, Inc.), and the remaining PS is then removed by baking at 450°C in air and sonicating in toluene. Top surface and cross-sectional SEM images of an etched Si substrate fabricated in this way are shown in Figure 8.7. The average pore size is ~90nm and the pore walls are ~10nm thick.

8.2.3 Porous $Bi_{2-x}Sb_xTe_3$ Thin Films

In this section, we report the fabrication of porous $Bi_{2-x}Sb_xTe_3$ thin films via pulsed laser deposition on porous substrates. To determine the effect of porosity on the film characteristics, deposition is done on two substrates simultaneously: (1) a <100> Si substrate and (2) a porous substrate (either anodic alumina or etched Si). These 2 substrates are placed symmetrically about the optimal position on the substrate holder to ensure similar deposition rates. The pairs of films were deposited using a laser
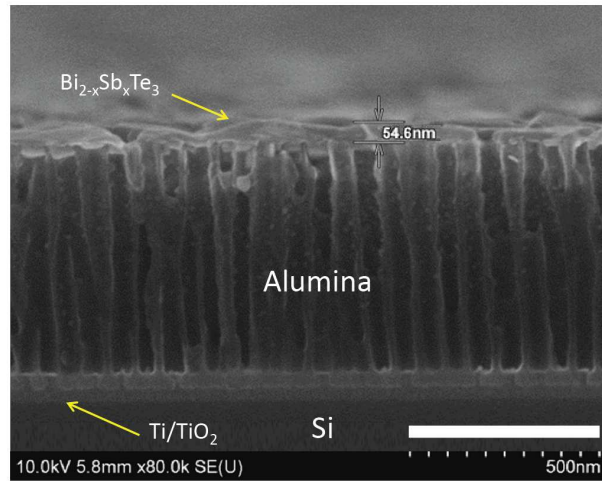

Figure 8.8: Cross-sectional SEM image of a porous $Bi_{2-x}Sb_xTe_3$ film on top of the alumina template. The Si substrate and Ti/TiO$_2$ adhesion layer are also labeled. Scale bar: 500nm.

power of 1.6W and background pressure of 2mTorr, and annealed at a temperature and pressure of 375°C and 2mTorr. A cross-sectional SEM image of a porous $Bi_{2-x}Sb_xTe_3$ film on an anodic alumina template is shown in Figure 8.8. The bright contrast towards the top of the alumina indicates that some $Bi_{2-x}Sb_xTe_3$ has deposited inside of the pores. The pulsed laser deposited material typically penetrates <250nm into the pores and does not form a continuous film through the bottom of the pores. The thickness of the porous films is measured from the top surface of the alumina (for example, for the film in Figure 8.8 the thickness is estimated to be 55nm), ignoring the coating on the pore walls.

SEM images of as-deposited and 15hr-annealed porous and dense films are compared in Figure 8.9. As-deposited, the porous films conform well to the underlying alumina template. The pores in the template lead to pores in the deposited $Bi_{2-x}Sb_xTe_3$ thin films. With annealing, the grains grow and appear more faceted. A similar transformation is seen in the dense films.

The XRD spectra of dense and porous films annealed in Te vapor for 0 to 15hrs are compared in Figure 8.10. The dense films show the now-familiar transformation from disordered to crystalline morphology with annealing (from blue to red) as was demonstrated in Sect. 7.5, although this set of films does not show strong texturing. The porous films show an improvement in crystallinity with annealing, with peaks generally increasing in intensity. Consistently, however, the XRD spectra of dense and porous films deposited simultaneously (shown as the same color in the two plots in Figure 8.10) indicate *different phases* present in the two films. The spectra from the dense films always indicate the presence of some amount
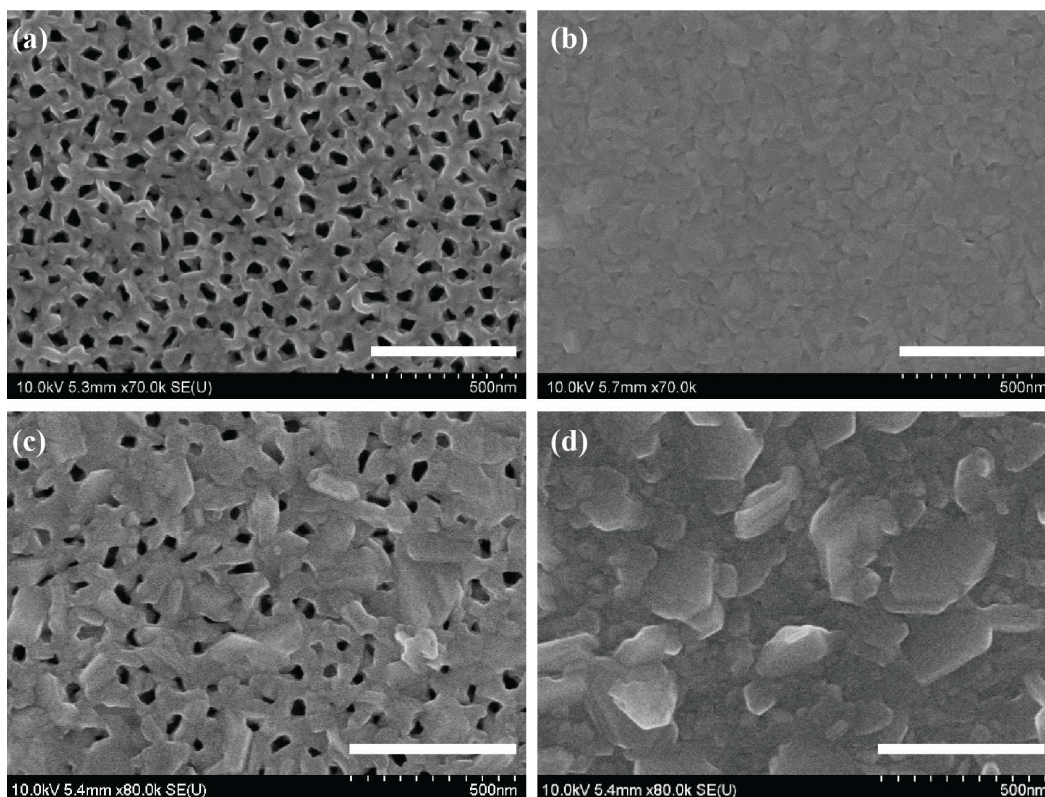
Figure 8.9: SEM images of an as-deposited (a) porous film on anodic alumina and (b) dense film on Si are compared with an annealed (c) porous film and (d) dense film. The deposition time was 26min. The films were annealed for 15hrs in a Te vapor. All images were taken at a magnification of 70-80kx. Scale bar: 500nm.

of the disordered phase. The porous films, on the other hand, do not contain any of the disordered phase. This result holds true independent of annealing time, though the structures of the two films become similar (i.e. crystalline) after 15hrs annealing. We note that while the XRD spectra in Figure 8.10 are from films annealed in Te vapor, porous and dense films annealed in N_2 show the same differences in structure. These results indicate that there is a fundamental difference between the depositions on the two substrates which leads to different film structures.

We proposed several possibilities for the source of the difference between the deposited films. These hypotheses were tested by depositing on a range of substrates.

For this investigation, all films were annealed under Te vapor for 1hr (from Figure 8.10, this is the annealing time for which the structures of porous and dense films are most different).
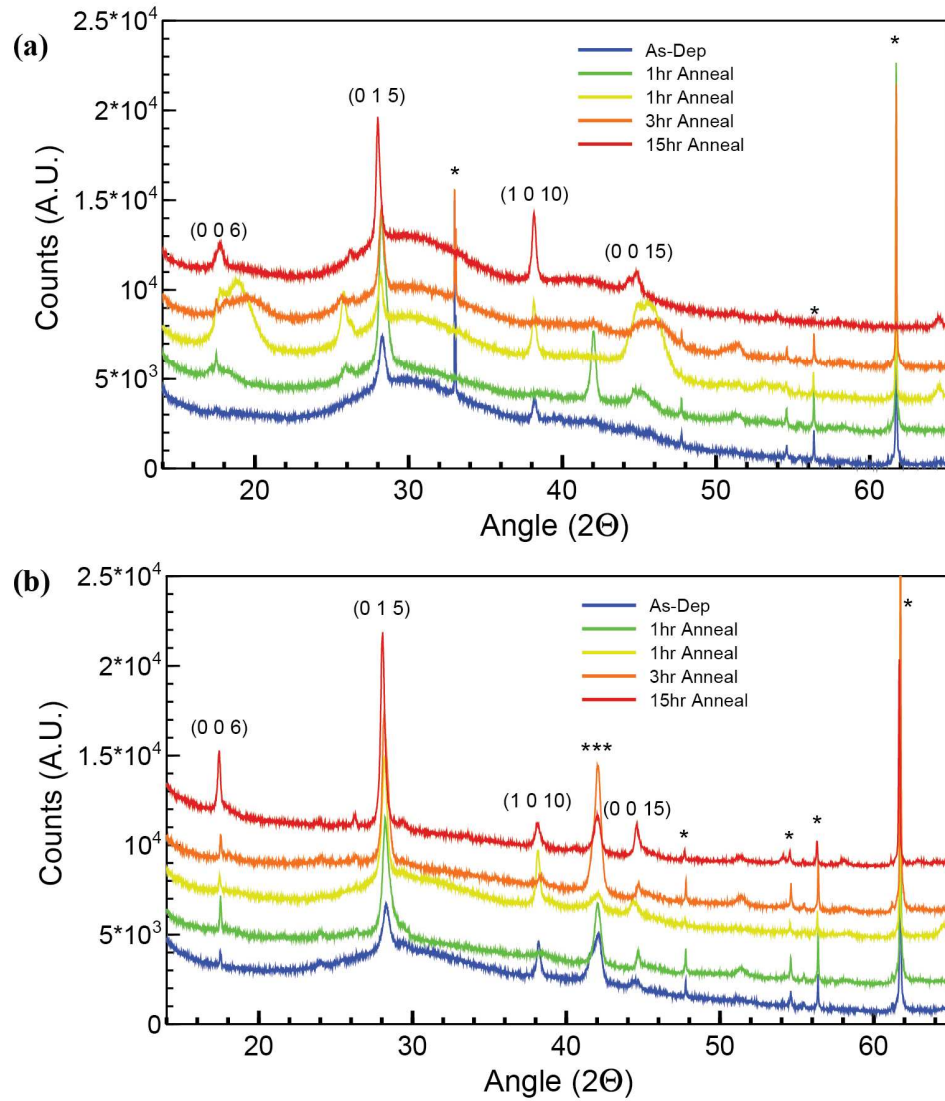

Figure 8.10: XRD spectra from (a) dense and (b) porous films annealed for various lengths of time. $Bi_{2-x}Sb_xTe_3$ peaks are identified and Si peaks are marked as *. The *** peak frequently seen in depositions on alumina is unidentified.

Hypothesis #1: The Si substrate and the anodic alumina template have very different thermal conductivities. A difference in the temperature of the substrate surface could lead to differences in the structure of the deposited films, as mentioned above in Sect. 7.4.1. We tested this hypothesis by depositing $Bi_{2-x}Sb_xTe_3$ on (1) a quartz slide (a low thermal conductivity dense material) and (2) an anodic alumina template coated with amorphous carbon (higher thermal conductivity). The film deposited on quartz has the same crystal structure as *dense* films on Si (showing little or no disordered phase), and the film deposited on carbon-coated anodic alumina has the same crystal structure as other *porous* films on anodic alumina. Thus, the thermal conductivity of the substrate is not the controlling factor.

Hypothesis #2: We investigated whether the surface chemistry of the substrate determined the crystal structure of the deposited films. Depositions on <111> Si, which show a mix of disordered and crystalline phases similar to films on <100> Si, indicate that there is no preference for the orientation of the wafer. In addition, Si substrates and anodic alumina templates were coated with thin layers of (1) amorphous carbon (grown by chemical vapor deposition) and (2) amorphous Al_2O_3 (grown by sputtering) prior to pulsed laser deposition. In both cases, the crystal structure of the porous and dense films differed, with more of the disordered phase found in the dense films.

We therefore propose that the disordered phase is less likely to form on the porous substrates due to the nanoscale morphology of the surface. We investigated the effect of the nanoscale porosity on the crystal structure by comparing porous films deposited on anodic alumina with pore sizes of 30nm, 60nm and 200nm. These

templates are alumina anodized in sulfuric acid, alumina anodized in oxalic acid and a commercially available Whatman Anodisc, respectively.

Typical depositions on anodic alumina or porous Si with pores larger than 60nm in diameter are 26min long, yielding ~100nm thick films in which the pores are still exposed. For 30nm pores, the deposition time must be shortened. Top surface and cross-sectional SEM images of 26min (left) and 11min (right) depositions on a "small-pore" anodic alumina template are shown in Figure 8.11. Interestingly, if the deposition is too long and the pores are completely covered, the effect of substrate is
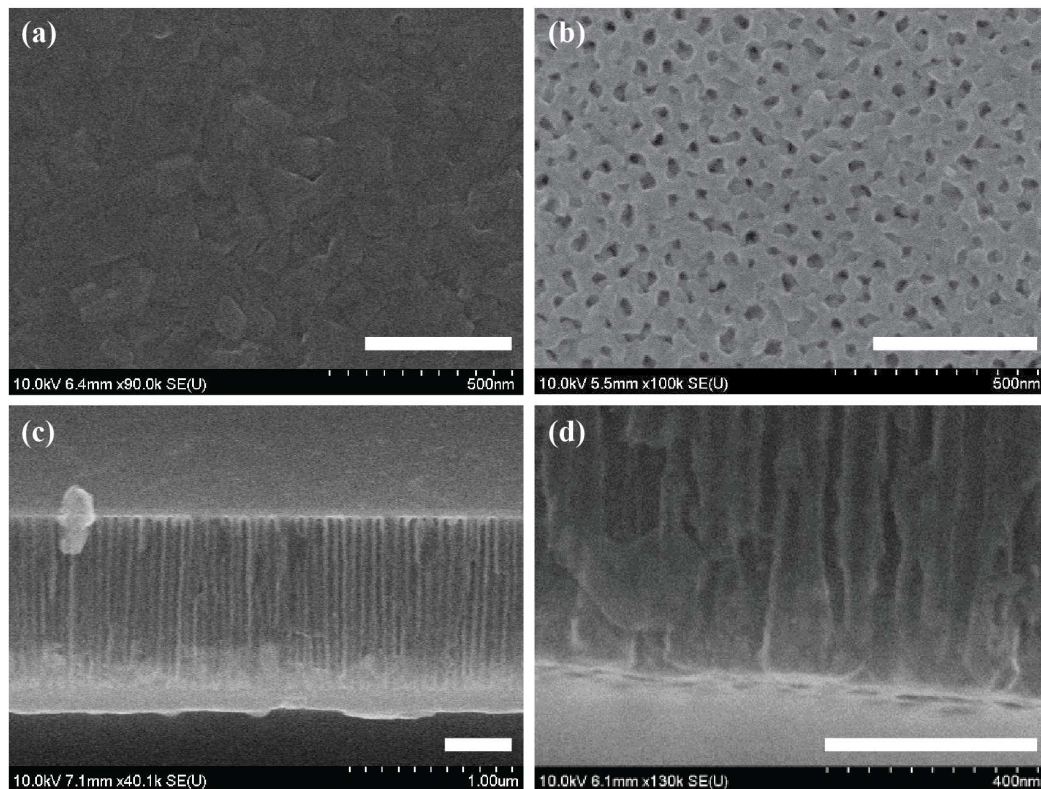
Figure 8.11: SEM images of a 26min deposition (left) and an 11min deposition (right) on anodic alumina with 30nm pores. The top images were taken at 90-100kx. Scale bar: 400nm.
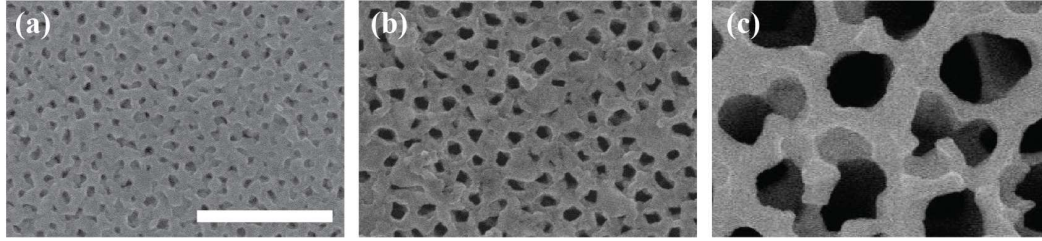
Figure 8.12: Top surface SEM images of $Bi_{2-x}Sb_xTe_3$ films deposited on substrates with a range of pore sizes: (a) 30nm porous alumina, (b) 60nm porous alumina, (c) 200nm Whatman Anodisc. Scale bar: 500nm.

lost—the films deposited on alumina and Si have nearly identical XRD spectra.

Top surface SEM images of films deposited on substrates with the range of pore sizes 30-200nm are compared in Figure 8.12. XRD data shows that if the pores are open, independent of the size of the pores, the porous films do not contain the disordered phase.

A summary of these experiments is given in Table XV.

Table XV. Summary of the structure of films deposited on a range of substrates. "X" and "D" indicate crystalline and disordered phases, respectively. Porous substrates are highlighted, with darker gray indicating the templated $Bi_{2-x}Sb_xTe_3$ film is porous and lighter gray indicating the pores in the $Bi_{2-x}Sb_xTe_3$ film were closed.

Substrate	Structure
Anodic alumina, 30nm (pores in BiSbTe film *open*)	X
Anodic alumina, 60nm	X
Anodic alumina (60nm) + C	X
Anodic alumina (60nm) + a-Al$_2$O$_3$	X
Etched Si (75nm)	X
Anodic alumina, 200nm	X
Etched Si, 60nm (pores in BiSbTe film *closed*)	D+X
Anodic alumina, 30nm (pores in BiSbTe film *closed*)	D+X
<100> Si	D+X
<111> Si	D+X
Quartz	D+X
<100> Si + C	D+X
<100> Si + a-Al$_2$O$_3$	D+X

As a whole, the depositions done on a range of substrates indicate that the crystal structure of the deposited films depends primarily on whether or not the substrate is porous (and is not strongly controlled by the thermal conductivity or surface chemistry or orientation of the substrate). It therefore seems likely that the nanostructured morphology of the porous templates limits or controls diffusion during grain growth in the deposited $Bi_{2-x}Sb_xTe_3$ films in such a way that the disordered phase is less likely to form.

We will briefly present a comparison of the compositions and transport properties of the porous and dense thin films deposited in this study. However, because the structures of the two types of films are consistently different, these results cannot be used to make any conclusions about the effect of porosity alone.

The M:Te ratios measured for dense and porous films annealed in Te vapor are shown as a function of annealing time in Figure 8.13. The composition of the dense films was measured by ICP-OES, while the composition of the porous films was measured by EDX. We note that while we expect there to be an error in the compositions of porous films measured by EDX (see Sect. 7.3.2), this error is likely to be different from that of the dense films. This is simply because (for porous films on anodic alumina) there is a difference in the composition of the underlying substrate. In general, the M:Te ratio decreases down to the target value with annealing; as detailed in Sect. 7.5.2, however, the data is scattered for samples annealed for short periods of time.
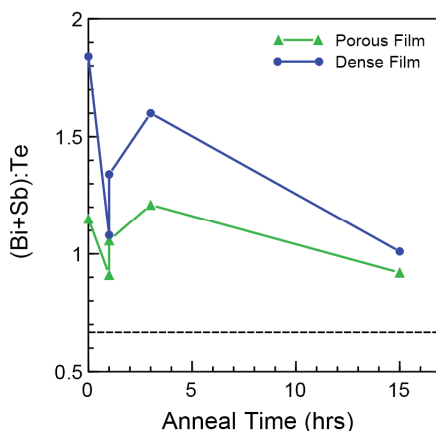

Figure 8.13: M:Te atomic ratios for the porous films on anodic alumina and dense films on Si as a function of annealing time. Data for the porous films was measured using EDX, and data for the dense films was measured using ICP-OES.
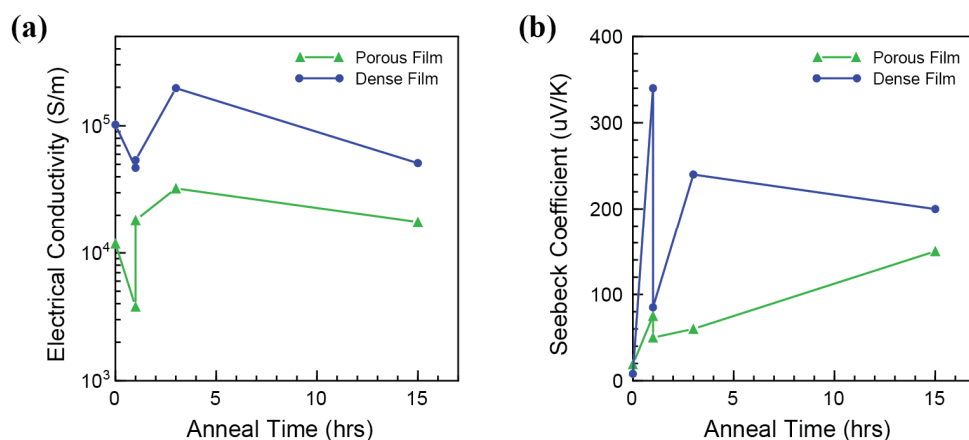
Figure 8.14: (a) Electrical conductivity and (b) Seebeck coefficient as a function of annealing time for the set of porous and dense films annealed in Te vapor.

The transport properties (electrical conductivity and Seebeck coefficient) of the porous films are measured in the same way as described for the dense films. The fill factor is ignored for calculation of the conductivity of the porous films. Good contact is easily achieved, despite the induced porosity and roughness in the films. The electrical conductivity and Seebeck coefficient for this set of porous and dense films are given as a function of annealing time in Figure 8.14. The electrical conductivities of both film morphologies do not change significantly with annealing, and the conductivities of the dense films are consistently higher than those of the porous films. The Seebeck coefficients of the porous and dense films both increase by a factor of ~10 with annealing, with the Seebeck of dense films typically larger in magnitude. The power factor value of both porous and dense films generally increases with annealing time (Figure 8.15), and the power factor of dense films is consistently higher than that of porous films.
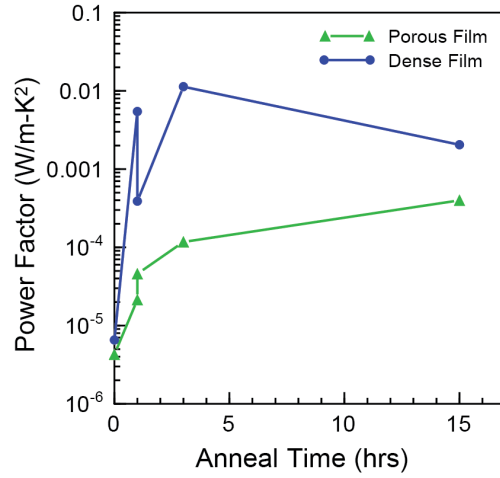
Figure 8.15: Power factor value as a function of annealing time for porous and dense films annealed in Te vapor.

8.3 _Top-Down Patterning of Porous Bi$_{2-x}$Sb$_x$Te$_3$ Thin Films_

In the previous section, we found that porous films fabricated using a templated deposition technique consistently form a different crystal structure than films deposited on flat Si substrates. In the absence of an adequate reference, we can make no assertions about the effect of porosity alone. Top-down patterning of dense films may therefore be a better route for future experiments. We have carrier out preliminary work on using ion milling to etch pores into dense Bi$_{2-x}$Sb$_x$Te$_3$ films with self-assembled block copolymer masks. When the PS-P4VP block copolymer-homopolymer film was used as a mask (see Sect. 8.2.2), we found that the structure does not form through-holes when spun on Bi$_{2-x}$Sb$_x$Te$_3$ (Figure 8.16). This prevents the underlying Bi$_{2-x}$Sb$_x$Te$_3$ film from being patterned. A better mask structure is therefore required for top-down patterning. One potential solution is to protect the top surface of the PS mask with Cr (as was done to etch pores into Si), although the post-
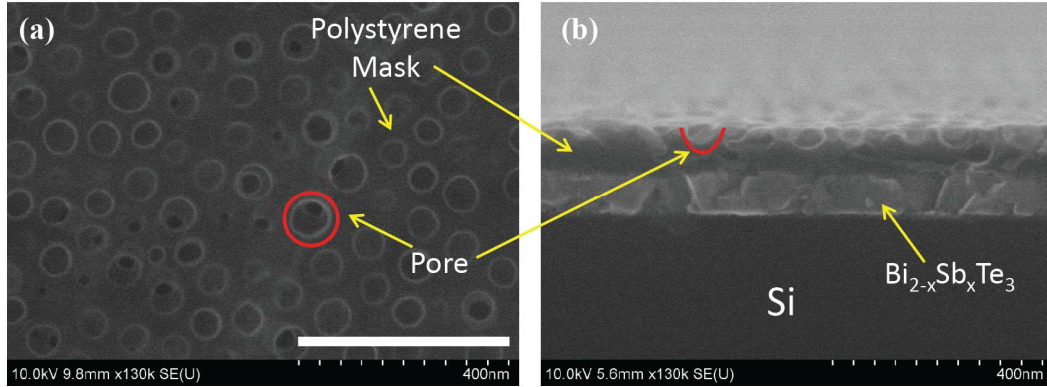
Figure 8.16: Top surface and cross-sectional SEM images of a $Bi_{2-x}Sb_xTe_3$ film covered with a block copolymer mask after ion milling. Scale bar: 400nm.

patterning removal of the Cr, crucial for accurate transport measurements, may prove difficult. One alternative to block copolymer patterning not yet explored is using e-beam lithography to pattern a PMMA mask on top of the dense $Bi_{2-x}Sb_xTe_3$ films.

8.4 Conclusions

In this chapter, we reported a templated deposition approach to fabricating porous $Bi_{2-x}Sb_xTe_3$ films on anodic alumina templates. We find that while the porous films show a similar enhancement in the thermoelectric transport properties with annealing in a Te vapor, the crystal structure of the porous films consistently differs from that of the dense films. After deposition on a wide range of additional substrates, we propose that these differences arise because the nanostructured surface of the porous substrates limits grain growth. Because of this result, we cannot isolate the effect of nanoscale porosity on the transport properties. This work indicates that future investigation should focus on top-down patterning of dense $Bi_{2-x}Sb_xTe_3$ films.

Chapter 9 Summary and Future Work

9.1 Conclusions

In this work, we addressed the discrepancy between experimental and modeling work in the field of nanostructured thermoelectric materials. We developed new models for calculating the thermoelectric transport properties of nanowires and thin films. Results calculated using these models, in contrast with the original modeling work of Hicks and Dresselhaus, indicate that the power factor of nanostructures (1) has a non-monotonic dependence on size and (2) falls below the bulk value for most of the size range of experimental interest ($w > 20$nm). The latter result is supported by a vast majority of experimental work in the field of nanostructured thermoelectric materials. These phenomena are the result of fundamental changes in the electron density-of-states as the size is varied. For small sizes (typically <20nm), quantum confinement is strong and the power factor increases with decreasing size. For larger sizes, however, the power factor increases up to the bulk value with increasing size. This is due to weakening of confinement, which causes the quantized energy levels to become closer together and the magnitude of the density-of-states to increase. These qualitative trends were seen in each system investigated, regardless of the system dimensionality, the material of interest or the temperature.

We used the analytical forms of the transport properties of nanostructured systems to derive universal scaling relationships between the thermoelectric power

factor and various system parameters (material, temperature and size). These universal curves (1) further prove that the non-monotonic size-dependence of the power factor is a fundamental result of these models and (2) allow us to determine the power factor value of nanostructures of any single-carrier isotropic material with no additional computational effort. A new criteria for evaluation of the effectiveness of confinement, $\frac{\hbar^2}{m^* w^2} > 5k_B T$, is proposed based on the features of the universal curves. These universal curves will therefore serve as a guide for future experimental work in the field of nanostructured thermoelectrics. Specifically, these universal curves can be used to determine the size-range in which the expected decrease in the power factor is more than compensated by a decrease in the thermal conductivity.

The principle result of this theoretical work is that, in general, the power factor of simple nanostructures is lower than the bulk value. More complex nanostructuring techniques must therefore be investigated. We explored one such technique, the introduction of nanoscale through-pores, both in terms of modeling and experimental implementation. Transport property calculations were done for nanostructured systems in which the carrier scattering time is a function of energy. We found that mechanisms which preferentially scatter low-energy electrons ("energy filtering") lead to the highest power factor values. In fact, an improvement in the power factor is seen with the addition of such a scattering mechanism even when the overall scattering rate increases.

These conclusions were then evaluated experimentally. Porous $Bi_{2-x}Sb_xTe_3$ thin films were fabricated via pulsed laser deposition onto porous substrates. We find that because the deposited porous films show different structure than dense films

deposited on planar substrates, these results cannot be used to make assertions about the effects of nanoscale porosity alone.

9.2 Future Work

The results of the modeling work described here point to the difficulty in realizing improvements in the thermoelectric power factor by reducing the system size. It is therefore crucial that future theoretical and experimental work on this project focus on whether or not improvements in the power factor can be realized with complex nanostructuring techniques.

1. *Transport models for complex nanostructures:* The models used here to calculate the transport properties of nanostructures and bulk systems in which low-energy electrons are preferentially scattered can only give a rough estimate for the effects of nanoscale grain boundaries on the magnitude of the power factor of nanoporous or nanocomposite systems. Significant work remains in order to (a) better model such complex nanostructured systems and (b) to determine optimized conditions (in terms of suitable materials choices and nanoparticle/pore size and density) for the largest improvements in the power factor.

2. *Top-down patterning of porous thin films:* The templated deposition technique developed for the fabrication of porous $Bi_{2-x}Sb_xTe_3$ thin films is not suitable for determining the fundamental effects of nanoscale porosity on thermoelectric transport. The results of the experimental work presented here indicate that future work should focus on top-down patterning of dense films as a means for answering this question. We note, however, that once the scientific questions are answered with a top-down process, the templated deposition technique could be reinstated as a

means to fabricate porous thin films with high power factor values in a single processing step.

Chapter 10 Appendix

This appendix includes a description of the front panel of the PLD-TE system described in Sect. 6.3, and a list of components used in deposition processes. During deposition, the process parameters of the dual PLD-TE system are controlled using an integrated control rack shown in Figure 10.1. The front panel was designed and built by Blue Wave Semiconductors and includes (A) the deposition controller for thermal evaporation, (B) the control panel for the turbo pump, (C) the pressure readout, (D) the gas flow controller, (E) the substrate temperature controller and (F) the power
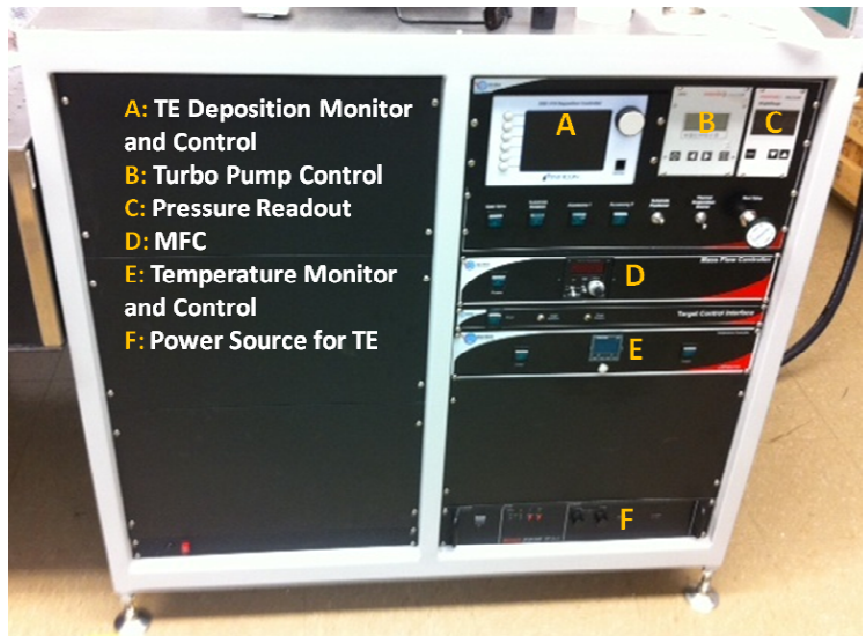

Figure 10.1: Front panel of the control racks of the PLD-TE system.

source for thermal evaporation. Other switches on the front panel control the power for the roughing pump, the gate valve, position and rotation of the substrate holder, selection of the thermal evaporation source and power for the target carousel. In addition to the front panel, most processing parameters are controlled and recorded using LabView programs.

The function and part number of the components within the front panel and the deposition chamber are listed in the table below. Where applicable, the description is followed by the letter designated in Figure 10.1.

Table XVI. Part numbers of various components in the PLD-TE system.

Purpose	Description	Manufacturer and Part Number
Pressure of chamber	Roughing pump	Pfeiffer DUO035
	Turbo pump	Pfeiffer HiPace 400
	Turbo pump control (B)	Pfeiffer TC400
	Pressure gauge	Pfeiffer PKR251
	Pressure readout (C)	Pfeiffer PKR251 Control Unit
	Mass flow controller (D)	MKS MFC with 167 Readout Module
Substrate temperature	PID controller for heater (E)	Eurotherm 2416
Thermal evaporation	Deposition control (A)	INFICON SQC-310
	DC power supply (F)	Sorensen DCS8-350E
	Quartz crystal sensor	INFICON 008-010-G10
Pulsed laser deposition	532nm laser	Quantel Brilliant b
	Target carousel motor	Silverpak 23C

CAD drawings of various components of the PLD-TE system are given

below. These components were discussed in detail in Sect. 6.3.

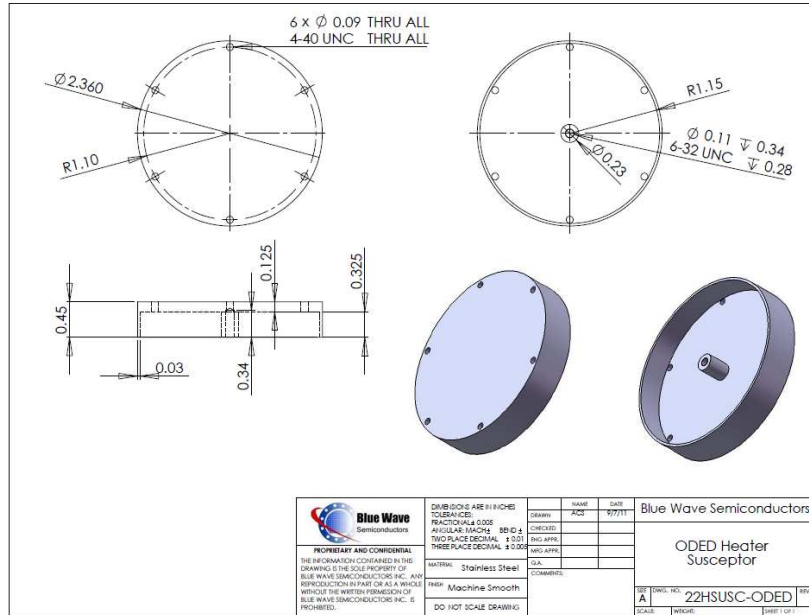Figure 10.2: CAD drawing: Deposition chamber.

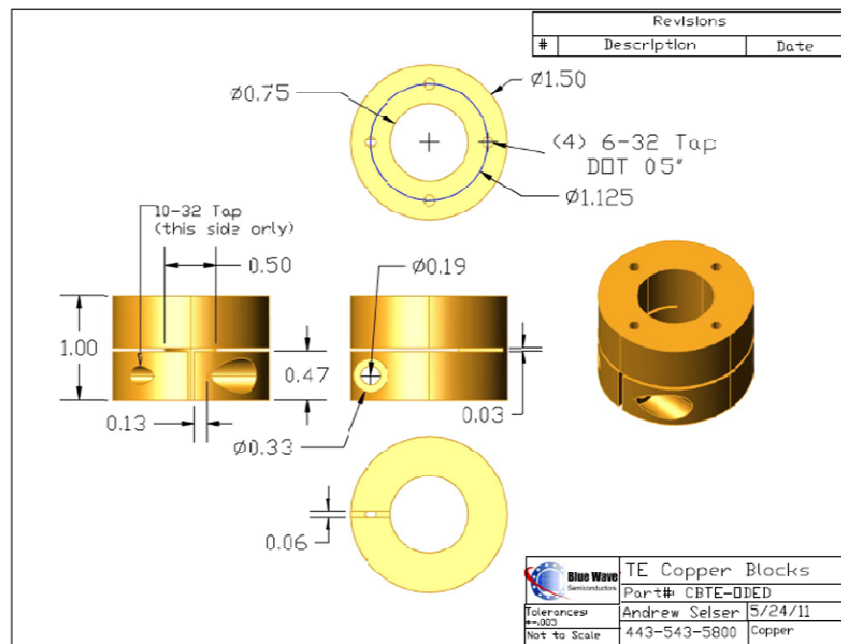Figure 10.3: CAD drawing: Substrate holder.

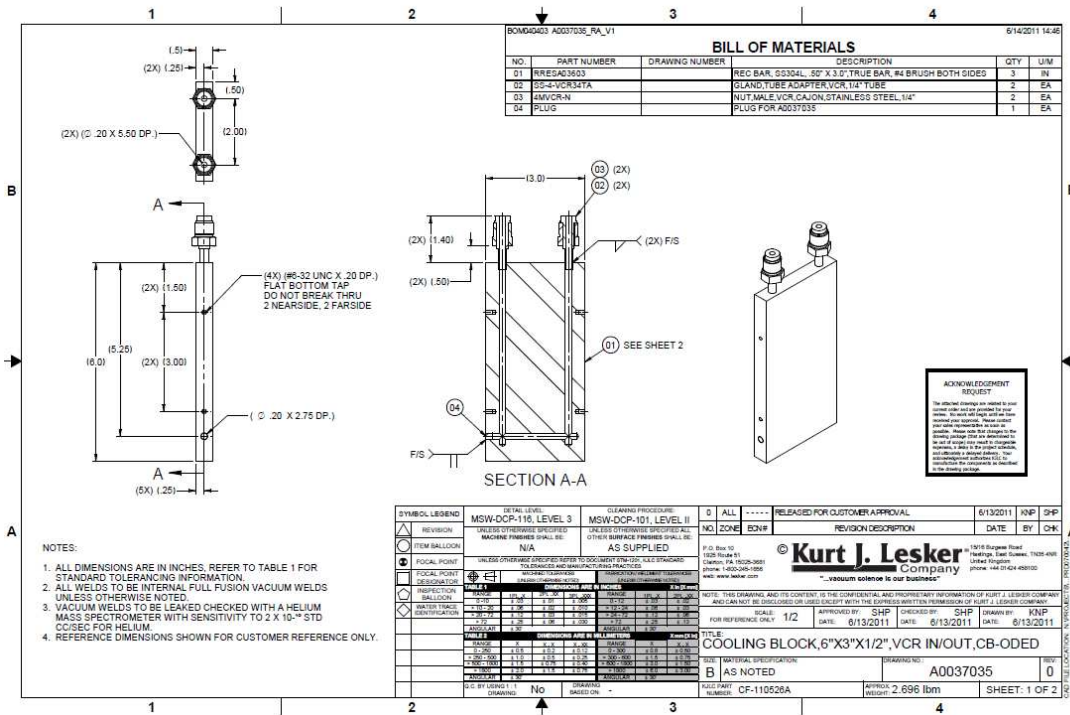Figure 10.4: CAD drawing: Cu block in electrodes for thermal evaporation.

Figure 10.5: CAD drawing: Water cooling unit that separates target carousel from thermal evaporation electrodes.

Bibliography

1.   Eason, R., *Pulsed Laser Deposition of Thin Films: Applications-Led Growth of Functional Materials*. 2006, Hoboken, New Jersey: John Wiley & Sons, Inc.

2.   Snyder, G.J. and E.S. Toberer, *Complex thermoelectric materials.* Nature Materials, 2008. **7**(2): p. 105-114

3.   Rabin, O., *Bismuth Nanowire and Antidot Array Studies Motivated by Thermoelectricity.* (2004), Doctor of Philosophy, Chemistry, Massachusetts Institute of Technology.

4.   Mingo, N., *Thermoelectric figure of merit and maximum power factor in III–V semiconductor nanowires.* Applied Physics Letters, 2004. **84**(14): p. 2652

5.   Lee, H., et al., *Effects of nanoscale porosity on thermoelectric properties of SiGe.* Journal of Applied Physics, 2010. **107**(9): p. 094308.

6.   Harman, T.C., et al., *Thermoelectric quantum-dot superlattices with high ZT.* Journal of Electronic Materials, 2000. **29**(1): p. L1-L2

7.   Bos, J., et al., *Structures and thermoelectric properties of the infinitely adaptive series (Bi2)m(Bi2Te3)n.* Physical Review B, 2007. **75**(19).

8.   Hochbaum, A.I., et al., *Enhanced thermoelectric performance of rough silicon nanowires.* Nature, 2008. **451**(7175): p. 163-167.

9.   Dauscher, A., A. Thomy, and H. Scherrer, *Pulsed laser deposition of Bi2Te3 thin films.* Thin Solid Films, 1996. **280**(1–2): p. 61-66

10.   Zide, J.M., et al., *Thermoelectric power factor in semiconductors with buried epitaxial semimetallic nanoparticles.* Applied Physics Letters, 2005. **87**(11): p. 112102.

11.   Rostek, R., V. Sklyarenko, and P. Woias, *Influence of vapor annealing on the thermoelectric properties of electrodeposited Bi2Te3.* Journal of Materials Research, 2011. **26**(15): p. 1785-1790.

12.   Russo, V., et al., *Raman spectroscopy of Bi-Te thin films.* Journal of Raman Spectroscopy, 2008. **39**(2): p. 205–210

13.   Tang, J., et al., *Holey Silicon as an Efficient Thermoelectric Material.* Nano Letters, 2010. **10**(10): p. 4279-4283.

14.   Mohammad, R., Ş. Katırcıoğlu, and M. El-Hasan, *The electronic band structure of InN, InAs and InSb compounds.* Journal of Materials Science, 2008. **43**(8): p. 2935-2946.

15.   Li Bassi, A., et al., *Thermoelectric properties of Bi–Te films with controlled structure and morphology.* Journal of Applied Physics, 2009. **105**(12): p. 124307.

16.   Noh, H.J., et al., *Spin-orbit interaction effect in the electronic structure of Bi 2 Te 3 observed by angle-resolved photoemission spectroscopy.* Europhysics Letters, 2008. **81**(5): p. 57006.

17.   Joshi, G., et al., *Enhanced Thermoelectric Figure-of-Merit in Nanostructured p-type Silicon Germanium Bulk Alloys.* Nano Letters, 2008. **8**(12): p. 4670-4674.

18. Hicks, L.D. and M.S. Dresselhaus, *Thermoelectric figure of merit of a one-dimensional conductor.* Physical Review B, 1993. **47**(24): p. 16631.

19. Hicks, L.D. and M.S. Dresselhaus, *Effect of quantum-well structures on the thermoelectric figure of merit.* Physical Review B, 1993. **47**(19): p. 12727.

20. *InSb Band structure and carrier concentration.* 2013; Available from: http://www.ioffe.rssi.ru/SVA/NSM/Semicond/InSb/bandstr.html.

21. Yang, C. and S. Li, *Size-Dependent Lattice Thermal Conductivity of Nanostructured Bulk Semiconductors.* Journal of Electronic Materials, 2011. **40**(5): p. 953-956.

22. *Report on the First Quadrennial Technology Review*, in *Quadrennial Technology Review*, U.S.D.o. Energy, Editor. September 2011.

23. Rowe, D.M. and C.M. Bhandari, *Modern Thermoelectrics.* 1983: Reston Publishing Company.

24. Nolas, G.S., J. Sharp, and J. Goldsmid, *Thermoelectrics: Basic Principles and New Materials Developments.* 2001: Springer.

25. Venkatasubramanian, R., et al., *Thin-film thermoelectric devices with high room-temperature figures of merit.* Nature, 2001. **413**(6856): p. 597-602

26. Harman, T.C., et al., *Quantum Dot Superlattice Thermoelectric Materials and Devices.* Science, 2002. **297**(5590): p. 2229-2232

27. Poudel, B., et al., *High-Thermoelectric Performance of Nanostructured Bismuth Antimony Telluride Bulk Alloys.* Science, 2008. **320**(5876): p. 634-638.

28. Bux, S.K., et al., *Nanostructured Bulk Silicon as an Effective Thermoelectric Material.* Advanced Functional Materials, 2009. **19**(15): p. 2445-2452

29. Boukai, A.I., et al., *Silicon nanowires as efficient thermoelectric materials.* Nature, 2008. **451**(7175): p. 168-171

30. Weber, L. and E. Gmelin, *Transport properties of silicon.* Applied Physics A Solids and Surfaces, 1991. **53**(2): p. 136-140

31. Harman, T.C., et al., *Nanostructured thermoelectric materials.* Journal of Electronic Materials, 2005. **34**(5): p. L19-L22

32. Jeong, C., R. Kim, and M. Lundstrom, *On the Best Bandstructure for Thermoelectric Performance.* http://arxiv.org/abs/1103.1274, 2011.

33. Madsen, G.K.H., *Automated Search for New Thermoelectric Materials: The Case of LiZnSb.* Journal of the American Chemical Society, 2006. **128**(37): p. 12140-12146

34. Broido, D.A. and N. Mingo, *Theory of the thermoelectric power factor in nanowire-composite matrix structures.* Physical Review B, 2006. **74**(19): p. 195325

35. Broido, D.A. and T.L. Reinecke, *Theory of thermoelectric power factor in quantum well and quantum wire superlattices.* Physical Review B, 2001. **64**(4): p. 045324

36. Cui, Y., et al., *Doping and Electrical Transport in Silicon Nanowires.* The Journal of Physical Chemistry B, 2000. **104**(22): p. 5213-5216

37. Ford, A.C., et al., *Diameter-Dependent Electron Mobility of InAs Nanowires.* Nano Letters, 2009. **9**(1): p. 360-365

38. Koga, T., et al., *Mechanism of the enhanced thermoelectric power in (111)-oriented n-type PbTe/Pb_{1-x}Eu_{x}Te multiple quantum wells.* Physical Review B, 1999. **60**(20): p. 14286

39. Ashcroft, N.W. and N.D. Mermin, *Solid state physics.* 1976: Holt, Rinehart and Winston.

40. Broido, D.A. and T.L. Reinecke, *Thermoelectric transport in quantum well superlattices.* Applied Physics Letters, 1997. **70**(21): p. 2834

41. Broido, D.A. and T.L. Reinecke, *Thermoelectric power factor in superlattice systems.* Applied Physics Letters, 2000. **77**(5): p. 705

42. Kane, E.O., *Band structure of indium antimonide.* Journal of Physics and Chemistry of Solids, 1957. **1**(4): p. 249-261

43. Hicks, L.D., *The Effect of Quantum-Well Superlattices on the Thermoelectric Figure of Merit.* (1996), Ph.D., Physics, Massachusetts Institute of Technology.

44. Lin, Y.-M., X. Sun, and Dresselhaus, *Theoretical investigation of thermoelectric transport properties of cylindrical Bi nanowires.* Physical Review B, 2000. **62**(7): p. 4610.

45. Lin, Y.-M., *Fabrication, Characterization and Theoretical Modeling of Te-doped Bi Nanowire Systems for Thermoelectric Applications* (2000), M.Sc., Electrical Engineering and Computer Science, Massachusetts Institute of Technology.

46. Yamaguchi, S., et al., *Thermoelectric properties and figure of merit of a Te-doped InSb bulk single crystal.* Applied Physics Letters, 2005. **87**(20): p. 201902.

47. Stradling, R.A. and R.A. Wood, *The temperature dependence of the band-edge effective masses of InSb, InAs and GaAs as deduced from magnetophonon magnetoresistance measurements.* Journal of Physics C: Solid State Physics, 1970. **3**(5): p. L94-L99

48. Madelung, O., *Semiconductors: Group IV Elements and III-V Compounds.* 1991: Springer-Verlag.

49. Cornett, J.E. and O. Rabin, *Thermoelectric figure of merit calculations for semiconducting nanowires.* Applied Physics Letters, 2011. **98**(18): p. 182104.

50. Levinshtein, M.E.a.R., S.L., *Handbook Series on Semiconductor Parameters,* ed. M.E. Levinshtein, Rumyantsev, S.L and Shur, M. Vol. 1. 1996, London: World Scientific.

51. Drabble, J.R. and A.J. Brammer, *The third-order elastic constants of indium antimonide.* Proceedings of the Physical Society, 1967. **91**(4): p. 959-964

52. Stuckes, A.D., *Thermal Conductivity of Indium Antimonide.* Physical Review, 1957. **107**(2): p. 427

53. Mingo, N. and D.A. Broido, *Lattice Thermal Conductivity Crossovers in Semiconductor Nanowires.* Physical Review Letters, 2004. **93**(24): p. 246106

54. Mingo, N., *Calculation of Si nanowire thermal conductivity using complete phonon dispersion relations.* Physical Review B, 2003. **68**(11): p. 113308

55. Rabin, O., Y.-M. Lin, and M.S. Dresselhaus, *Anomalously high thermoelectric figure of merit in Bi[sub 1−x]Sb[sub x] nanowires by carrier pocket alignment.* Applied Physics Letters, 2001. **79**(1): p. 81

56. Mingo, N., et al., *Predicting the Thermal Conductivity of Si and Ge Nanowires.* Nano Letters, 2003. **3**(12): p. 1713-1716

57. Cornett, J.E. and O. Rabin, *Universal scaling relations for the thermoelectric power factor of semiconducting nanostructures.* Physical Review B, 2011. **84**(20): p. 205410.

58. Nolas, G.S., J. Sharp, and H.J. Goldsmid, *Thermoelectrics: basic principles and new materials developments.* 2001: Springer

59. Zhou, J., et al., *Optimal Bandwidth for High Efficiency Thermoelectrics.* Physical Review Letters, 2011. **107**(22): p. 226601.

60. Fistul□, V.I.i., *Heavily doped semiconductors* 1969: Plenum Press.

61. Chattopadhyay, D. and H.J. Queisser, *Electron scattering by ionized impurities in semiconductors.* Reviews of Modern Physics, 1981. **53**(4): p. 745-768

62. Zawadzki, W. and W. Szymańska, *Elastic Electron Scattering in InSb‐Type Semiconductors.* physica status solidi (b), 1971. **45**(2): p. 415-432

63. Cornett, J.E. and O. Rabin, *Effect of the energy dependence of the carrier scattering time on the thermoelectric power factor of quantum wells and nanowires.* Applied Physics Letters, 2012. **100**(24): p. 242106 -242106-4.

64. Mahan, G.D. and J.O. Sofo, *The best thermoelectric.* Proceedings of the National Academy of Sciences of the United States of America, 1996. **93**(15): p. 7436 -7439

65. Minnich, A.J., et al., *Bulk nanostructured thermoelectric materials: current research and future prospects.* Energy & Environmental Science, 2009. **2**(5): p. 466

66. Vineis, C.J., et al., *Nanostructured Thermoelectrics: Big Efficiency Gains from Small Features.* Advanced Materials, 2010. **22**(36): p. 3970-3980

67. Zide, J.M.O., et al., *Demonstration of electron filtering to increase the Seebeck coefficient in In_{0.53}Ga_{0.47}As/In_{0.53}Ga_{0.28}Al_{0.19}As superlattices.* Physical Review B, 2006. **74**(20): p. 205335.

68. Heremans, J.P., C.M. Thrush, and D.T. Morelli, *Thermopower enhancement in PbTe with Pb precipitates.* Journal of Applied Physics, 2005. **98**(6): p. 063703-063703-6

69. Popescu, A. and L.M. Woods, *Enhanced thermoelectricity in composites by electronic structure modifications and nanostructuring.* Applied Physics Letters, 2010. **97**(5): p. 052102

70. Donetti, L., et al., *Influence of acoustic phonon confinement on electron mobility in ultrathin silicon on insulator layers.* Applied Physics Letters, 2006. **88**(12): p. 122108

71. Esseni, D. and E. Sangiorgi, *Low field electron mobility in ultra-thin SOI MOSFETs: experimental characterization and theoretical investigation.* Solid-State Electronics, 2004. **48**(6): p. 927-936

72. Gámiz, F., et al., *Electron mobility in extremely thin single-gate silicon-on-insulator inversion layers.* Journal of Applied Physics, 1999. **86**(11): p. 6269

73. Wang, T., T.H. Hsieh, and T.W. Chen, *Quantum confinement effects on low-dimensional electron mobility.* Journal of Applied Physics, 1993. **74**(1): p. 426

74. Huang, Y., et al., *Gallium Nitride Nanowire Nanodevices*. Nano Letters, 2002. **2**(2): p. 101-104.

75. Jin, S., M.V. Fischetti, and T.-w. Tang, *Modeling of electron mobility in gated silicon nanowires at room temperature: Surface roughness scattering, dielectric screening, and band nonparabolicity.* Journal of Applied Physics, 2007. **102**(8): p. 083715

76. Mingo, N., *Thermoelectric figure of merit of II–VI semiconductor nanowires.* Applied Physics Letters, 2004. **85**(24): p. 5986

77. Cui, Y., et al., *High Performance Silicon Nanowire Field Effect Transistors.* Nano Letters, 2003. **3**(2): p. 149-152

78. Hattori, J., et al., *Scaling consideration and compact model of electron scattering enhancement due to acoustic phonon modulation in an ultrafine free-standing cylindrical semiconductor nanowire.* Journal of Applied Physics, 2010. **107**(3): p. 033712

79. Scullin, M.L., et al., *Anomalously large measured thermoelectric power factor in Sr[sub 1−x]La[sub x]TiO[sub 3] thin films due to SrTiO[sub 3] substrate reduction.* Applied Physics Letters, 2008. **92**(20): p. 202113

80. Obara, H., et al., *Thermoelectric Properties of Bi2Te3-Based Thin Films with Fine Grains Fabricated by Pulsed Laser Deposition.* Japanese Journal of Applied Physics, 2009. **48**(8): p. 085506.

81. Ohtomo, A. and H.Y. Hwang, *Growth mode control of the free carrier density in SrTiO3-d films.* Journal of Applied Physics, 2007. **102**: p. 083704.

82. Nolas, G.S., J. Sharp, and J. Goldsmid, *Thermoelectrics: Basic Principles and New Materials Developments.* 2001: Springer. 93-94.

83. White, G.K. and M.L. Minges, *Thermophysical properties of some key solids: An update.* International Journal of Thermophysics, 1997. **18**(5): p. 1269-1327.

84. van der Pauw, L.J., *A method of measuring specific resistivity and Hall effect of discs of arbitrary shape.* Philips Res.Rep, 1958. **13**(1).

85. Rowe, D.M., *Thermoelectrics Handbook: Macro to Nano.* 2006, CRC Press.

86. Smith, M.J., R.J. Knight, and C.W. Spencer, *Properties of Bi2Te3-Sb2Te3 Alloys.* Journal of Applied Physics, 1962. **33**(7): p. 2186-2190

87. Bekebrede, W.R. and O.J. Guentert, *Lattice parameters in the system antimony telluride bismuth telluride.* Journal of Physics and Chemistry of Solids, 1962. **23**(7): p. 1023-1025.

88. Birkholz, U., *Untersuchung Der Intermetallischen Verbindung Bi2te3 Sowie Der Festen Losungen Bi2-Xsbxte3 Und Bi2te3-Xsex Hinsichtlich Ihrer Eignung Als Material Fur Halbleiter-Thermoelemente.* Zeitschrift Fur Naturforschung Part a-Astrophysik Physik Und Physikalische Chemie, 1958. **13**(9): p. 780-792.

89. Tritt, T.M., *Thermal Conductivity: Theory, Properties, and Applications.* 2004: Springer.

90. Goldsmid, H.J., A.R. Sheard, and D.A. Wright, *The performance of bismuth telluride thermojunctions.* British Journal of Applied Physics, 1958. **9**(9): p. 365-370.

91. Drašar, Č., et al., *Transport coefficients of titanium-doped Sb2Te3 single crystals.* Journal of Solid State Chemistry, 2005. **178**(4): p. 1301-1307.

92. Wright, D.A., *Materials for direct-conversion thermoelectric generators.* Metallurgical Reviews, 1970. **15**(14): p. 147-160.

93. Bailini, A., et al., *Pulsed laser deposition of Bi2Te3 thermoelectric films.* Applied Surface Science, 2007. **254**(4): p. 1249-1254

94. Makala, R.S., K. Jagannadham, and B.C. Sales, *Pulsed laser deposition of Bi2Te3-based thermoelectric thin films.* Journal of Applied Physics, 2003. **94**(6): p. 3907-3918

95. Hsin, C.-L., et al., *Phase transformation and thermoelectric properties of bismuth-telluride nanowires.* Nanoscale, 2013. **5**(11): p. 4669-4672.

96. Poudeu, P.F.P. and M.G. Kanatzidis, *Design in solid state chemistry based on phase homologies. Sb4Te3 and Sb8Te9 as new members of the series (Sb2Te3)m·(Sb2)n.* Chemical Communications, 2005. **21**: p. 2672-2674

97. Taylor, A., et al., *Vapor Annealing as a Post-Processing Technique to Control Carrier Concentrations of Bi2Te3 Thin Films.* Journal of Electronic Materials, 2010. **39**(9): p. 1981-1986

98. Schumacher, C., et al., *Optimizations of Pulsed Plated p and n-type Bi2Te3-Based Ternary Compounds by Annealing in Different Ambient Atmospheres.* Advanced Energy Materials, 2013. **3**(1): p. 95–104

99. Dresselhaus, M.S., et al., *New Directions for Low-Dimensional Thermoelectric Materials.* Advanced Materials, 2007. **19**(8): p. 1043-1053

100. Romano, G., A. Carlo, and J.C. Grossman, *Mesoscale modeling of phononic thermal conductivity of porous Si: interplay between porosity, morphology and surface roughness.* Journal of Computational Electronics, 2012. **11**(1): p. 8-13

101. Yang, R., G. Chen, and M.S. Dresselhaus, *Thermal conductivity of simple and tubular nanowire composites in the longitudinal direction.* Physical Review B, 2005. **72**(12): p. 125418

102. Zebarjadi, M., et al., *Effect of nanoparticle scattering on thermoelectric power factor.* Applied Physics Letters, 2009. **94**(20): p. 202105.

103. Kyotani, T., et al., *Chemical modification of carbon-coated anodic alumina films and their application to membrane filter.* Journal of Membrane Science, 2002. **196**(2): p. 231-239.

104. Sander, M.S., et al., *Fabrication of High-Density, High Aspect Ratio, Large-Area Bismuth Telluride Nanowire Arrays by Electrodeposition into Porous Anodic Alumina Templates.* Advanced Materials, 2002. **14**(9): p. 665–667.

105. Thompson, G.E., *Porous anodic alumina: fabrication, characterization and applications.* Thin Solid Films, 1997. **297**(1–2): p. 192-201.

106. Li, A.P., et al., *Hexagonal pore arrays with a 50–420 nm interpore distance formed by self-organization in anodic alumina.* Journal of Applied Physics, 1998. **84**(11): p. 6023

107. Zhang, X., et al., *Silicon Patterning Using Self-assembled PS-b-PAA Diblock Copolymer Masks for Black Silicon Fabrication via Plasma Etching.* Plasma Processes and Polymers, 2012. **9**(10): p. 968–974